12-17-2010

Highly Sensitive and Selective Gas Sensors Based on Vertically Aligned Metal Oxide Nanowire Arrays

Jiajun Chen
University of New Orleans

Highly Sensitive and Selective Gas Sensors Based on Vertically Aligned Metal Oxide
Nanowire Arrays

A Dissertation

Submitted to the Graduate Faculty of the
University of New Orleans
in partial fulfillment of the
requirements for the degree of

Doctor of Philosophy
in
Engineering and Applied Science
Physics

by

Jiajun Chen
M.S. University of Electronic Science and Technology of China, 2004
B.S. University of Electronic Science and Technology of China, 2001

December, 2010

Dedication

This dissertation is dedicated to my mother, Mrs. Wanhuan Zhu and my wife, Jie.

Acknowledgments

Contents

Abstract

Mimicking the biological olfactory systems that consist of olfactory receptor arrays with large surface area and massively-diversified chemical reactivity, three dimensional (3D) metal oxide nanowire arrays were used as the active materials for gas detection. Metal oxide nanowire arrays share similar 3D structures as the array of mammal's olfactory receptors and the chemical reactivity of nanowire array can be modified by surface coatings. In this dissertation, two standalone gas sensors based on metal oxide nanowire arrays prepared by microfabrication and *in-situ* micromanipulation, respectively, have been demonstrated. The sensors based on WO_3 nanowire arrays can detect 50 ppb NO_2 with a fast response; well-aligned CuO nanowire array present a new detection mechanism, which can identify H_2S at a concentration of 500 ppb. To expand the material library of 3D metal oxide nanowire arrays for gas sensing, a general route to polycrystalline metal oxide nanowire array has been introduced by using ZnO nanowire arrays as structural templates. The effectiveness of this method for high performance gas sensing was first investigated by single-nanowire devices. The polycrystalline metal oxide coatings showed high performance for gas detection and their sensitivity can be further enhanced by catalytic noble metal decorations. To form electronic nose systems, different metal oxide coatings and catalytic decorations were employed to diversify the chemical reactivity of the sensors. The systems can detect low concentrated H_2S and NO_2 at room temperature down to part-per-billion level. The system with different catalytic metal coatings is also capable of discriminiating five different gases (H_2S, NO_2, NH_3, H_2 and CO).

Keywords: Gas Sensors, Nanowires, Nanostructures, Metal Oxides, Three Dimensional

Chapter 1

Introduction

1.1 The Momentum of Nanotechnology

Nanotechnology is a multidisciplinary field, which spans over various basic science and engineering areas. The earliest arise of the term "nano-technology" should be dated back to the year of 1956, when Prof. Richard Feynman in California Institute of Technology presents the famous talk "There's Plenty of Room at the Bottom" [1]. He described the possibility of manipulation of individual atom or molecule, the new phenomena in the confined scales and the bright future to expand the functionality of various tools. After that, new discoveries in nanoscale, such as quantum confinement effect [2], fullerene [3], carbon nanotube [4, 5], and graphene [6], had generated lots of interest in the nanotechnology. The Clinton's administration elevated the nanoscience and nanotechnology as a federal level initiative, referred as National Nanotechnology Initiative (NNI) [7], in 2001 when the research in nanotechnology started to pick up its momentum in various disciplines. Significant advances have been made in the last decade both in fundamental science research and the applications of nanotechnology. Figure 1.1 gives publication numbers with keyword of "nanotechnology" in last 20 years. The number of related publications have been increase at least 10 times from the year of 2001 to 2009, implying tremendous research efforts have been put into this area and this trend will be maintained.

There are two major properties of nanomaterials that are employed in many applications of nanotechnology: quantum confinement effects and large surface-to-volume ratio, which will be
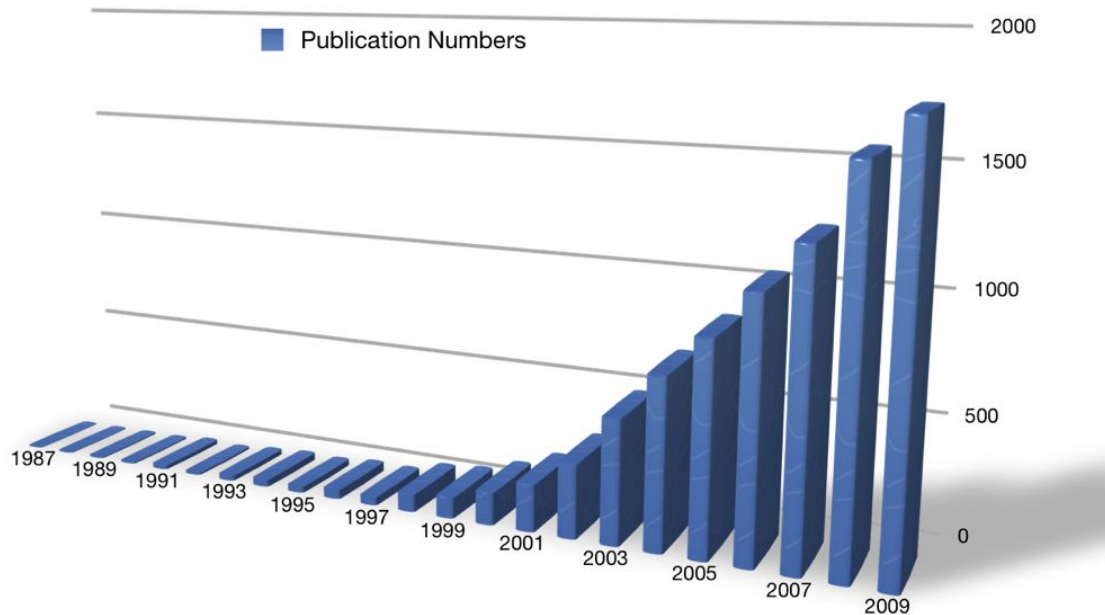
Figure 1.1: Number of publications with the keyword "nanotechnology" in last 20 years, acquired from ISIknowledge website.

briefly introduced. As the feature size of nanomaterials reduces to less than 10 nm, the condition of periodic energy wells in a crystal may be broken down in one or more dimensions and the boundary effects must be considered. The nanomaterials can be divided into four different categories in terms of the confinement of dimensionality, which are shown in Figure 1.2. The representative plots of their corresponding density of states (DOS) are given on the left side. For the nanomaterials (e.g. quantum dots, nanowires, 2-dimensional electron gas) in which the electrons are confined in at least one direction, discreted energy level may arise and the energy band gaps may also deviate from their bulk counterparts. One famous example with commercialized applications [8] (e.g. biological labeling, light emitting diodes, photovoltaics, etc.) is the semiconducting quantum dots with emission wavelengths that can be adjusted through their sizes. However, the feature size of nanomaterials must be less than certain values ($\sim$ 10 nm) so that the effect of quantum confinement
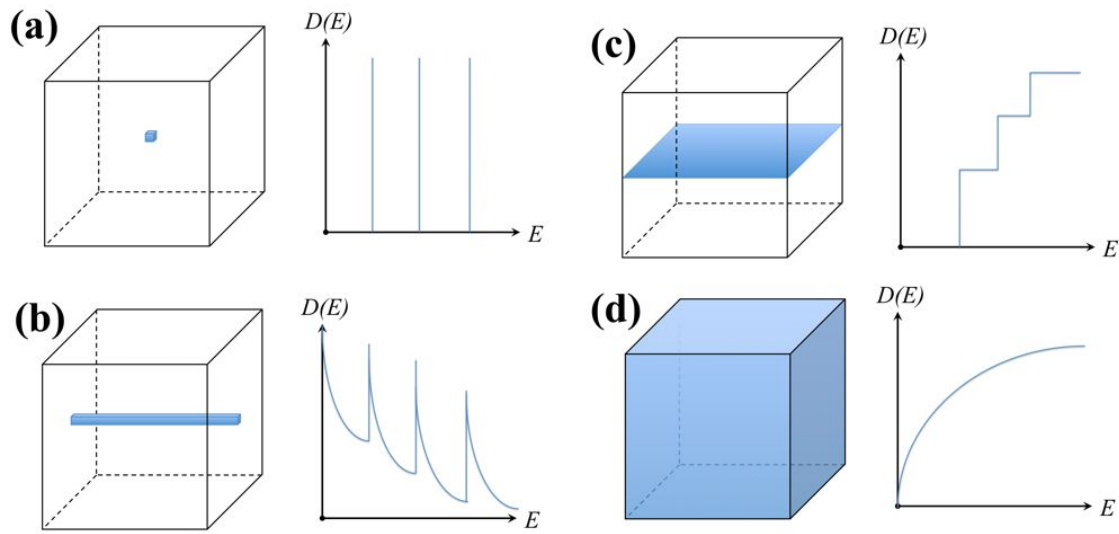
Figure 1.2: The diagrams and representative plots of density of states (DOS) of confinement nano-materials: (a) 0D, namely a single energy well with barriers along all three directions; (b) 1D, quantum wire; (c) 2D, electron wave function are limited in a two-dimensional layer; (d) bulk materials. After Ref. [9].

is applausible.

Another important properties for nanomaterials is the large surface-to-volume ratio, which means nanomaterials consist more precentage of surface atoms as the feature sizes decrease. Figure 1.3 plots the percentage of surface atoms with respect to the nanoparticle diameters, showing the inverted proportional relationship between them, showing that the percentage of surface atoms significantly increases as the particle diameter decreases, especially when the diameter is less than several tens of nanometers. The inset is a schematic comparing the surface atoms in spherical particles with different diameters. Generally, surface atoms have much higher reactivity than the bulk (inner) atoms of a particles due to the suspended (dangling) chemical bonding. This is why nanometerials are generally have higher reactivity than bulk materials. For instance, the performance of Pt catalytic nanoparticles can be significantly enhanced when the particle size is reduced. And further, the large surface-to-volume ratio can also alter the fundamental properties of the materials, such as increment of gas absorption and overall resistance.
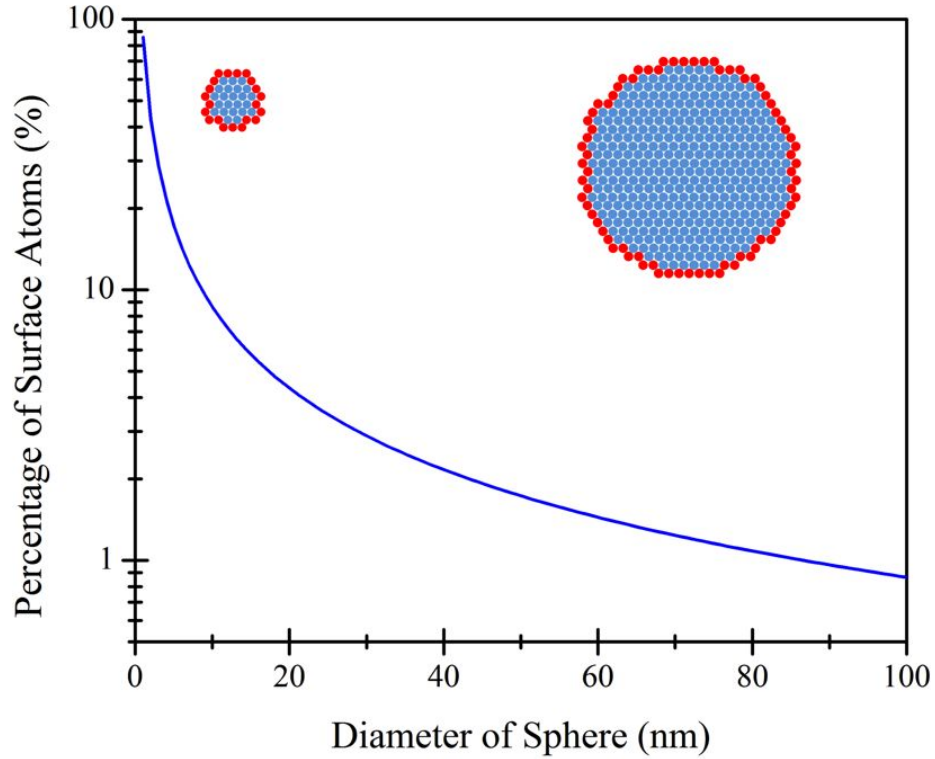
Figure 1.3: Plot of percentage of surface atoms in terms of the diameter of a spherical nanoparticles with close-packed structure, showing the inversely-proportional relationship. The insets are two schematics showing how the sphere diameters affect the surface-to-volume ratio.

Nanotechnology has infiltrated into many scientific areas and enabled numerous novel applications, such as biological labeling [10], drug delivery [11], renewable energy [12], environmental monitoring [13], electronics [14], etc. Among all these applications, nanomaterials and nanodevices for gas sensing is one of the most important aspects of nanotechnology with promising future of real world applications, which is also the central topic of this dissertation.

1.2 Modern Electronic Gas Detection

Gas sensor is one of the most important modern electronic components, which has obtained major progress of performance in the last few decades [15]. Similar to other sensing devices

(e.g. photo-diode, charge-coupled device (CCD), microphone or sonar detector), gas sensors play a role of interface between environment and electronic systems. Gas sensors can discriminate some specific chemical vapor molecules that present in environment, evaluate their concentration and monitor their change. Based on the enormous performance increase, gas sensors currently have various critical applications, such as public safety, environmental monitoring, food industry, aerospace, automobile, etc [16, 17]. For examples, gas sensors have been employed to monitor the product quality in perfume industry, and toxic gas detectors can be used for environment evaluation before workers enter some dangerous work places. Recent development in technology and applications has imposed more and more strict requirements on the performance of gas sensors. The development of mobile devices, high-speed wireless networks, and geographical positioning system (GPS) makes the massively distributed environment monitoring system become possible [18], which require the sensing devices to have small form-factors and extremely low power consumption [19]. Additionally, highly sensitive and selective gas sensors with fast response are needed for applications in public safety. These requirements triggered enormous research efforts in the development of high performance gas detection devices. The application of nanomaterials and nanotechnology is a major route to meet these demands. In the following sections, the general electronic gas detection methods will first be introduced, and then we will focus on the detection mechanism of metal oxide conductometric gas sensors and the applications of nanotechnology in metal oxide gas sensors.

1.2.1 Electronic Gas Detection Methods

To analyze the gas contents in the atmosphere, one needs to detect the variation in physical or chemical properties of the environment when the interested gases present or absent, for examples, electrical conductivity, photo-luminescence, and gas diffusion coefficient have been employed as the media to identify specific vapor molecules [17, 20, 21]. Many of these gas sensors have already been commercialized to real life products. In the following part, we will introduce the gas sensors

5

based on electrical detection methods, while other special gas detection schemes, such as mass spectrometers, gas chromatograph, or optical sensors, will not be covered since electrical detection are the most promising methods to simultaneously address concurrent demands of gas detection - low power consumption, portable, high sensitivity and stability, etc.

Electrochemical Sensors. The operation of an electrochemical sensor relies on the oxidation or reduction of gas molecules at the surface of sensing electrode where an electrical signal proportional to the gas concentration is generated. Figure 1.4(a) shows the detection mechanism of an electrochemical sensor. A hydrophobic membrane is generally used in a real sensor to avoid the electrolyte leaking and allow the gas molecules to diffuse into the device. The electrical current flow through the circuit is proportional to the gas concentration, which can be easily picked up by a current meter. Thus, this type of gas sensors is also named as amperometric gas sensors. Because the electrical current is generated from the reaction and generally no heating element is needed, electrochemical sensors have the lowest power consumption among all kinds of gas sensors. However, electrochemical sensors show relative poor selectivity, which can be improved by the use of a chemical filter.

Catalytic Combustible Gas Sensors. Catalytic combustible gas sensors are also called as "catalytic bead detector" due to their bead-shape catalytic metal oxide compounds. A platinum coil goes through the catalytic bead, which work as the heating wire and the resistive sensors, as shown in Figure 1.4(b) [22]. The ignition temperature is generally very high for most combustible gases ($> 1000°$C), while the catalytic bead can effectively reduce the ignition temperature down to $500°$C. The combustion reaction increase the temperature of the platinum wire and thus change the resistance of the wire. The resistance change can be monitored by electronic meter. The catalytic combustible gas sensors are easy to manufacture but pull large power consumption due to the high working temperature.

Surface-Acoustic-Wave (SAW) Gas Sensors. Figure 1.4(c) provides the diagram of a typical SAW gas sensor [23, 24]. Two piezoelectric tranducers are located at the both sides of a gas
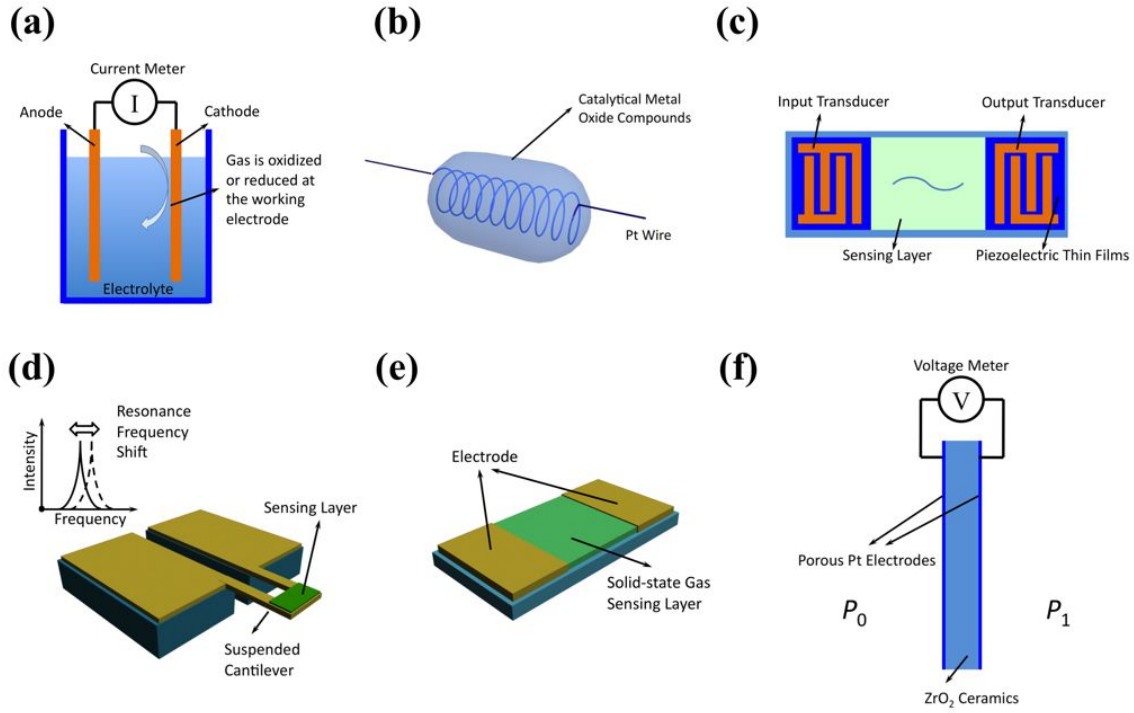
Figure 1.4: Schematic diagrams of electronic gas sensors based on different detection mechanisms: (a) electrochemical sensors; (b) catalystic combustible gas sensors; (c) surface-acoustic-wave (SAW) gas sensors; (d) cantilever gas sensors; (e) solid-state conductometric gas sensors; (f) Zirconium oxide oxygen sensors.

sensing membrane. A high frequency signal is applied onto the input transducer, in which the piezoelectric film generates a SAW across the sensing layer. After propagating through the sensing layer, the SAW is picked up by the output transducer. The propagation velocity of SAW in the sensing layer is changed when the device is exposed to the targeting gases. By monitoring the phase difference between the input and output signal, the concentration of targeting gases can be evaluated. The most important benefit of using SAW is its slow propagation speed compared with electromagnetic waves, which allows the preparation of miniaturized sensors working at high frequency and provides fast responses.

Cantilever Gas Sensors. Micro-cantilever is a thin film beam freely suspended above the device substrate, which is generally prepared by microfabrication in microelectromechanical systems (MEMS) [25–27]. The cantilever has a intrinsic resonant frequency that is determined by the mate-

rials, geometrical factors, and the environment. A sensing layer can be applied onto the cantilever for gas molecule detection [Figure 1.4(d)]. The resonant frequency of the cantilever changes due to the mass increment caused by gas absorption. Frequency measurement is generally more robust than current or voltage measurement and show strong capability to resist background noise. Biological sensing layer, such as deoxyribonucleic acid (DNA), enzyme, or protein, can be employed for bio-detection and the cantilever can be easily adapted into devices that operate liquid phase media. The fabrication of cantilevers are relatively complex and requires well-controlled processings.

Solid-State Conductomentric Gas Sensors. Solid-state conductometric gas sensors consist of two metal electrodes through which the conductivity or resistivity of the materials is continuously measured. The active sensing materials can be in the forms of bulk, thin or thick films. Various materials have been used as the active materials, such as metal oxides [28], conducting polymer [29–31], graphene [32], carbon nanotubes (CNTs) [33] etc. The adsorbed gas molecules at the material surface or interface alter the electronic structures and result in conductivity change. The detailed detection mechanism and factors that influence the sensing performance will be discussed in the following section. The structure of conductometric gas sensors is relatively simple and very convenient for large scale production and they also show very high sensitivity and selectivity. Additionally, many different methods can be used for sensitivity tunig, which enable construction of more complex gas detection systems — electronic noses.

Zirconium Oxide Oxygen Gas Sensors. This type of gas sensors is widely used in automobile vehicle, in which the gas sensor monitors the oxygen content in the engine emission and feedback the measurement to the controller computer for efficient fuel combustion in the engine. Similar to solid-state conductometric sensors, ZrO_2 sensors are also two terminal devices, shown in Figure 1.4(f). The porous catalytic platinum electrodes are applied on the both sides of ZrO_2 ceramics. The platinum electrodes not only work as electrical connections but also help to dissociate the oxygen molecule and generate oxygen ions. The ZrO_2 is solid electrolyte that transport the current

of oxygen ions. The difference in oxygen partial pressure between both sides of the ZrO_2 ceramics induces a Nernst voltage, which can be measured across the electrode elements. The device works at high temperature and provide fast response, however this high temperature also brings up some problems. For instance, the temperature is so high that almost all the combustible gases can be ignited, which creates interference signals. The device is majorly used for monitoring the waste gas emissions and is not suitable for portable applications.

Other than the above-mentioned detection methods, research groups are also developing new phenomena for gas sensing applications. Piezoelectric metal oxides have been used to detect the swell in organic polymer when they were exposed to organic vapors [34, 35] and the effect of gas environment on the Schottky barrier at the metal-semiconductor interfaces also showed very high sensitivity towards some specific gas molecules [36, 37]. The metal-insulator-transition (MIT) in vanadium oxide was also employed for gas detection [38, 39]. Though these sensors only demonstrated in the laboratory, most of them present the quality of high sensitivity and low power consumption, implying possible applications in high performance integrated systems.

1.2.2 Metal Oxide Conductometric Gas Sensors

As described in previous section, various phenomena can be used for gas detection. Among all these detection methods, metal oxide conductometric gas sensor is one of the most promising techniques that can meet the modern demands for integrated gas detection system due to their properties of low production cost, low power consumption, high sensitivity and stability [15, 40].

The metal oxide conductometric gas sensors detect gases by measuring the variation of resistance or conductance of the metal oxide materials. The mechanism of the change in conductivity is generally explained by the absorption and desorption processes of oxygen species on the semiconducting metal oxide surfaces [41]. Figure 1.5 provides experimental results of oxygen species adsorbed on the SnO_2 surfaces. It was found that molecule-ion species (O_2^- or O_2^{2-}) dominated the surface of metal oxide, while atomic-ion species (O^- or O^{2-}) presented at a relatively high

9
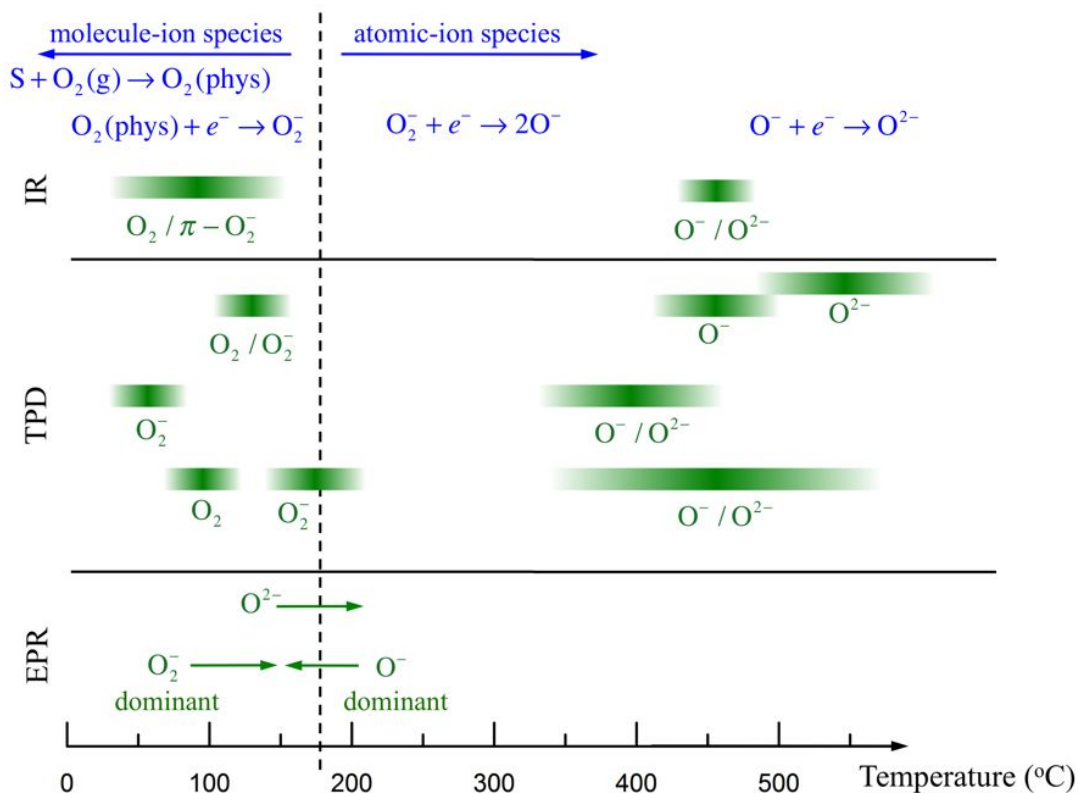
Figure 1.5: Oxygen species adsorbed on the SnO_2 surfaces analyzed with different methods: infrared (IR) analysis, temperature programmed desorption (TPD), electron paramagnetic resonance (EPR). After Ref. [41].

temperature. Though the transition temperatures given by different measurement techniques are different, the basic trends of this phenomenon are similar. The adsorbed oxygen species may form surface states that trap electrons from the semiconducting metal oxide creating a surface charge depletion layer that possesses high resistance. Therefore, it is possible to connect the conductivity of metal oxide with the coverage of oxygen species on its surfaces. Barsan et al. [41] have proposed a conduction model to relate the electrical conduction of metal oxide semiconductor with oxygen species adsorbed on its surface. The reaction equation for the oxygen absorption and desorption

can be given as

$$\frac{\beta}{2}O_2^{\text{gas}} + \alpha \cdot e^- + S \rightleftharpoons O_{\beta S}^{-\alpha} \tag{1.1}$$

where O_2^{gas} is oxygen molecule in the enviroment; e^- is an electron that can reach the metal oxide surface; S is the surface sites that can accept oxygen species. And α and β are integers that determine the type of oxygen species, for example, $\alpha = 1$ means the oxygen species are singly ionized and $\beta = 2$ means they are molecular form. By using the mass action law of Eq.1.1, one can deduce the relationship of concentrations of reactants and products:

$$k_{\text{ads}} \cdot [S] \cdot \left[e^-\right]^\alpha \cdot p_{O_2}^{\beta/2} = k_{\text{des}} \cdot \left[O_{\beta S}^{-\alpha}\right] \tag{1.2}$$

where k_{ads} and k_{des} are the reaction constants for oxygen absorption and desorption processes. The total number of surface sites for oxygen absorption including occupied ones is donated as $[S_t]$, and the surface coverage θ is given as $\theta = \left[O_{\beta S}^{-\alpha}\right] / [S_t]$. Thus, the Eq.1.2 can be rearranged by using the implied relation $[S] + \left[O_{\beta S}^{-\alpha}\right] = [S_t]$:

$$(1-\theta) \cdot k_{\text{ads}} \cdot \left[e^-\right]^\alpha \cdot p_{O_2}^{\beta/2} = k_{\text{des}} \cdot \theta \tag{1.3}$$

Eq.1.3 has created a relation between the surface coverage θ and the concentration of electrons that can reach to the surface $[e^-]$. However, more equations are needed to connect the electron concentrations with the oxygen partial pressure in atmosphere. The situation is similar to Schottky approximation [42] where the conditions of electroneutrality and carrier distribution based on Poisson equations were used. Once the geometry of the metal oxide crystal is defined, the relations between the electron density and the oxygen pressures can be obtained.

Discussion above has shown how the surface adsorbed oxygen species deplete the electrons close to the metal oxide surface creating a surface charge depletion layer. To further clarify the effect of oxygen molecules, we can use an n-type metal oxide semiconductor as an example to
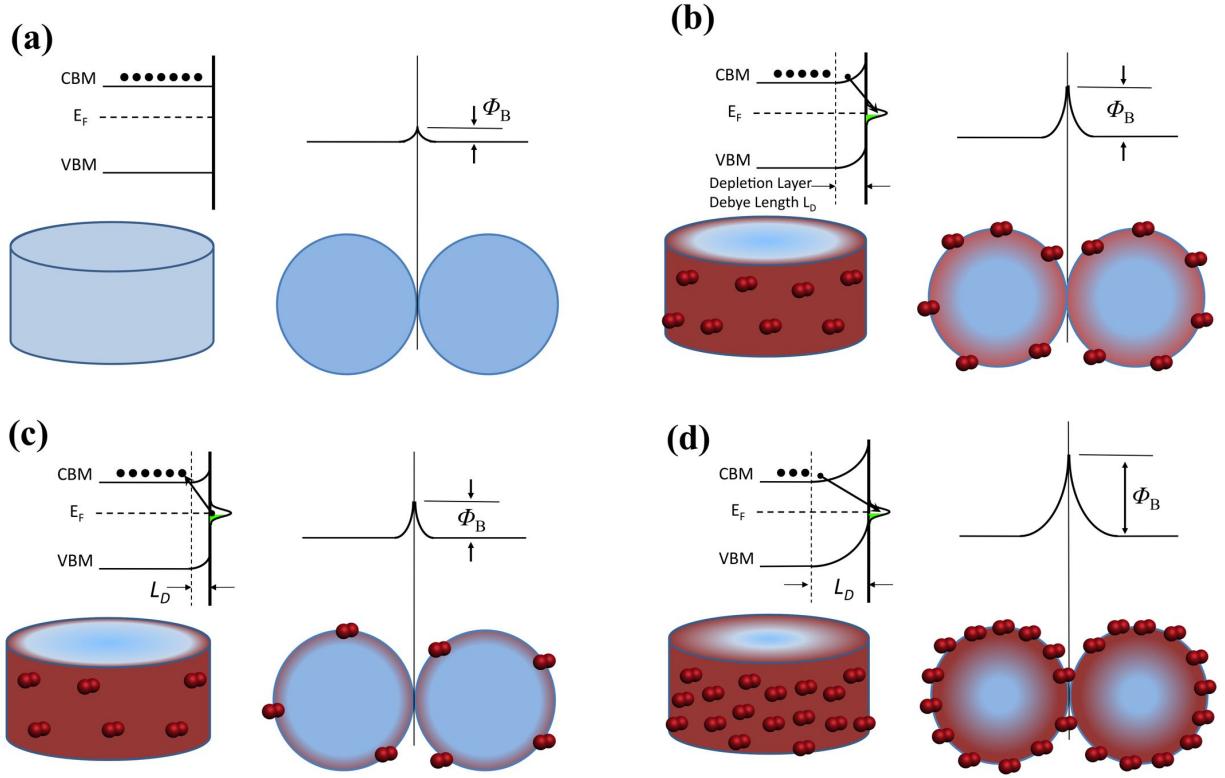
Figure 1.6: Schematics of relationship between oxygen adsorbates and the surface depletion layer on metal oxide wires or particles using *n*-type semiconductor as an example. (a) The energy bands and contact barrier for pristine metal oxides. (b) Metal oxides adsorb oxygen from atmosphere forming surface charge depletion layer. (c) Adsorbed oxygen species react with reducing gases and release trapped electrons back to metal oxide, which decreases the thickness of depletion layer. (d) Oxidizing gases trapped more electrons from metal oxides and enhance the depletion layer.

analyze the effect of surface reactions on the overall conductivity. Figure 1.6 shows several typical states and surface energy band diagrams of metal oxides when they are exposed to different ambient atmosphere. Considering that the metal oxide is in a realistic vacuum where no gas species are adsorbed, the carrier density on the whole material is homogeneous and there is a contact barrier between adjacent particles, which contributes the major part of the devices resistance [Figure 1.6(a)]. As the device exposes to the atmosphere, the oxygen species attach to the metal oxide surface forming surface states that trap electrons from material bulk. As mentioned before, this

process results in electron lost in the surface layer. The width of charge depletion layer is defined as Debye length, L_D. The build-up of depletion layer increases the particle-to-particle contact barriers and decrease effective cross-section for electron transport in metal oxide bulk, shown in Figure 1.6(b). When exposed to reducing gas molecules, such as H_2S, CO, NH_3, H_2 etc., the adsorbed oxygen species react with these gases and release the electrons back to the metal oxide semiconductor:

$$H_2 + O^- \rightarrow H_2O + e,$$
$$CO + O^- \rightarrow CO_2 + e,$$
$$2NH_3 + 3O^- \rightarrow 3H_2O + N_2 + 3e,$$
$$H_2S + 3O^- \rightarrow H_2O + SO_2 + 3e. \tag{1.4}$$
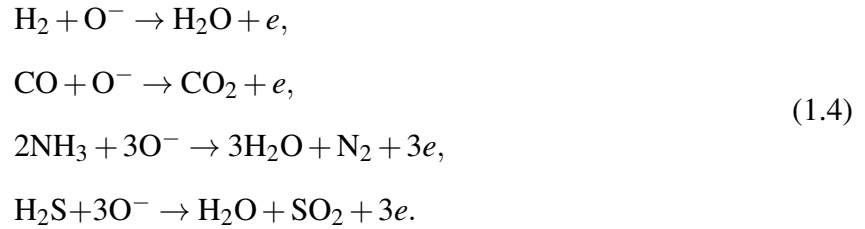
Depicted in Figure 1.6(c), the reducing gas molecules consume the oxygen species and effectively decrease the surface coverage of oxygen species at equilibrium. The width of depletion layer is proportional to the surface coverage of oxygen species, the reaction to reducing gases thus decrease energy barriers between adjacent particles and increase the effective conduction channel in the semiconductors, which result in overall increase in device conductivity. Figure 1.6(d) shows the situation when the metal oxide is exposed to oxidizing gases, such as NO_2 and Ozone. The oxidizing gas molecules play roles similar to oxygen species that trapped electron from metal oxide semiconductors:

$$NO_2 + e \rightarrow NO_2^-,$$
$$O_3 + e \rightarrow O_3^-. \tag{1.5}$$

Therefore, oxidizing gases further decrease the conductivity of the *n*-type metal oxide semiconductors. Contrary situation happens for *p*-type semiconducting metal oxides, such as CuO and NiO, since the majority carrier are positive holes.

13

D >> $2L_D$ (grain-boundary control)

D $\geq$ $2L_D$ (neck control)

low resistance region

D < $2L_D$ (grain control)

high resistance depletion layer
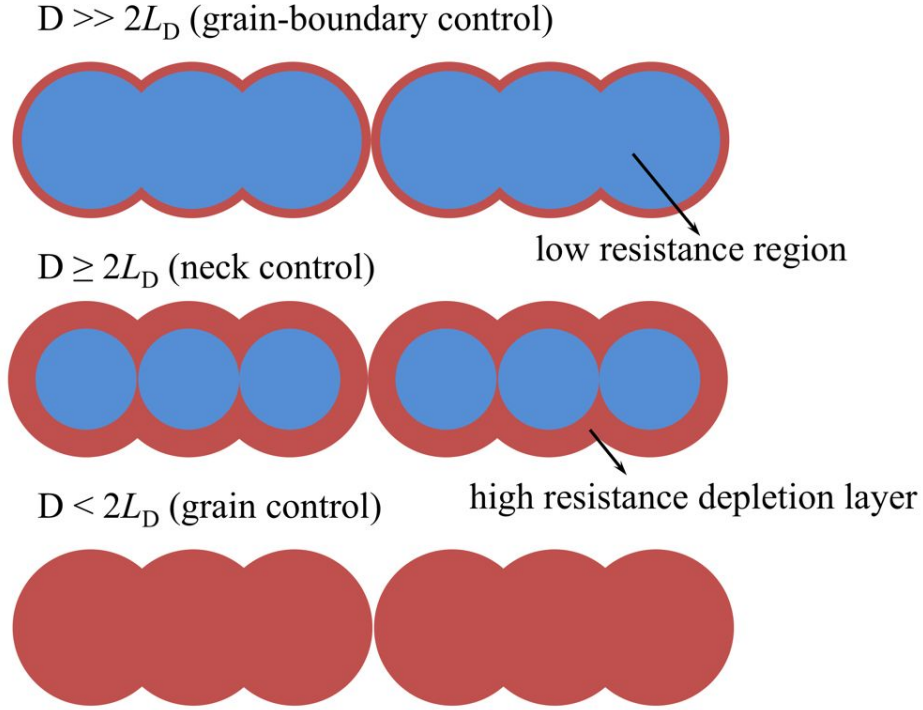
Figure 1.7: The effect of grain size on the overall carrier transport of the particulate metal oxide semiconductors. After Ref. [43].

1.2.3   Factors Affecting the Sensing Performance

Based on the oxygen-species absorption and desorption model, we will discuss briefly on the factors that influence the sensing performance of metal oxide conductometric sensors, such as crystalline size and catalytic additives.

1.2.3.1   Effects of Crystalline Size

The sensors that consists of small crystalline particles generally show high sensitivity. And recent reports on nanostructured materials for gas sensing applications also further confirmed that using fine particles as active materials can significantly enhance the sensors performance [44]. The effects of particulate size, D, on sensitivity can be elucidated through the comparison with the thickness of depletion layer, L_D. As shown in Figure 1.7, the change in depletion layer gives few

influence on the bulk conductivity of the nanocrystals when the particle size is much larger than the thickness of surface depletion layer. For this situation, the depletion layer majorly contributes to particle-to-particle barriers. If the grain size is close to L_D, confined conduction channels appear at the neck of chained particles, which determine the major parts of the resistance. If the grain size is smaller than the depletion thickness, which means the metal oxide crystals are fully depleted, the resistance of depletion region dominates the whole metal oxide nanoparticle and is directly related to the surface coverage of adsorbed gas species so that the highest sensitivity is reached. These models have been confirmed by experimental observations [45].

Other than the above-mentioned nanoparticle size, the feature size of other types of nanomaterials also play a crucial role of sensitivity. We can use single-crystalline-nanowire sensors as an example. There is not particle-to-particle barrier in this type of sensor. The electron transport is majorly controlled by the effect of depletion layer thickness. Figure 1.8 compares the conductivity change of two nanowires with different diameters. If the size of nanowires is close to the Debye length, a slight change in the depletion layer thickness will cause obvious change of effective conduction channel, implying higher sensing responses for nanowires with smaller diameters. In the example, the metal oxide wires with diameters of 4000 nm and 400 nm are compared. As one can see, the wire with 4000 nm diameter only give 10 % change in conductivity, while the 400-nm metal oxide wire can generate about 75 % conductivity change, which is move than 7 times larger than the big wire.

1.2.3.2   Effects of Catalytic Noble Metals

Proper amount of catalytic noble metal particles (e.g. Pt, Pd, Ag, etc.) can be added to the metal oxide materials to promote the sensing performance [46–50]. The oxide materials generally present lower T_{max} (the temperature where the sensitivity is maximized) and higher sensitivity. For example, 1.5 wt% Pd can effectively reduce the T_{max} of TiO_2-based trimethylamine (TMA) sensors from 470 °C to less than 350 °C [51].
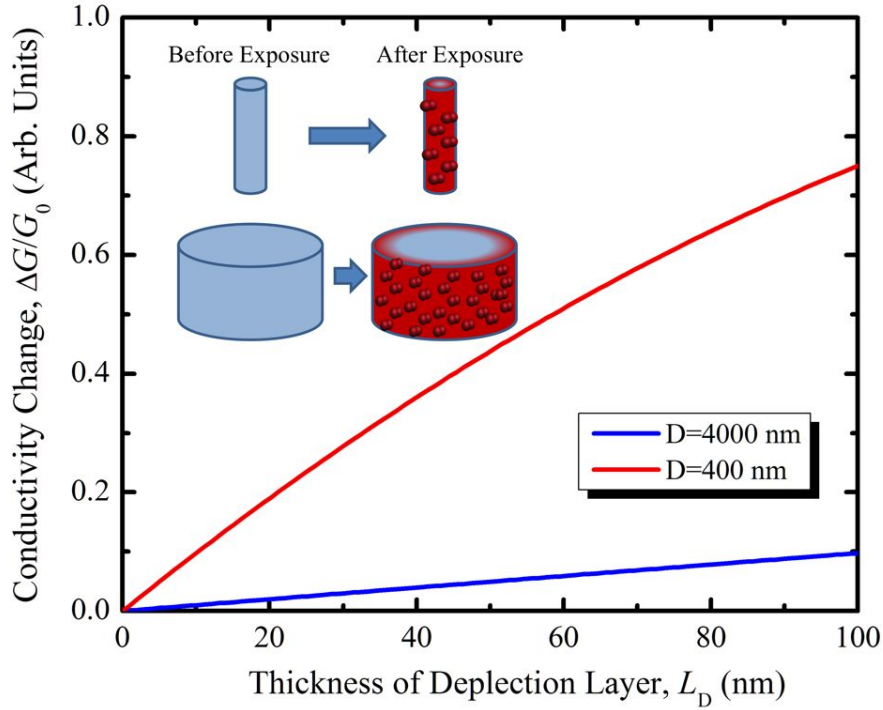
Figure 1.8: Plot of conductivity change ($\Delta G/G_0$) vs. depletion layer thickness (L_D), showing the effect of nanowire diameter on the conductivity change.

The promotion effects of noble metal particles can be explained in two aspects. Firstly, the catalytic noble metals are capable of dissociating the oxygen molecules into much more active oxygen species, which enhances the density of adsorbed oxygen species at the location close to the noble metal particles. Through this process, the oxygen is much more easy to react with the surface sites on the metal oxides, and consequently, the sensitivity is increased while T_{max} is decreased. This effect is called "chemical sensitization". Figure 1.9 depicts this process. The noble metal particles attached on the metal oxide surface help to dissociate the oxygen molecules into much more active oxygen species (i.e. O_2^-, O_2^{2-}, O^- or O^{2-}) before they reach the oxide surfaces. At the "spill-over" area near the noble metal particle, the density of oxygen species is higher and thus a thicker carrier depletion layer is formed. The activities of noble metal particles are directly related to their size due to the previously discussed surface-to-volume ratio, so the size of noble metal particles also plays an important role of the resulted device performance [53]. Secondly,
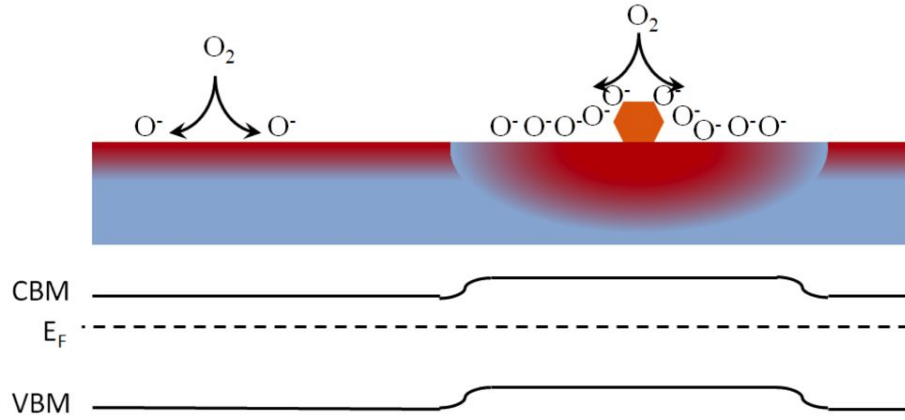
Figure 1.9: Schematic illustration showing the effect of catalytic metal particles on the absorption of oxygen species on the metal oxide surface. After Ref. [52].

the noble metals generally have higher work-function than metal oxides (for instance, Pd has a work-function of 5.1 eV while the work-function of SnO_2 is 4.5 eV) [54], which tends to migrate the carriers from metal oxides to noble metal particles. The oxygen species adsorbed on noble metal can further extract the electrons form the metal, which is equal to the situation that the oxygen species directly trap electrons from the metal oxides. This effect is referred as "electronic sensitization". Both of these effects increase the thickness of the depletion layer, which results in enhanced sensitivity.

1.2.3.3 Other Factors

Many other factors can influence the performance of gas sensors, such as particle crystalline facets, porosity of metal oxide, intentionally introduced dopants, sensor configuration, etc.

Crystalline facets. This can be explained by using SnO_2 as an example. Sn atoms in SnO_2 play the most important role of oxygen absorption. The density of surface Sn atoms defined the available sites for oxygen absorption. The distance between adjacent Sn atoms can be simulated through atomic model: $d_{(110)} \sim d_{(100)} < d_{(101)} < d_{(001)}$ [55]. Therefore, smaller atomic distance implies higher Sn density on the surface, which have direct effects on the absorption and desorption

dynamics of oxygen species. The surface facets can be controlled by the growth conditions and large particles generally tend to have lower indexed facets, implying another benefits of reduction in particle size [56].

Material porosity. It is not difficult to understand that a porous material allows gas molecules to easily diffuse into or out from the metal oxide. The effect not only increase the response speeds but also significantly improve the sensitivity [57–59]. This is also the reason why we are pursuing three-dimensional (3D) nanostructures for sensing applications. The detail implications of the porosity or structures of materials will be discussed in the following sections.

Dopants. Dopants are also frequently used to alter the material properties of metal oxides. One purpose is to increase the chemical diversity of metal oxides, which is beneficial for selective detection. Another important application is to increase the stability of gas sensors. As we mentioned before, a sensor that consists of fine crystalline may has limited stability in long period due to the crystal growth during the high temperature operation. Some dopants can introduce a surface coating on the surface of metal oxide crystallines and make them more stable at high temperature [60]. The dopants have many other complex effects, such as the influence on the surface states, carrier density, etc.

Sensor configuraton. A direct example is the position of metal electrodes for electrical connection in a metal oxide gas sensor. If the metal electrodes are located on the surface of metal oxide, they may only measure the conductivity change on the surface of metal oxide, while the average conductivity of material bulk is detected if the electrodes are put inside the inner part of the metal oxide [61]. The metals used in a gas sensors (e.g. Pt, Au) have catalytic behaviors to the gas adsorbates, therefore, their distance, thickness, and even the synthesis method also have major effect on the sensing performance.

1.2.4 Metal Oxide Nanowire Gas Sensors

From the discussion above, one can recognize that decreasing the crystalline size of the active materials is generally beneficial for the sensing performance. Accordingly, numerous efforts have been make to employ nanostructured metal oxide materials for the gas and chemical sensing [62–66]. Most of the metal oxides (ZnO [67–69], In_2O_3 [70], SnO_2 [71], WO_3 [72], Ga_2O_3 [73], and even complex oxides [74]) have been grown as nanostructures (e.g. nanoparticles, nanowires) and patterned into gas detection devices. These nanosensors show enhanced sensitivity over their thin film or bulk counterparts. For examples, gas sensors formed with individual In_2O_3 nanowire or nanowire networks can detect NO_2 down to 30 ppb at room-temperature [75].

Though the nanostructured metal oxides show very promising applications for gas detection, there are several major issues that limit their development. (a) The large surface-to-volume ratio do benefit the sensing responses, however, it also brings some negative effects of device performance. For instance, the small crystalline sizes tend to growth during high temperature operation, which degrade the long-term stability of the sensors. (b) Many research efforts have been focused on the reduction of feature size of nanomaterials and relatively small amount of research has been done on the organization or arrangement of the nanomaterials. The agglomerates of nanoparticles or the alignment of nanowires have complex effect on the sensing performance, however, only limited number of reports have addressed some aspects of this issue [76]. (c) The device fabrication, such as nanowire integration and alignment, is still a challenge issue for nanowire-based gas sensors. These processes consume the major parts of the production cost and some of them are even not available for large scale manufacture.

1.3 Biological Olfactory System and Electronic Noses

Though the research and application of man-made gas detection systems have obtained enormous progress during last several decades, there is no gas sensing device that can compete with the
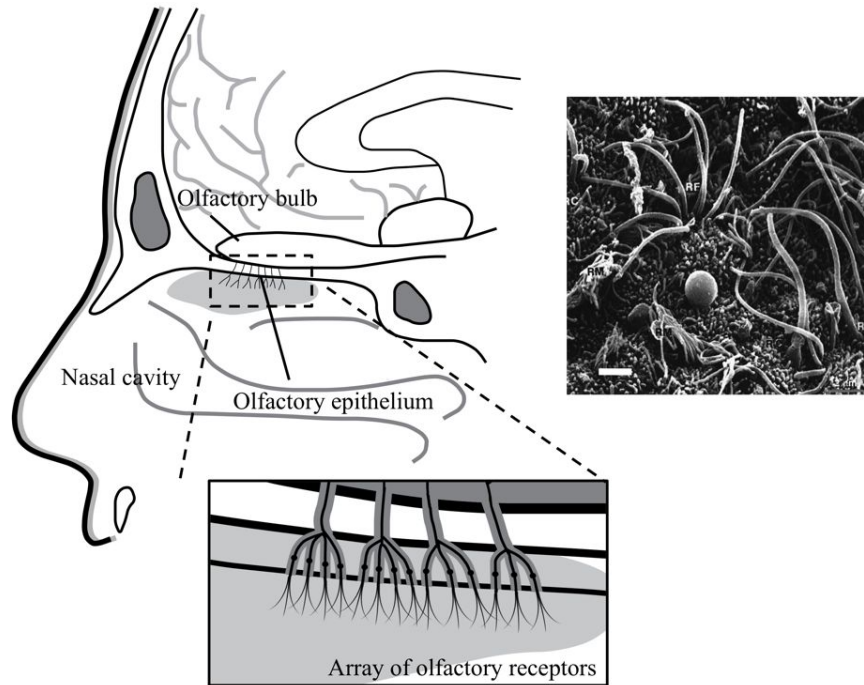
Figure 1.10: The skull cross-section showing the structure of nasal cavity. The enlarged inset is the array of olfactory receptors that have 3D nanostructures. The picture is a scanning electron microscope image of a real olfactory receptor array (Scale bar: 1 μm). After Ref. [77].

performance of mammal's olfactory system. Not like other sensing systems (sona device, optical microscopy, etc.), for which man-made systems generally have supreme abilities over the biological systems, it is still a challenge issue to identify composition of a gas mixture in an extremely low concentration. Human's nose is capable to discriminate more than ten thousand different types of chemical vapors and canine's olfactory system is even more sensitive. For example, an well-trained dogs can sniff out the trace of explosives (i.e. bombs or landmines) due to their capability of recognizing the chemical at a concentration of part-per-billion (ppb) [78]. Even though the training and maintenance of a dog for this purpose is very expensive, it is very difficult to find a electronic replacement. Therefore, electronic gas sensors with such detection limits are highly pursued for automatic detection and ubiquitous tracking of possible treat for many applications.

The strong capabilities of gas discrimination of mammal's olfactory systems can be attributed to the hundreds of millions of olfactory receptors that consist of tremendous surface area and
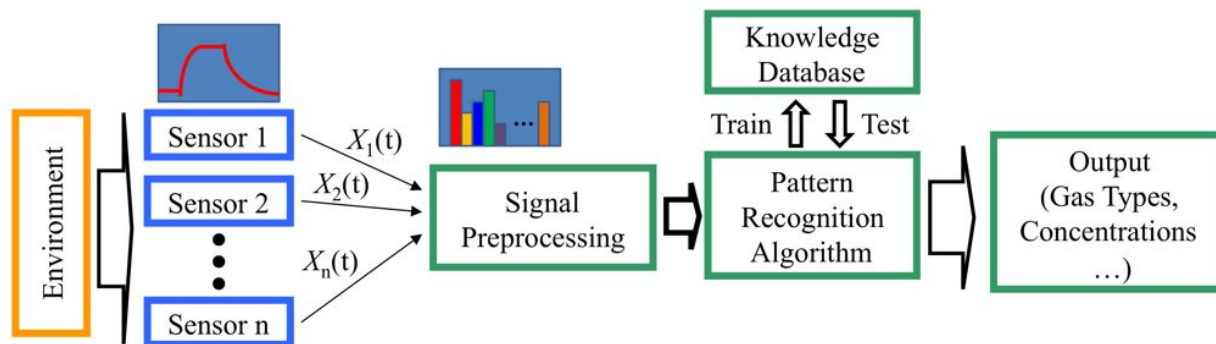
Figure 1.11: Architecture of an electronic nose system.

the largely diversified chemical properties for gas molecule capture and recognition. Figure 1.10 shows a cross-sectional structure of a human's skull, in which the nasal cavity is emphasized. The enlarged schematics depict the array of nanowire-like olfactory receptors. From the scanning electron microscopy (SEM) image, the olfactory receptors have similar shape as nanowires, the diameters and lengths of which are about $300 \sim 500$ nm and $5 \sim 8$ μm, respectively [79, 80]. The inhaled gas molecules react with the specific receptors that located in the olfactory epithelium. The collective signals from all the receptors are transmitted by olfactory neurons and processed by the brain. The large surface area of this receptor array is very efficient to capture low concentrated gas molecules, resulting in high sensitivity. Furthermore the largely chemical diversity of these receptors and the massively paralleled signal transmission and processing scheme contributed to the fast response and strong capability of gas recognition. In a brief summary, the biological system have three major advantages that is supreme over man-made gas sensors:

- Tremendous surface area of 3D olfactory receptor array;

- Largely diversified chemical reactivity of olfactory receptors for gas recognition;

- Massively parallel scheme for signal transmission and processing.

Based on the knowledge of biological olfactory systems, research groups have developed electronic systems that are able to identify the composition of a gas mixtures and pursuing performance

21
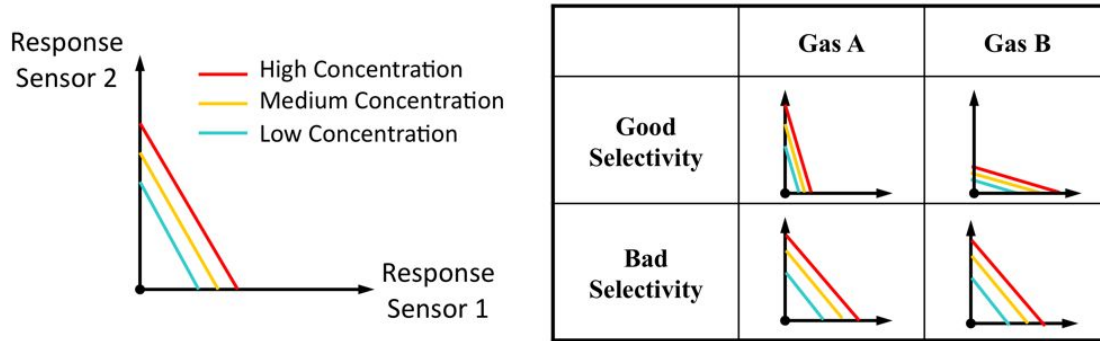
Figure 1.12: Schematic plots that explain the simplest case of gas discrimination by an array of two sensors.

surpass biological system in some aspects. This type of electronic systems is generally referred as "electronic noses" or "machine olfactory systems" [77, 81–86]. The architecture of a typical electronic nose system is shown in Figure 1.11. An electronic nose generally consists of several gas sensors with different sensitivity specifically designed for different gases. The detected signals are continuously monitored when the devices are exposed to the atmosphere. The collective signals are pre-processed before transmission to a pattern recognition engine (PRE). The details about the signal processing is discussed in Appendix B. In certain recognition algorithm, the PRE must be trained with serial known gases. According to the detected signals, a knowledge database is formed. And this knowledge database can be used as a reference to identify the gas types, concentrations of unknown gas mixtures. The performance of the whole system depends on the collaboration of the sensors, signal processing, and the design of recognition algorithm. In this dissertation, we emphasize the design of gas sensors and also cover some aspects of the signal processing.

To give a simplest example of gas discrimination, we can use a radial plots to analyze a two-sensor system for detection of a mixture with two types of gases (Figure 1.12). The axes in the plots represent the sensing responses. A triangle (or polygonal for more than two devices) can be drawn by connected the response points on the adjacent axes. The shapes of the radial plots denote the response patterns to different gases. If two devices present good selectivity with respect to these
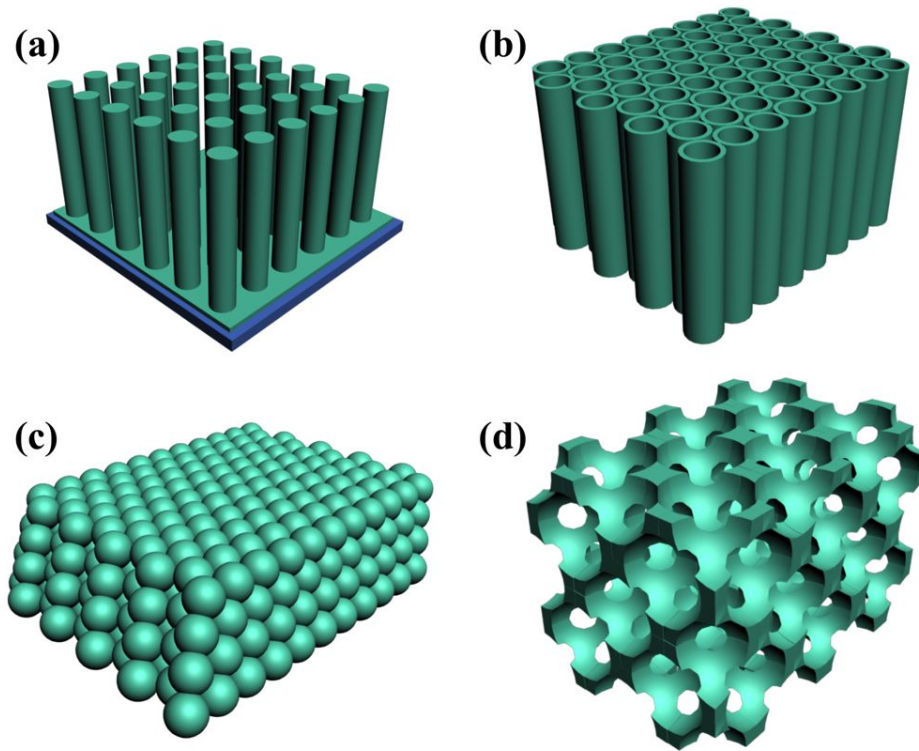
Figure 1.13: Schematic diagrams of four major 3D nanostructures: (a) nanowire array, (b) nanotube array, (c) opal structure, and (d) inverted opal structure.

gases, the shapes in the radial plots must be different so that the two gases can be discriminated.

To mimic the biological olfactory systems, we proposes to use 3D metal oxide nanostructures to create an electronic gas detection systems that have large surface area, high porosity, and controllable chemical reactivity for highly sensitive and selective gas detection.

1.4 3D Metal Oxide Nanowire Arrays for Gas Detection

Based on the discussion in previous sections, we can conclude that there are three key factors that define the sensitivity of gas sensors based on metal oxide nanostructures: (1) the intrinsic properties and critical dimensions of nanostructured materials; (2) the structural arrangement of the nanostructures in the gas sensors; (3) the concentration profiles of gases in the device structures, which is defined by the porosity and the distribution of catalysts. Many efforts have been

put into the engineering of individual nanostructures (i.e. nanowires, nanotubes, nanoparticles). Recently, 3D nanostructures, such as vertically aligned nanowire/nanotube arrays, opal and inverted opal structures, attracted more and more interest in the research of the gas detection using these types of materials. The 3D nanostructures have extremely large surface area, high porosity, and furthermore, the chemical properties of metal oxide nanostructures can be easily altered by using catalytic metals, exotic dopants, or fine structure tuning, which is very crucial for selective detection in electronic noses.

Figure 1.13 shows several typical 3D nanostructures: nanowire/nanotube arrays [87–92], opal and inverted opal structures [93–96], the fabrication and properties of which have been intensively studied among nanotechnology society. 3D nanostructures can make full use of the nanostructure surface and their intrinsic channels allowed gas molecules readily transport into and escape from the materials, which help to increase the sensitivity and response speed and lower the operation temperature. The fabrication of 3D nanostructures provides a route to optimize sensing performance by tuning the structural parameters of metal oxide nanomaterials.

In the following sections, we will introduce the preparation methods of metal oxide nanowire arrays. The preparation of nanowires can be divided into two categories: "top-down" and "bottom-up". The "top-down" methods refer to prepare nanowires by etching from bulk materials or thin films [97]. "Bottom-up" methods "grow" nanowires from vapor or solution sources, and the 1D structure of nanowires is formed by the guidance of templates or caused by the intrinsic anisotropic growth rates. We will focus on the "bottom-up" techniques, which can be further classified into vapor-based growth and solution-based growth according to the phase of growth environments.

1.4.1 Vapor-phase Growth of Metal Oxide Nanowire Arrays

The process for nanowire growth by vapor-based methods can be separated into three Stages: (1) generating vapor from deposition source; (2) transporting materials from the source to the growth substrate; (3) consolidation of deposition material and forming nanowires on the substrates.
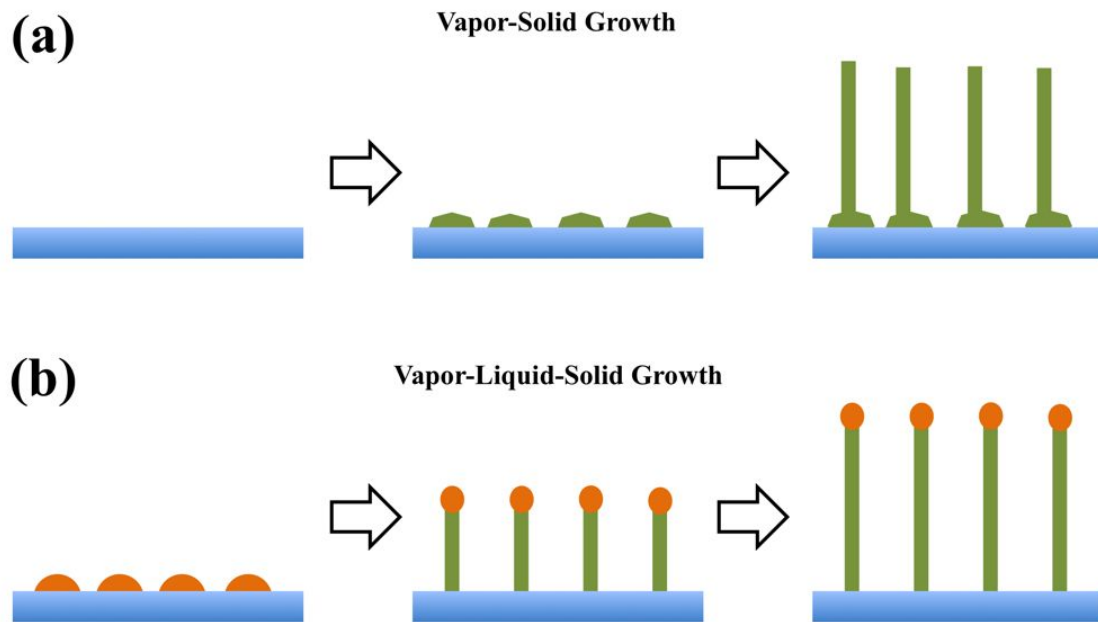
Figure 1.14: Schematics showing two major mechanism for nanowire array growth by vapor phase methods: (a) vapor-solid (VS) growth and (b) vapor-liquid-solid (VLS) growth.

Most of the vapor-based thin film techniques can be used for nanowire growth, such as thermal evaporation, chemical vapor depostion (CVD), pulsed laser deposition (PLD).

Figure 1.14 depicted two typical mechanisms for vapor-phase nanowire growth. In a vapor-solid (VS) process, the vapor source directly condenses on the substrates forming a pre-growth crystallines. These crystallines work as seeds that guide nanowire growth. For some metal oxides, such as ZnO, their growth rates are highly anisotropic in proper growth conditions, thus, the nanowires growth along the crystal direction with highest growth rates. This mechanism is convenient however lack of the control of nanowire diameters. Vapor-liquid-solid (VLS) process was first employed for the growth of single crystalline Si whiskers [98], and later was adapted for metal oxide nanowire growth. In a VLS process, catalytic metal particles are dispersed on the growth substrate. When the substrate reaches the growth temperature, the metal particles melt and become liquid phase droplets. The source vapor dissolves into the metal droplet forming liquid-phase alloys. As the concentration of source materials in the alloys exceeds the solubility, the

25
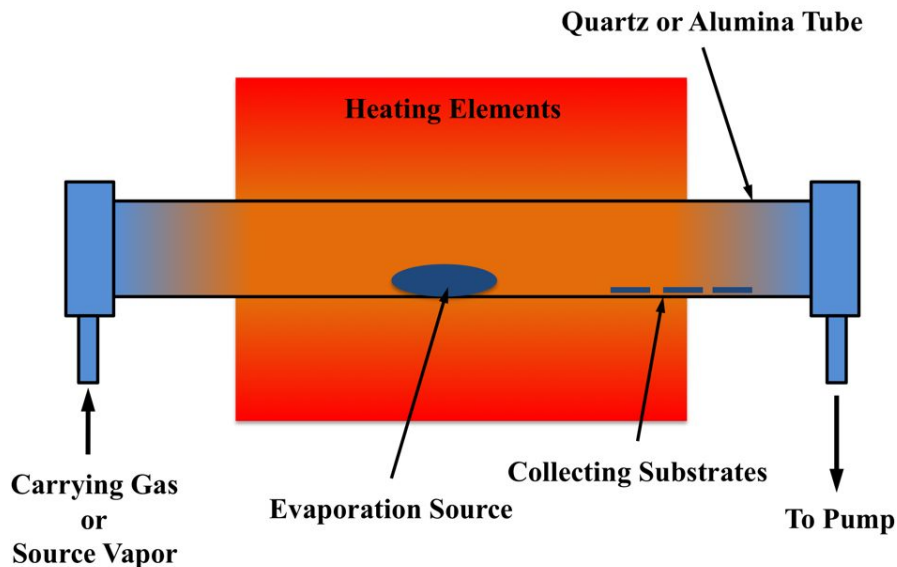
Figure 1.15: Schematic diagram of a chemical vapor deposition (CVD) system based on a tube furnace.

source materials start to segregate and consolidate into nanowires. VLS process has been widely used for nanowire growth since it provide a convenient way to control the nanowire diameter by using catalytic metal particles with different sizes [99–102].

After discussion on the growth mechanism, we will have a brief survey on different vapor-phase synthesis for metal oxide nanowires:

Chemical vapor deposition (CVD). CVD is the most widely used methods for nanowire growth. It is basically created on a vacuum sealed tube furnace, the typical diagram of which is shown in Figure 1.15. A vacuum pump is used to evacuate the quartz or alumina tube in the furnace and maintain the pressure in the tube furnace. Processing gases are inlet from the upstream forming a continuous and stable flow when incoporated with the vacuum pump. The source materials can be introduced with the gas flow or evaporated at the high temperature zone of the furnace. A series of substrates are loaded at the low-temperature zone for nanowire growth. The equipment for CVD is relatively simple and it provide very good control over the growth dynamics of nanowires.

Pulsed laser deposition (PLD). Pulsed laser beam is a high energy source, which can heat

26
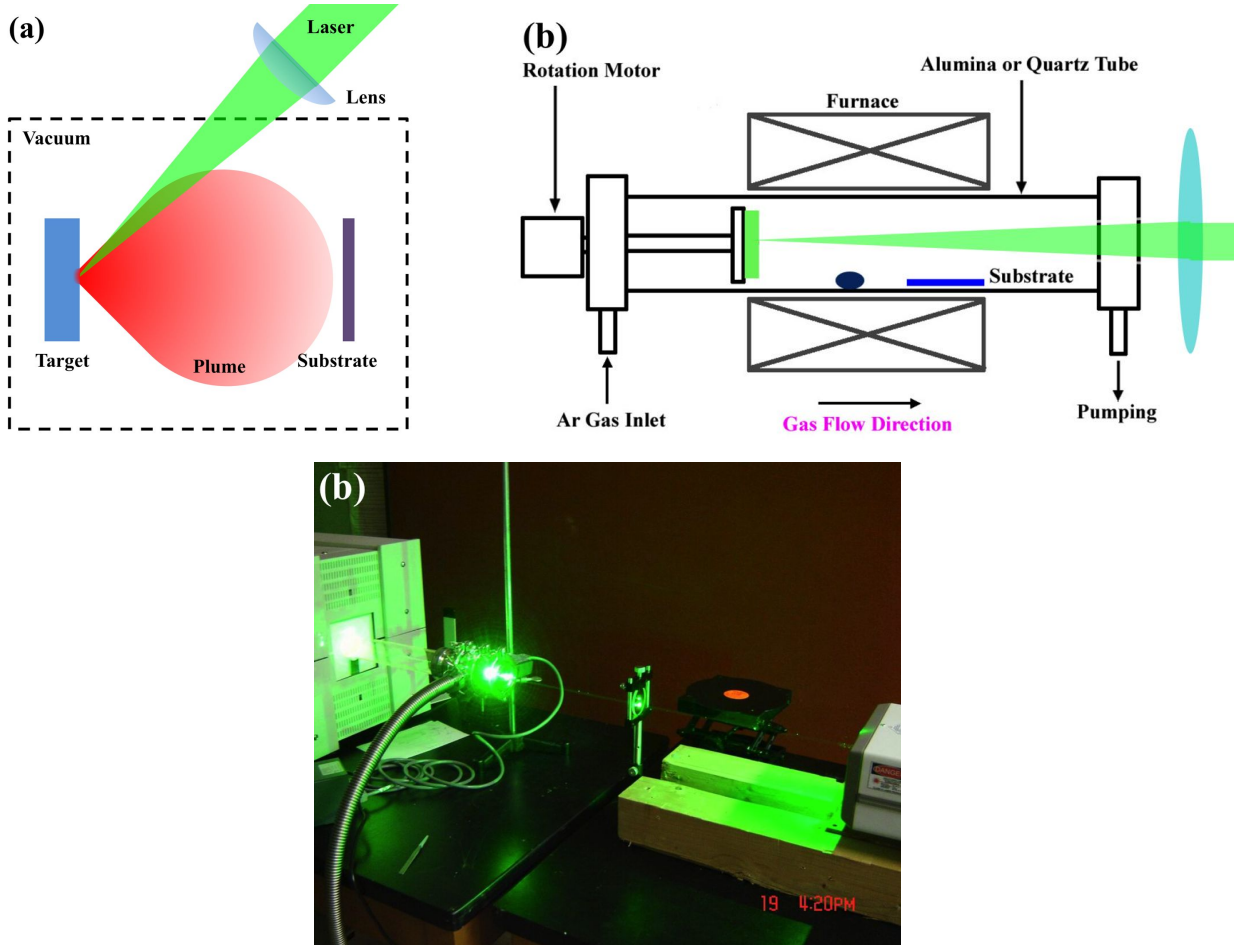
Figure 1.16: Schematics of (a) a PLD process, (b) a PLD system integrated with a tube furnace for nanowire growth and picture of (c) a real PLD system at working condition.

the materials at its focus point to several thousand degrees in nano-second [103]. At this high temperature, any types of materials can be vaporized. Figure 1.16(a) shows a laser beam that is focused onto a source material target, where the material is vaporized, ejected into the vacuum space and finally deposited onto the substrates. A laser beam can also be integrated with a tube furnace for nanowire growth, which can vaporize source materials or introduce certain dopants for a CVD process. A schematic of laser integrated tube furnace system is given in Figure 1.16(b) and the picture of a real system is shown in Figure 1.16(c). Because of the unique property of high-energy evaporization, PLD can maintain same stoichiometry of deposition materials as the target, which is very crucial for materials doping.
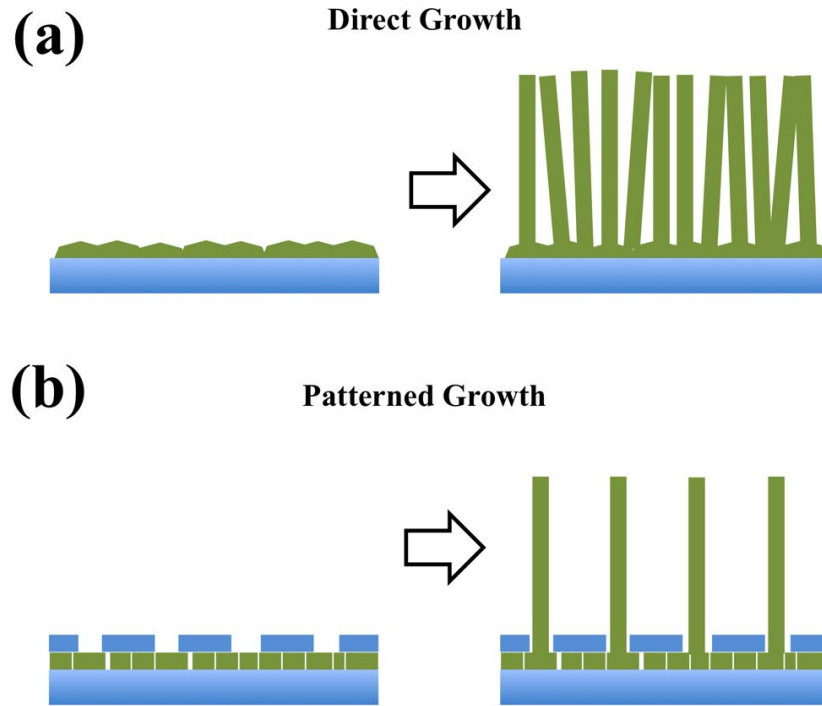
Figure 1.17: Schematics of two different types of hydrothermal growth methods. (a) Nanowires directly grown on pre-seeded substrate; (b) nanowires grown on substrate with patterned layer that defines the growth positions.

Sputtering. Sputtering, including direct-current (DC) and radio-frequency (RF) sputtering, is another well-known method that is used to generate vapor source. In the electric field, the argon ions are accelerated toward the target. The energetic argon ions bombard on the target materials and transfer their momentum to the target atoms. Through this process, the target atoms or atom clusters escape from the target and deposit onto the substrates. Though it is a very mature techniques for thin film deposition, its applications in nanowire growth are still not well explored yet.

1.4.2 Solution Synthesis of Metal Oxide Nanowire Arrays

The growth of nanowire arrays can also be realized in solution phase. Because the growth process happens in the solution, which excludes the requirements of vacuum systems, only a cap-

suled reaction container and a simple convection oven are needed. Due to the growth of nanowires is based liquid-phase chemical reaction, the growth temperature is much lower than vapor-phase methods. For some materials, the growth temperature can be as low as several tens of degree centigrade, which enable the use of flexible substrates and integration of lithographic patterned resist that can only survive at low temperature. Furthermore, solution synthesis is generally much easier to expand to large-scale production.

In this dissertation, we will emphasize the growth of ZnO nanowire arrays by hydrothermal method[†]. The ZnO nanowire array can not only play a role as active materials for gas sensing but also work as structural templates for the growth of other metal oxide nanowire arrays. Figure 1.17 shows the direct growth and patterned growth of ZnO nanowire arrays by hydrothermal method. From the schematics, no catalytic metal is used to defined the nanowire diameters and the nanowires are formed by the anisotropic growth. Due to the lack of control in lateral growth of nanowires, the diameters of ZnO nanowires prepared by hydrothermal methods generally have broader distribution than vapor-phase methods. Most importantly, the low temperature growth enables the use of e-beam patterned Poly(methyl methacrylate) (PMMA) layer to control the growth positions of the nanowires.

Figure 1.17 also illustrated the effect of seed layer on the alignment of the resulted nanowires. Well-aligned nanowire array can be obtained on the highly textured seeds. Figure 1.18 demonstrates the significant influence of the quality of the seed layer. The alignment of nanowire is very important for the fabrication and the performance optimization of gas sensors, accordingly, the preparation of high quality seeds is the key for this project. Figure 1.19 shows the highly textured seeds prepared by hydrothermal methods for subsequent patterned growth of nanowire arrays. Time serial SEM images show that isolated ZnO crystals first grew on the substrate. As the crystal grown into bigger size, they contacted to each other forming a continuous films. The cross-section view shows that the polycrystalline ZnO film is highly textured. And the majority

[†]"Hydrothermal" method is one type of solution-based method for single-crystal growth, in which water is used as the growth media. Its name origins from the natural process in geology.
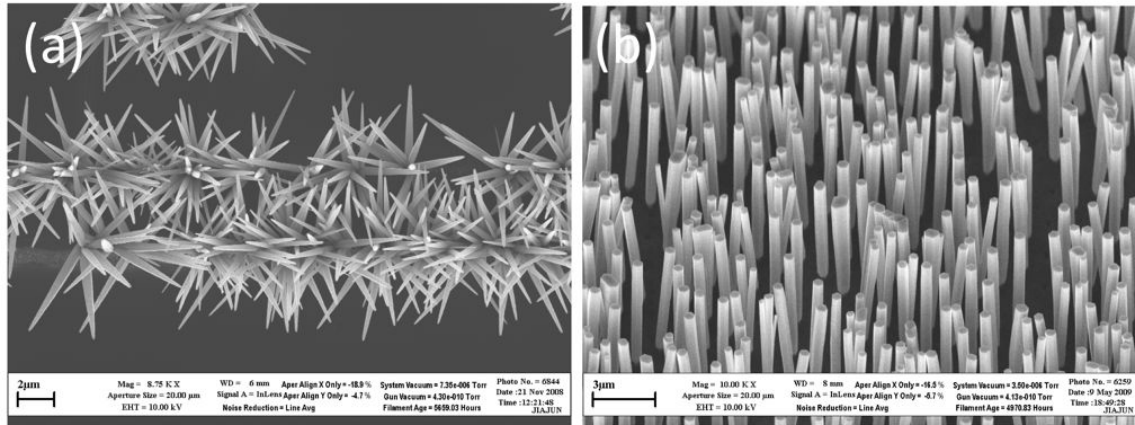
Figure 1.18: SEM images of ZnO nanowires grown on (a) randomly oriented seeds and (b) highly-textured seeds.
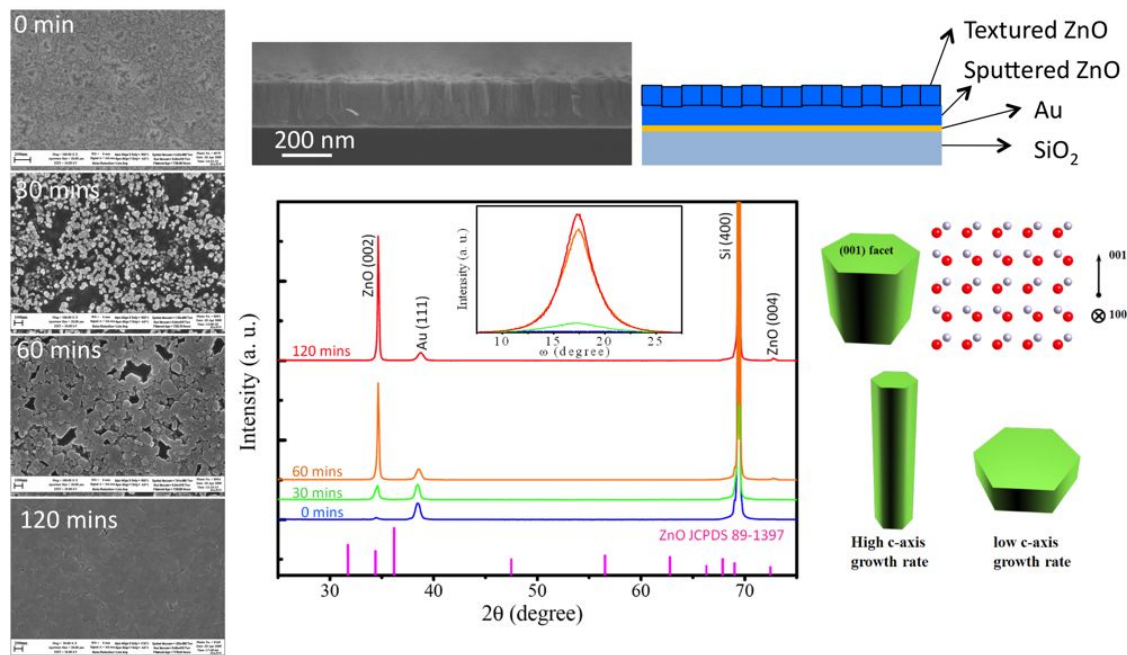
Figure 1.19: Serial SEM and X-ray diffraction (XRD) analysis of ZnO seed layers. A diagram is also given to explain the growth process of textured seeds.

30
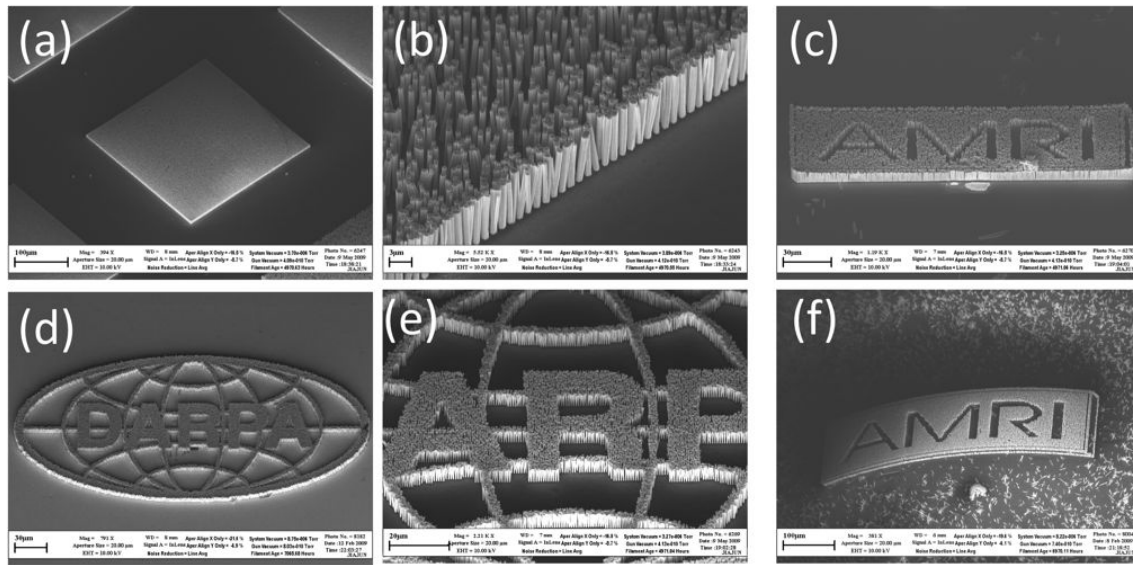
Figure 1.20: SEM images of nanowire arrays grown on different patterned substrates. (a-b) Si/SiO$_2$ substrates; (c-e) transparent conductive oxide (TCO) substrates; (f) Kapton flexible substrate.

of the ZnO crystals are *c*-axis oriented according to the X-ray diffraction (XRD) analysis. The textured growth of ZnO crystals can be ascribed to the suppressed growth rates along *c*-axis. The polarized surfaces of ZnO crystals, (0001) and $(000\bar{1})$, have high energy than other facets. The high growth rate along *c*-axis help to reduce the area of the polarized surfaces. Introducing a layer of gold can neutralize the polarized surfaces and suppress the *c*-axis growth. The tilted ZnO crystals at the initial growth tend to be blocked by the *c*-axis oriented crystals that have high lateral growth rate. Through this process, textured ZnO seed layer can be formed on any non-epitaxial substrate. And furthermore, this type of seed layer can even growth on plastic substrates due to the low-temperature nature of hydrothermal growth.

Figure 1.20 shows typical arrays grown by using highly textured seeds and e-beam lithography patterning on various non-epitaxial substrates (Si/SiO$_2$, TCO, and Kapton). The SEM observations indicate the nanowire positions can be defined by the e-beam patterned PMMA layer and the nanowire arrays show good alignment on the textured seed layer.

1.5 Objectives of the Dissertation

As mentioned in previous sections, electronic gas sensors with performance surpass the biological olfactory systems are highly pursued for many applications.In recent years, research efforts on the applications of nanomaterials for highly sensitive gas detection have obtained lots of promising results [75, 78, 104]. In this dissertation, we propose to use 3D metal oxide nanowire arrays to create highly sensitive and selective gas detection devices. The dissertation will address the fabrication of 3D nanowire array sensors as well as the modification of nanowire surfaces for selective detection. The major objectives of the dissertation are summarized as follows:

- Adapting versatile metal oxide nanowire arrays for sensing device fabrication and overcoming the obstacles that hinder the preparation of 3D nanowire array gas sensors;

- Exploring new routes for the fabrication of 3D well-aligned metal oxide nanowire arrays, which expands the material library for gas sensing;

- Employing multiple nanowire-array devices to create prototype electronic noses with high sensitivity and selectivity for gas detection and discrimination.

Chapter 2

Gas Detection by Standalone Vertically Aligned Nanowire Arrays

It is impossible to create high performance electronic noses that consist of multiple gas sensors without detailed investigation on the preparation and performance of individual gas sensors based on metal oxide nanowire arrays. In this chapter, standalone gas sensors based on 3D metal oxide nanowire arrays will be introduced. Not like lateral nanodevices that are compatible with conventional processes for microelectronics, exploration in fabrication methods is needed for nanosensors based on 3D nanostructured materials. In the first section, monoclinic WO_3 nanowire array is prepared by thermal evaporation and multiple step microfabrication is used to connect the nanowires forming conductometric gas sensors. The sensors show highly sensitive to NO_2 and H_2S. In the second section, well-aligned CuO nanowire arrays are grown on Cu foil by thermal oxidization are studied in details. The gas sensors were prepared by novel *in-situ* micromanipulation under a field emission scanning electron microscope (FESEM). Though the sensing responses are irrecoverable when exposed to H_2S with high concentration, the detection mechanism is novel and may be applied for high performance gas detection.

2.1 Gas Sensors Based on Monoclinic WO_3 Nanowire Array Prepared by Microfabrication[1]

2.1.1 Background

Tungsten oxides are multi-functional materials with many unique properties (e.g. electrochromic, gasochromic, and gas sensing properties) for various applications including smart windows, highly sensitive gas sensors, field emitters, etc [105–109]. Especially, tungsten oxides are widely used as active materials in many conductometric gas sensors due to their large conductivity change when exposed to targeting gas vapors. Nanocrystalline tungsten oxide thin films have showed high sensitivity to environmental toxic gases, such as NH_3, H_2S, and NO_2 [110–113]. Recently, the fabrication of tungsten oxide nanowires has attracted more and more interest from gas sensor society due to their confined conduction channels, large surface area and large surface-to-volume ratio that may significantly enhance the sensor performance. The fabrication of tungsten oxide nanowires is relatively difficult compared with other well-reported metal oxide nanowires, such as ZnO, In_2O_3, SnO_2, etc., because of high melting points of tungsten oxides. And most of the reported tungsten oxide nanowires are generally with composition of $W_{18}O_{49}$ [72, 114]. The $W_{18}O_{49}$ nanowires will transform into monoclinic WO_3 at temperature above 500 °C and monoclinic WO_3 is stable phase up to 1000 °C implying the applications of high temperature sensors.

The successful fabrication of monoclinic WO_3 nanowire array on silicon wafer provides an important platform for the gas detection based on 3D nanostructures of high performance sensing materials. The materials fabrication, device preparation, and device performance will be introduced in the following section.

---

[1]Partial of this section is reprinted by permission from Royal Society of Chemistry. Please check Appendix D. http://dx.doi.org/10.1039/b816646c

2.1.2 Growth of Monoclinic WO_3 Nanowire Arrays and Gas Senor Fabrication

The monoclinic WO_3 nanowire arrays were prepared by conventional thermal evaporation. The configuration of the system is similar to that shown in Figure 1.15. In a typical synthesis, 2 g tungsten powder (12 μm, 99.9 %, Sigma-Aldrich) was loaded into the center of the tube furnace, acting as a source material. Silicon substrate (1 cm $\times$ 3 cm) was cleaned by alcohol and deionized water in an ultrasonic cleaner, then positioned at the low temperature zone, 20 cm downstream of the source material. After the quartz tube was pumped down to a vacuum of 500 mTorr, the temperature of the tube was increased from room temperature to 1000 $^\circ$C at a ramping rate of 50 $^\circ$C/min. During the whole heating process, constant air flows of 20, 100 or 200 sccm, respectively, were introduced for each experiment and pressure inside the tube was kept at 13 $\sim$ 15 Torr in order to explore an optimum synthesis condition for nanowire array growth. After grown for 1 hr, the furnace was naturally cooled to room temperature by switching off the heating power. The as-prepared products on Si substrates were characterized by Carl Zeiss 1530 VP field emission scanning electron microscopy (FESEM), Philips Xpert-MPD X-ray diffraction (XRD), JEOL 2010 transmission electron microscopy (TEM), and energy dispersive spectroscopy (EDS) attached on the TEM.

A large area and quasi-aligned tungsten nanowire array was successfully synthesized under a pressure of 13 $\sim$ 15 Torr with an air flow of 200 sccm at a temperature of 1000 $^\circ$C. Figure 2.1 shows typical FESEM images of an as-synthesized nanowire array grown on Si substrate. Nanowires are distributed evenly with the length of about 3 $\sim$ 5 μm as shown in the top view of Figure 2.1(a) and cross-sectional view of Figure 2.1(b), respectively. In fact, the nanowire array grows out from a thin layer of tungsten oxide nanoparticles formed prior to the nanowire growth shown in the insert of the enlarged interface in Figure 2.1(b).

The XRD pattern of tungsten oxide nanowires is shown in Figure 2.2. The diffraction peaks
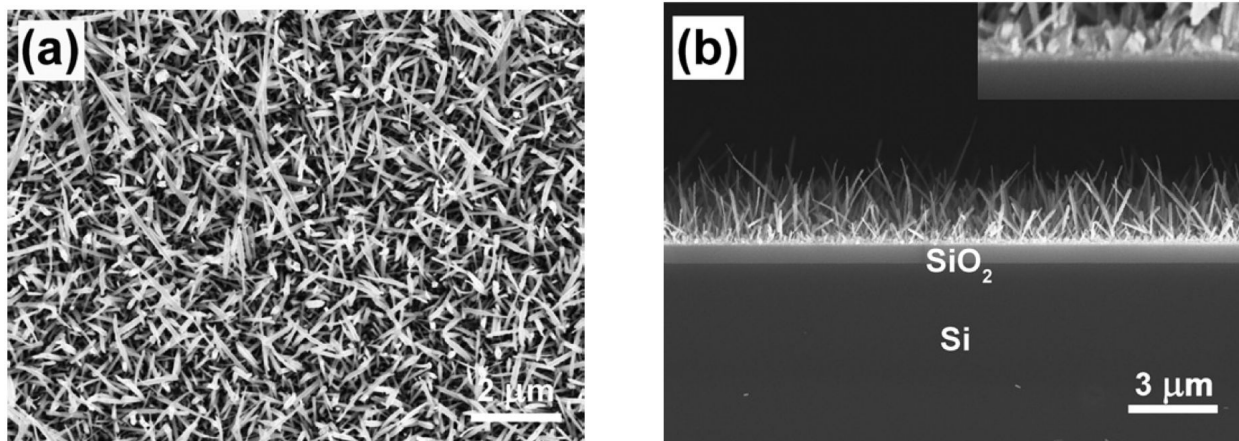
Figure 2.1: SEM images of a WO$_3$ nanowire array grown on a Si substrate from a top view (a) and a cross-sectional view (b). [115]

can be well indexed to a monoclinic WO$_3$ phase with unit cell parameters as $a = 0.7297$ nm, $b = 0.7539$ nm, $c = 0.7688$ nm, $\beta = 90.91°$ (JCPDS 43-1035). In the XRD pattern, the (002) diffraction peak is the strongest reflection, indicating the (002) is the preferential growth plane of the nanowires. The strong peak marked by a star in the pattern is from the Si substrate. It is apparent that the tungsten oxide synthesized in our experiment is WO$_3$ phase, other than W$_{18}$O$_{49}$ which was further confirmed by TEM investigation.

Figure 2.5(a) presents a low magnification TEM image of the nanowires with a diameter around $40 \sim 50$ nm. Figure 2.5(b) is the high resolution electron image (HREM) of the nanowire along [100] zone from the rectangular area in Figure 2.5(a), in which the lattice spacings are measured to be 0.385 nm and 0.379 nm along two orthogonal directions, corresponding to the (002) and (020) planes of monoclinic WO$_3$, respectively. The selected-area electron diffraction pattern (SAED) proves the nanowire is single crystalline with the growth plane parallel to (002), as shown in the inset in Figure 2.5(b). Furthermore, EDS analysis shows the atomic ratio of W and O are close to 3:1. The C and Cu peaks are from the copper grid in the EDS spectrum. From the XRD and TEM analysis, it can be further concluded that the WO$_3$ nanowires are single monoclinic crystalline with growth plane parallel to the (002) plane.

36
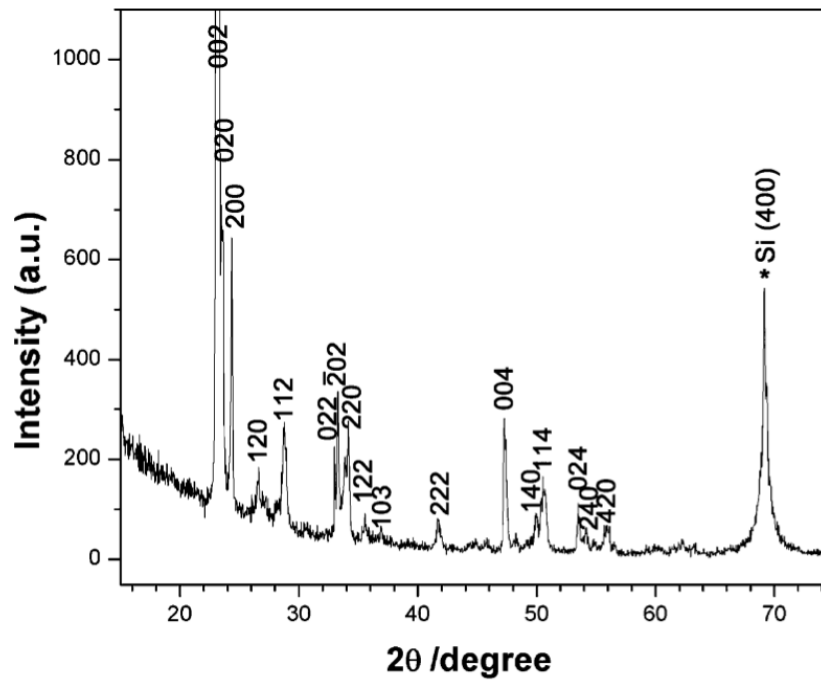
Figure 2.2: XRD spectrum of the WO$_3$ nanowire array grown on Si substrate. [115]

No catalyst droplets were found on the tips of tungsten oxide nanowires indicating the whole synthesis process follows the vapor-solid (VS) mechanism [67]. Generally, gas-phase supersaturation in VS growth is a most determining factor for the formation of different nanostructures, which is influenced by source materials temperature, tube pressure, gas flow rate, etc. Therefore, a series of experiments were performed to investigate the optimum growth conditions. It is found that relatively low pressure (13 $\sim$ 15 Torr), moderate temperature (1000 $^\circ$C), and high air flow rate (200 sccm) are able to produce a suitable gas-phase supersaturation for nanowire array growth. During the heating, the color of the source materials changed from dark gray to orange-reddish, accompanied with an obvious volume increase. Owing to the sufficient oxygen introduced from the air flow, WO$_3$ species were directly carried down stream, forming WO$_3$ nanowire arrays on the Si substrate. No catalysts were observed at the tips of the nanowires by SEM or TEM. It should be noted that a layer of WO$_3$ nanoparticles, acting as a seed layer, was formed prior to the nanowire array growth.
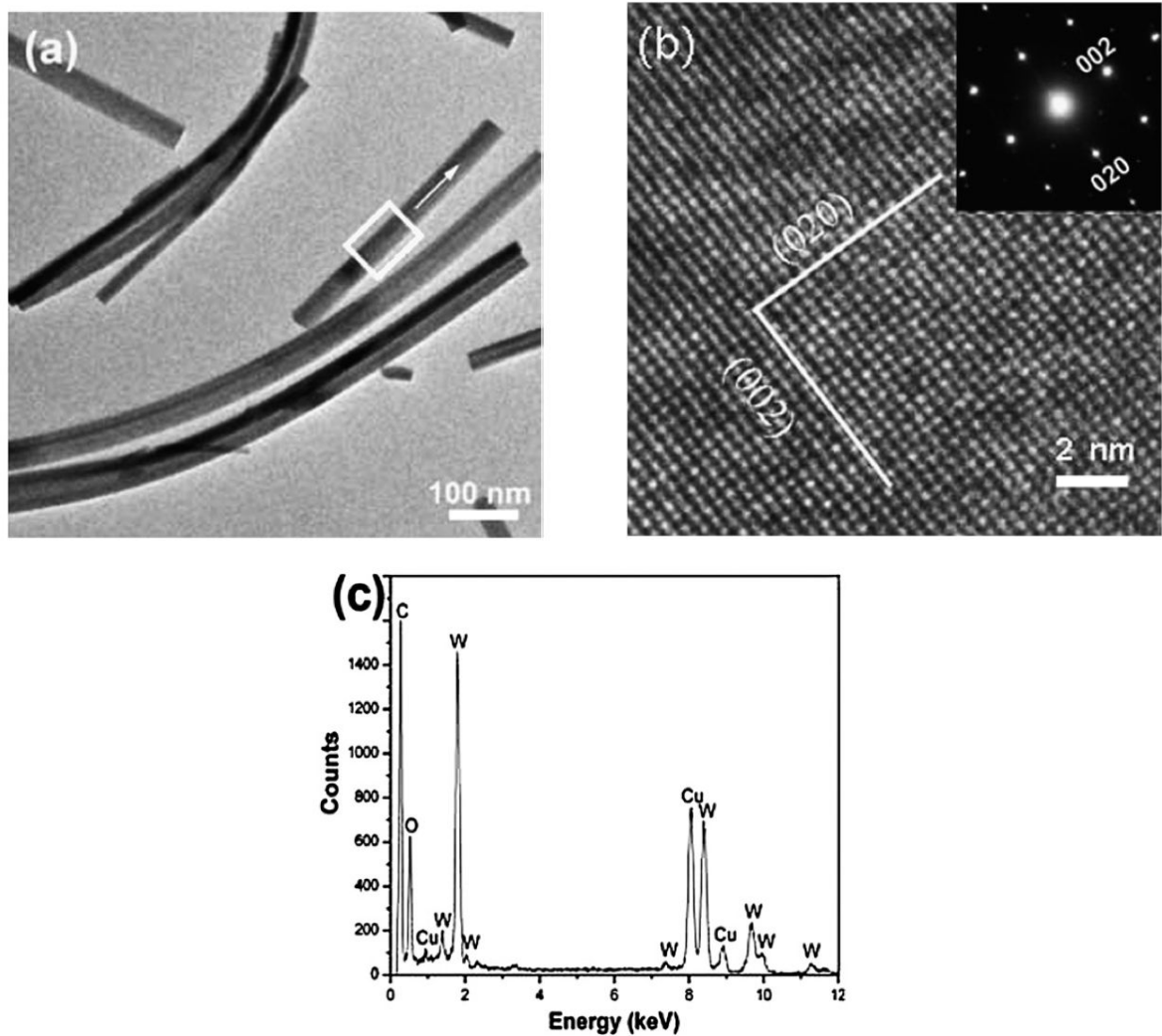
Figure 2.3: (a) A typical low magnification TEM image of tungsten oxide nanowires. (b) [100] HREM image of a tungsten oxide nanowire denoted by the white rectangle in (a). The inset shows the corresponding SAED pattern. The white arrow in (a) indicates the growth direction of the nanowire. (c) EDS spectra of the as-prepared nanowires reveal that nanowires consist of W and O. The C and Cu elements are from the TEM copper grids. [115]

2.1.3 Sensing Performance of Gas Sensors Based on Monoclinic WO_3 Nanowire Arrays

The nanowire array gas sensor was prepared by a multiple-step photolithography process [116] and the sensor was mounted on a heating stage connected to the electrical feedthrough in a test-
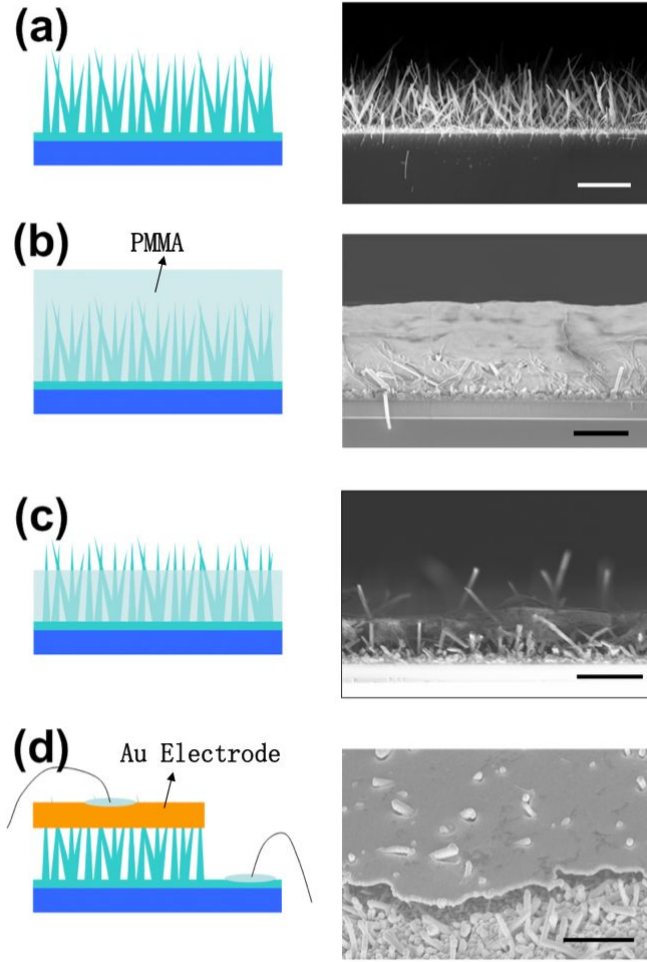
Figure 2.4: Schematics and SEM images showing the procedures to prepare a gas sensor based on WO$_3$ nanowire array. All the scale bars are 4 μm. [115]

ing cell for sensor measurements. The gas testing experiments of the sensor under air-diluted NO$_2$ were conducted at 180 °C using a Keithley 2400 source meter. A gas sensor was prepared based on this WO$_3$ nanowire array and the schematic diagram and corresponding SEM images of the preparation process are shown in the Figure 2.4. A layer of 8 μm polymethyl methacrylate (PMMA) Resist (950A4, Microchem Inc.) was first coated on the nanowire array by spin coating, shown in Figure 2.4(b). After the heat treatment on the PMMA resist, the nanowire array was loaded to an oxygen plasma etching machine (SPI Plasma Prep II). A 100 W input power resulted in an etch rate of 0.08 μm/min, and after 75 min etching, 2 microns of PMMA was left and the tips of the
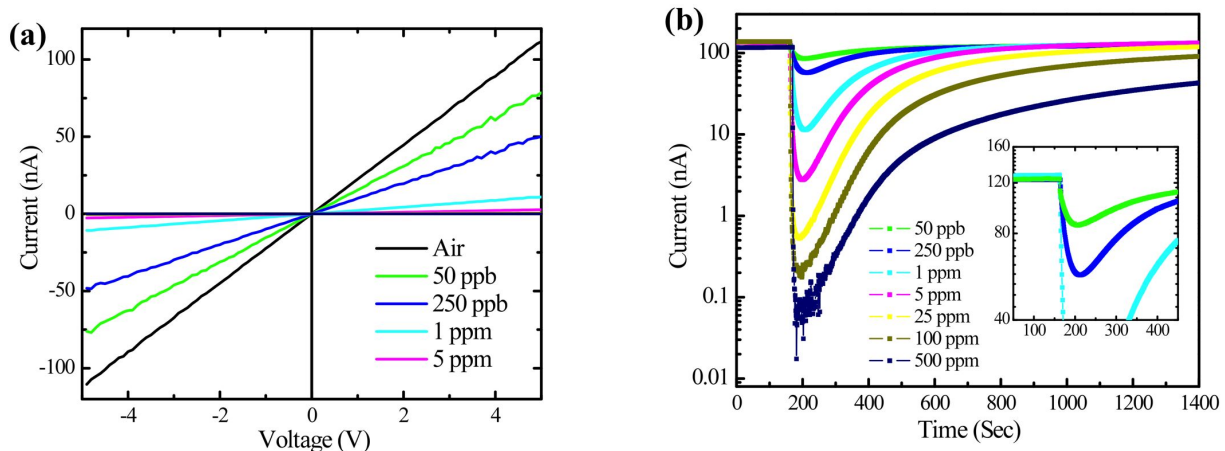
Figure 2.5: (a) *I-V* curves of gas sensors based on the WO_3 nanowire array being exposed to air-diluted NO_2 with different concentrations. (b) Sensing response curves of the sensor. [115]

nanowires were exposed to the environment [Figure 2.4(c)]. By using sputtering and a metal mask, a 100 nm gold layer with 2 mm × 2 mm area was coated onto the residue PMMA and connected to the tips of the nanowires. After that, the nanowire array was soaked into acetone, isopropyl alcohol, and deionized water, successively, to remove the PMMA. Finally, the sensor was dried by slow nitrogen flow. Silver paste was used to make connections from the testing system to the bottom layer and the top gold electrode [Figure 2.4(d)]. By applying a voltage on the top electrode, current flowing through the nanowires could be provided and all of the nanowires were exposed to the atmosphere.

The sensor was first stabilized at 180 °C in pure air. *I-V* curves were obtained when air-diluted NO_2 with different concentrations were introduced into the gas sensor testing cell, as shown in Figure 2.5(a). All the *I-V* curves are linear, implying ohmic contacts were formed between the deposited Au and WO_3. The sensor can detect NO_2 with a concentration down to 50 ppb. When the sensor is exposed to 50 ppb NO_2, the resistance of the sensor increased to about 37% from 45.5 MΩ to 62.5 MΩ. Even at a relatively low concentration, 5 ppm, the resistance change can be as high as 3400% from 45.5 MΩ to 1.6 GΩ. The sensing response curves to air-diluted NO_2 are plotted in Figure 2.5(b). The sensor showed immediate response to NO_2, the typical response

40

times are less than 30 s; however, it took a relatively long time for the sensor recovery, generally more than 800 s, and it increased as the exposed concentration increased. The response curves for the low concentrations are also plotted in the inset of Figure 2.5(b), which indicates that the response signal was much larger than the background noise level, even at a concentration as low as 50 ppb and can be easily identified. Therefore, the sensor presents high sensitivity to detect NO_2 gases, which might be attributed to the large surface area of the nanowire array and intrinsic properties of the monoclinic WO_3 nanowires.

WO_3 is an n-type semiconductor. Adsorbing oxidizing gas molecules, such as O_2 and NO_2, to its surface, can induce surface states that trap electrons and result in depletion of carrier on the material surface. For nanowires, forming a carrier depletion layer will reduce the effective cross area for carrier transport and cause reduced current in our constant voltage bias measurement. Considering that the nanowires are resistors with parallel connection, overall resistance increase in our device requires the gas to cause resistance increase in most of the nanowires. Since the response speed of this sensor is very fast, gas diffusion into the nanowire array sensor must be very effective so that it can induce a resistance increase in most nanowires in a short time. Though the response trend is the same as other WO_3 based sensors [109, 117], the unique parallel connection with large surface area provides a new route to fabricate highly sensitive gas sensors.

2.1.4 Summary

In summary, a large area WO_3 nanowire array with diameters ranging from 40 to 100 nm and lengths up to 5 μm was synthesized on Si substrate using a convenient thermal evaporation method at a relatively low temperature. The nanowire grew on top of WO_3 nanoparticle seed layers, forming a quasi-aligned nanowire array. The nanowires were single crystalline with monoclinic structure. The nanowire array gas sensors were also fabricated using a multiple step photolithography method. Gas sensing tests revealed that the sensor based on the WO_3 nanowire array had the capability of detecting NO_2 concentrations as low as 50 ppb, demonstrating a promising application

41

in the field of low concentration gas detection.

2.2 CuO **Nanowire Array Sensor Prepared by *In-situ* Manipulation**[2]

2.2.1 Background

Conventionally, many metal oxide sensing materials present *n*-type properties due to naturally formed oxygen vacancies, for instances, the well-known SnO_2, In_2O_3, TiO_2, WO_3 are all intrinsic *n*-type semiconductors [66]. CuO is one of the few metal oxide semiconductors that have *p*-type properties, which is majorly caused by the Cu ions vacancies [118]. Recently, the applications of *p*-type CuO in gas sensing have attracted more attention because of the enhancement of selectivity in conventional metal oxide gas sensors when incorporating with *n*-type metal oxides. In thin-film based gas sensors, CuO particles generally work as additives enclosed in *n*-type metal oxides, like SnO_2, forming *p-n* junctions at the interfaces of the particles. These *p-n* junctions effectively alter the depletion layer thickness. This effect has provided a significant performance improvement of SnO_2 gas sensors targeting H_2S [119].

CuO has many applications in the detection of H_2S due to the room temperature reaction between the CuO and H_2S forming a layer of metallic CuS on the surface. Because CuS has much higher conductivity than that of CuO, the material conductivity may be effectively increased when exposing to H_2S gases. Moreover, H_2S is one of the most common environmental toxic gases that may widely present in industry and city sewerage system where the gases tend to accumulate to high concentrations due to their higher molecular weight than air. The H_2S gas can dispart human's nervous system at very low concentrations. Therefore, gas sensors that can detect H_2S with high sensitivity and selectivity is highly pursued and have a broad perspective in industrial and civil applications.

Low cost fabrication of vertically-aligned CuO has been reported, in which Cu foils were di-

rectly oxidized in atmosphere [120]. These well-aligned CuO nanowire array is a very good candidate for the H$_2$S detection. However, this type of CuO nanostructures is not compatible with conventional microfabrication methods because the high flexibility of nanowires and the brittle supporting substrates cannot survive the capillary force from the photoresists. In this section, a integration method that constructs gas sensors based on CuO nanowire array with *in-situ* manipulation in a FESEM is introduced. The gas sensors can detect 500 ppb H$_2$S with little responses toward inferences, such as H$_2$, CO and NH$_3$. This method may be expanded to fabrication of other type of 3D nanostructured devices.

2.2.2 Fabrication of CuO Nanowire Array Gas Sensors by *In-situ* Manipulation

A vertically aligned CuO nanowire array was prepared by heating the copper foil in air, which was reported by Xia *et al* [120]. Generally, heating the copper foil at 500 °C can produce well-aligned CuO nanowires with diameters in the range of 80 $\sim$ 200 nm. By adjustment of the heating time, the length of nanowires can be controlled. In our case, the heating time is 5 h, and after the cooling procedure, flakes of nanowire arrays split from the substrate due to the mismatch of thermal expansion between the CuO and the copper substrate. The size of as-prepared nanowire array can be as large as 10 mm × 10 mm. The flake of array was cut into a square shape with the size of 2 mm × 2 mm for structure characterization and device assembly. The morphology and composition were characterized by a Carl Zeiss 1530 VP field emission scanning electron microscope (FESEM) equipped with Oxford X-ray energy dispersive spectroscopy (EDS), and the crystal structures were analyzed by FEI Tecnai F20 field emission transmission electron microscopy (TEM).

Figure 2.6 shows the morphology and crystal structure of the as-grown CuO nanowire array. Parts a and b of Figure 2.6 are the tilted view (15 °) and the cross-sectional FESEM images, respectively. The length of the nanowires is in the range of 4 $\sim$ 8 μm, and the thickness of the supporting foil is about 3 μm. The low-magnification TEM image of a single CuO nanowire is
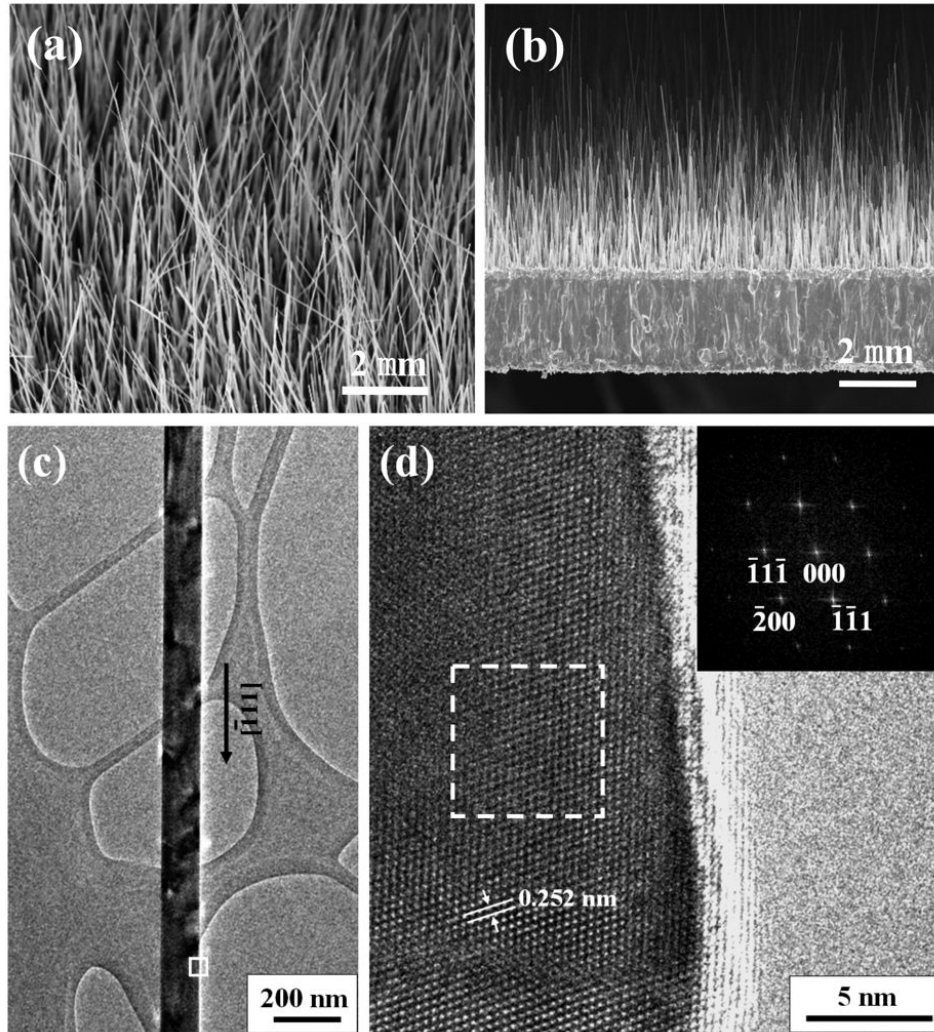
Figure 2.6: (a) SEM image of a CuO nanowire array grown by direct oxidation of Cu foil. (b) Cross-sectional view of the CuO nanowire array, showing the length of the nanowires in the range of 4-8 μm and the thickness of the supporting foil to be about 3 μm. (c) TEM image of a single CuO nanowire, the diameter of which is about 150 nm. (d) High-resolution TEM image of the boxed area in part c shows that the nanowires are single crystalline and no second phase is identified on its surface. The electron beam is along [110] axis of monoclinic CuO. The inset is the corresponding FFT pattern of the boxed area in part d. [121]

shown in Figure 2.6(c). Its diameter is about 150 nm. The diameters of most nanowires are found in the range of 80 $\sim$ 200 nm through TEM measurements. Figure 2.6(d) is a high-resolution TEM image along [110] zone axis, and the inset is the fast Fourier transform (FFT) pattern. The nanowires are single crystalline with monoclinic structure and growth direction along $\left[1\bar{1}1\right]$ axis.

44
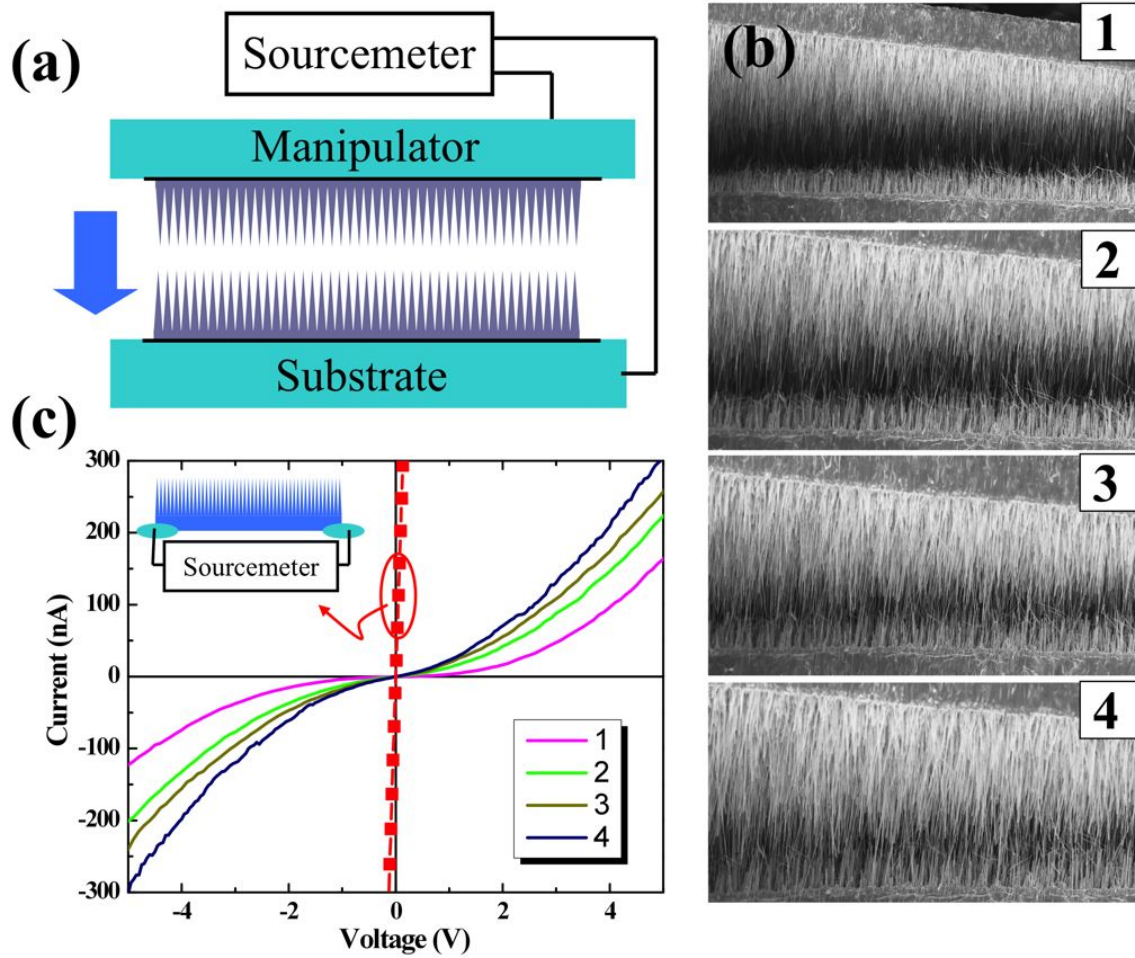
Figure 2.7: Assembly processes of CuO nanowire arrays. (a) Schematic diagram, demonstrating the setup used to assemble two vertically aligned CuO nanowire arrays into a three-dimensional nanostructure. Two pieces of nanowire arrays (2 mm × 2 mm) were attached to the copper plate and the micromanipulator tip (copper wire). By activation of the manipulator, the distance between the two arrays can be adjusted. (b) *In-situ* observation of the assembly process when pushing one nanowire array to the other. (c) *I-V* curves measured at different stages of the assembly process by a source measurement unit. The *I-V* curve of a nanowire array connected by silver paste is also plotted, which is indicated by square symbol line. [121]

The sensors were assembled by Kleindiek MM3A-EM micromanipulator, which were installed on the stage of the FESEM. The assembly process was performed and controlled through *in situ* FESEM imaging, and the *I-V* characteristics at different stages were also obtained by a Keithley 2400 sourcemeter.

A square piece of (2 mm × 2 mm) CuO nanowire array was attached to the thin copper plate,

and the other piece was mounted on the micromanipulator tip with silver paste for the chemical sensor fabrication. They were placed face to face and slowly pushed together by the micromanipulator. The space inbetween was monitored through the FESEM screen. Because of the accurate positioning capability of micromanipulators, short-circuits from the top electrode to bottom electrode were avoided, which increased the stability of the sensors. The schematic diagram of the assembly process is given in Figure 2.7(a), and the real-time captured FESEM images are shown in Figure 2.7(b). As one nanowire array approached to the other, more and more nanowires get connected, and the resistance of the whole sensor reduced as implied by the increased slope in I-V curves as shown in Figure 2.7(c). The I-V curves show nonlinear characteristics indicating that an energy barrier formed at the current flow path. To investigate the contact properties between the silver paste and CuO, a piece of CuO nanowire array was glued onto a 600-nm SiO_2-coated silicon substrate using two drops of silver paste, the configuration of which is shown in the inset of Figure 2.7(c). The I-V curve of the connections on the same CuO nanowire array flake was plotted as a square symbol line in Figure 2.7(c), illustrating linear properties with much lower resistance than those with current passing through the nanowires, implying good ohmic contact between the CuO and silver paste. Thus, the nonlinear I-V properties of the sensors should be attributed to the contacts of the adjacent CuO nanowires, these contacts also contributed to the majority of the device resistance.

2.2.3   Sensing Performance of CuO Nanowire Array Gas Sensors

After the assembly, the sensor was taken out of the FESEM chamber and mounted on a heating stage that connected to the electrical feed-through of a gas sensor testing cell. The sensing response was monitored by measuring the current change under a constant applied voltage (0.5 V). The sensor responses are characterized by the normalized currents I/I_0 as plotted in Figure 2.8 and in Figure 2.9 for room temperature and elevated temperature (160 °C), respectively. At room temperature, the sensor responded to H_2S at a concentration of 100 ppm; no significant response
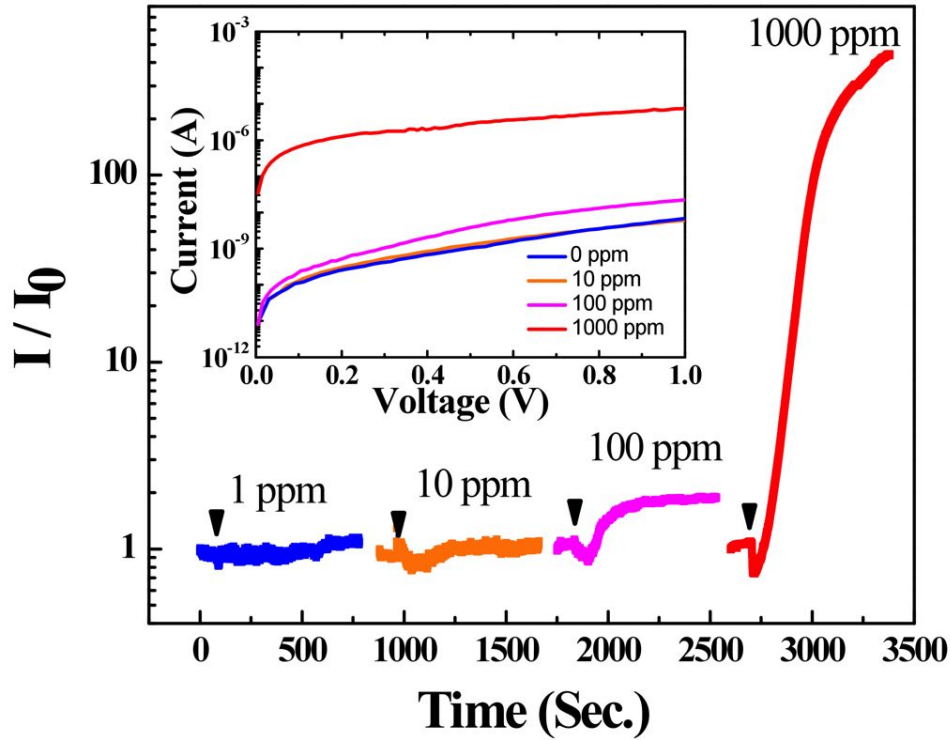
Figure 2.8: Sensing response of a CuO nanowire array sensor to air-diluted H_2S at room temperature. The inlet times are indicated by solid triangle symbols. No obvious response was observed at concentration lower than 10 ppm, and the sensors were unrecoverable when exposed to diluted H_2S with concentration higher than 100 ppm. All the response curves were obtained by measuring the current variation under a constant voltage (0.5 V). The inset shows the semilog *I-V* plots measured after exposure to H_2S with different concentrations. [121]

was observed at the concentration lower than 10 ppm. The response (I/I_0) to 1000 ppm H_2S can be as high as 400 times. However, the change of the resistance can not be recovered even after the H_2S was completely pumped out from the testing system and pure air was introduced. The inset of Figure 2.8 is the semilog *I-V* plots of the sensor before and after exposure to H_2S having different concentrations. The plots show that at 1000 ppm, H_2S induced nearly 3 orders of magnitude of conductivity change. The lowest detectable concentration was enhanced to 500 ppb when the sensor temperature was increased to 160 °C. The response was recoverable if the H_2S concentration was lower than 1 ppm. However, when the concentration went to higher than 5 ppm, the response became unrecoverable. Six sensing response curves were recorded successively
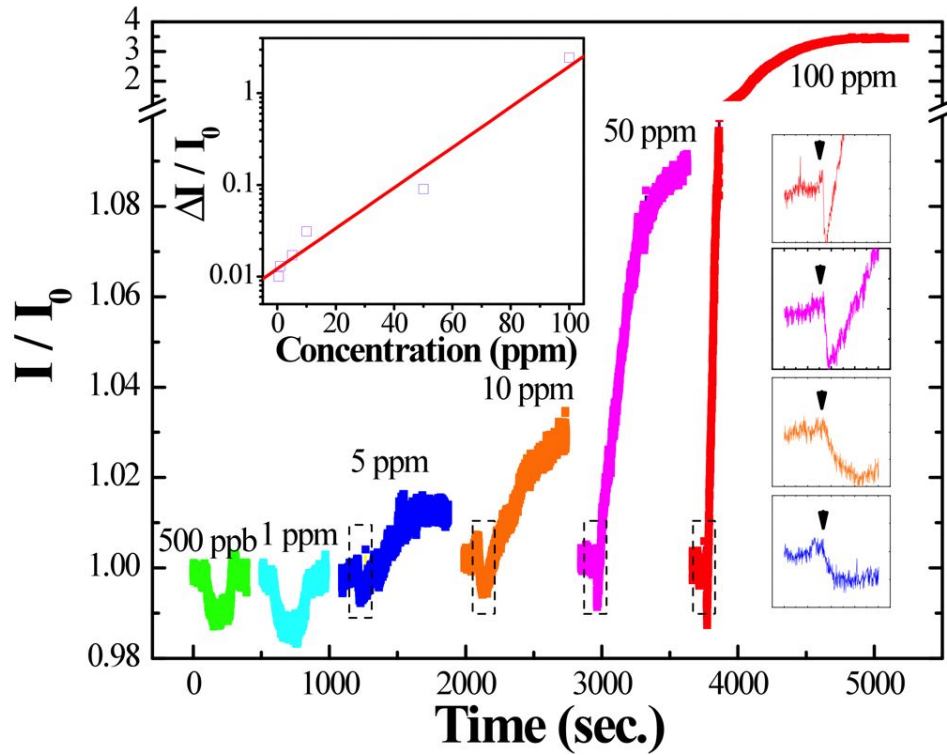
Figure 2.9: Sensing response of a CuO nanowire array sensor to air-diluted H_2S at elevated temperature (160 °C). The sensor can detect H_2S with concentration as low as 500 ppb. However, when the concentration was higher than 5 ppm, the sensor became unrecoverable. The initial responses for concentrations higher than 5 ppm are enlarged in square boxes. The time when air-diluted H_2S was inlet is also indicated by triangle symbols. The inset plots the concentration dependence of the normalized sensor responses ($\Delta I/I_0$). [121]

by introducing H_2S with concentrations from 500 ppb to 100 ppm, as shown in Figure 2.9. It is important to note that all the measured currents presented an immediate drop after the H_2S was introduced. If the concentration is lower than 1 ppm, the reduced current can be maintained; if the concentration is higher than 5 ppm, the current increased after the initial drop. Considering the opposite trends of current change, different mechanisms may be applied for the low and high concentration cases.

To reveal the reason why the sensor became unrecoverable after exposure to high concentrated H_2S, FESEM was employed to investigate the surface of the nanowires before and after the sensing response measurement upon 100 ppm H_2S, as shown in Figure 2.10. Exposure to the high con-
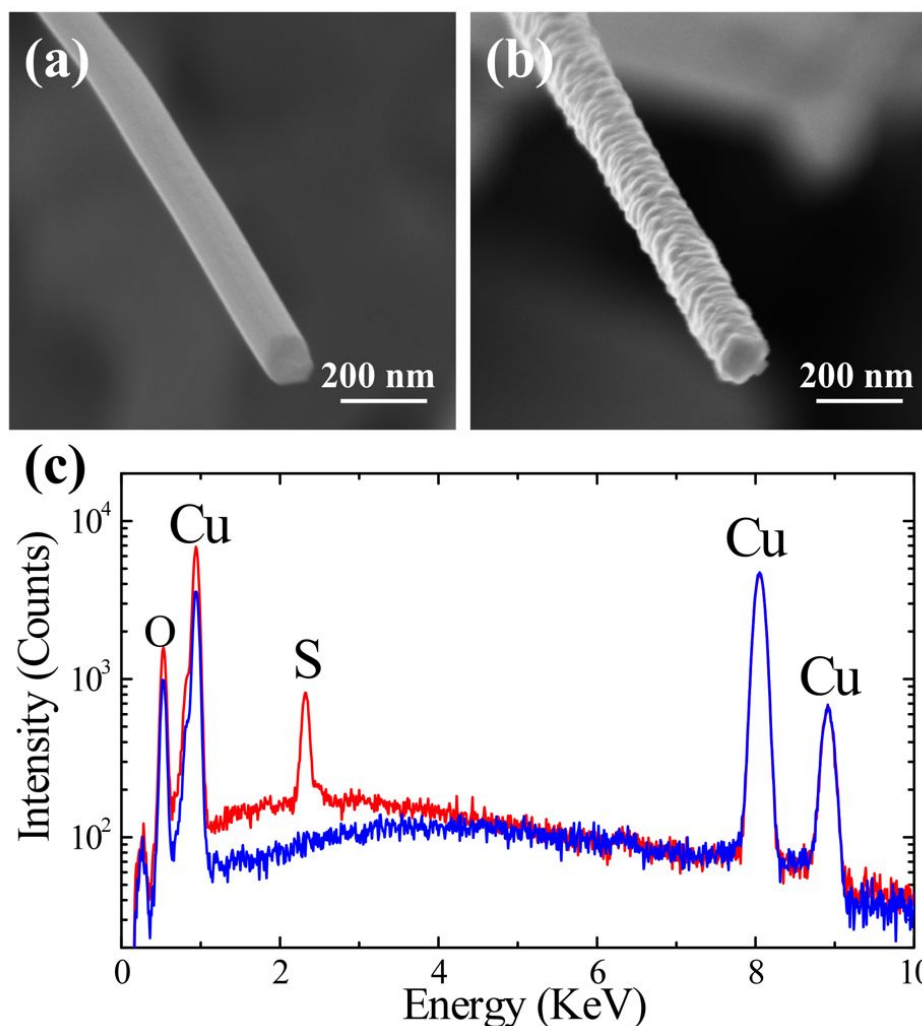
Figure 2.10: SEM images taken (a) before and (b) after exposure to 100 ppm H_2S. (c) EDS spectra of the nanowire before (dashed line) and after (solid line) the test. [121]

centrated H_2S generated obvious change in the surface roughness. From the EDS analysis (Figure 2.10(c)) and previously reported CuO based H_2S sensors [122], the following reaction is expected on the CuO nanowire surfaces

$$H_2S + CuO \rightarrow CuS + H_2O. \qquad (2.1)$$

Forming a layer of metallic CuS [123] on the surface of CuO nanowires may significantly change the contact barrier between two adjacent CuO nanowires. The contact energy barriers can
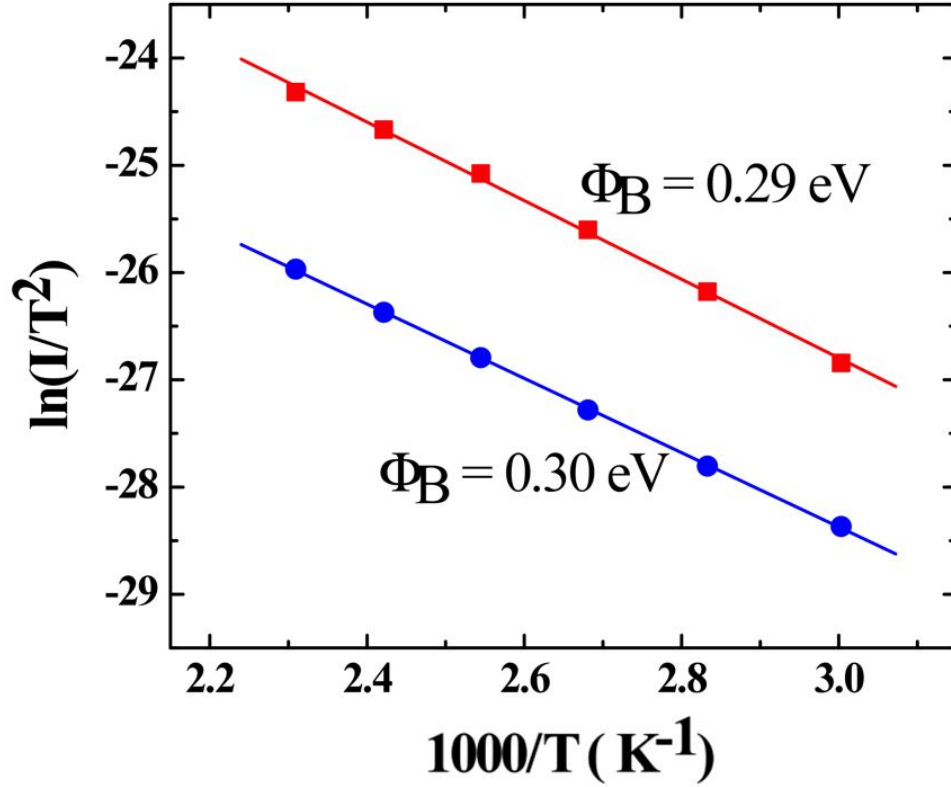
Figure 2.11: $\ln(I/T^2) - 1000/T$ plots at the 0.001 V bias. The plot with solid circles is before the H_2S exposure, and the one with solid squares is after the exposure to 100 ppm H_2S. The energy barrier heights are calculated from the slopes of the least-squares fits. [121]

be deduced by measuring the current change caused by thermal excitation, given by [124–126]

$$I = SA^*T^2 \exp(-q\Phi_B/kT), \tag{2.2}$$

where S is the contact area, A^* is Richardson Constant, $q\Phi_B$ is the effective barrier height, k is the Boltzman constant, and T is temperature. This relationship is only valid at small applied bias across the energy barrier. By plotting the relation between $\ln(I/T^2)$ and $1/T$ at the small bias (0.001 V was applied in our measurements), as shown in Figure 2.11, the slopes of the least-squares fits represent the effective barrier height across the contacts. Surprisingly, forming a layer of CuS on the CuO nanowire surface after exposure to high concentrated H_2S did not effectively alter the barrier
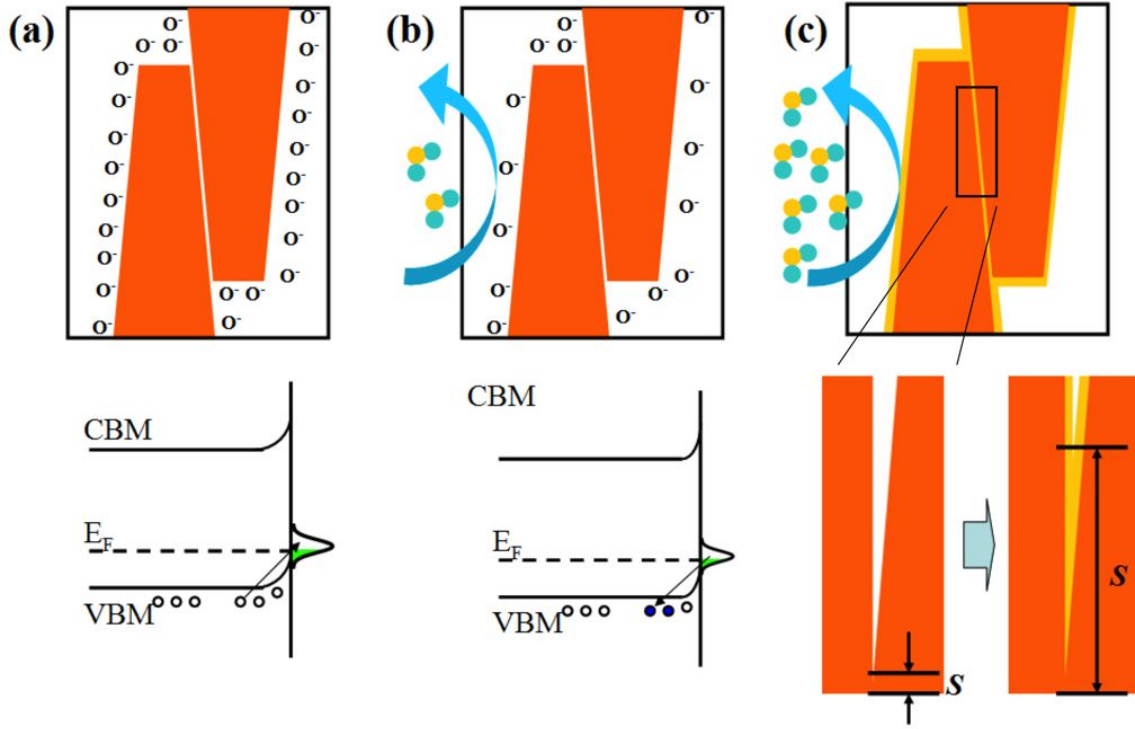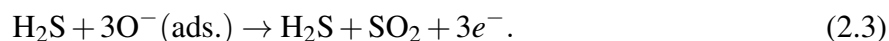
Figure 2.12: Schematics and band diagrams showing different stages before and after the sensors were exposed to H$_2$S gas. The drawing indicates the contacting area between two adjacent nanowires. (a) Before the H$_2$S exposure, the CuO nanowires adsorbed the oxygen from air and formed surface states. These surface states allowed electrons with relative low energy to be excited from valence band maximum (VBM) and induced more holes in p-type CuO nanowires. (b) When H$_2$S gas was introduced, low concentrated H$_2$S reached CuO nanowires and H$_2$S molecules reacted with the oxygen adsorbates and released electrons back to the VBM, thus decreasing the number of holes. (c) At high concentrated H$_2$S, H$_2$S reacted with the CuO nanowires and formed CuS layers on nanowire surfaces, therefore, increasing the effective contact area (indicated by S) between the adjacent CuO nanowires. [121]

height. However, we do see obvious increase of conductivity after the exposure. On the basis of the thermal excitation equation above, the phenomena can be understood by changing the effective contact area accomplished by introducing the CuS layer. Because of this special detection process based on the chemical reaction at the nanowire-to-nanowire interfaces, the sensing response exhibited exponential dependence on the concentration of H$_2$S (shown in the inset of Figure 2.9), and no saturation was observed for concentrations lower than 100 ppm. This exponential relation may help to construct a chemical sensor with accurate concentration resolution.

According to the results shown above, the sensing response of vertically aligned CuO nanowire array sensors can be described by Figure 2.12. Before introducing the H_2S, the sensor adsorbed O_2 from air and surface states that allowed electrons generated from the valence band maximum (VBM) were formed and, therefore, induced more hole carriers in VBM, as shown in Figure 2.12(a). At the initial stage when H_2S was introduced, only low concentrated H_2S arrived at the surface of CuO nanowires and the H_2S reacted with the oxygen adsorbates:

$$H_2S + 3O^-(\text{ads.}) \rightarrow H_2S + SO_2 + 3e^-. \tag{2.3}$$

The released electrons from the surface states recombine with the holes in VBM and resulted in reduced conductivity (Figure 2.12(b)). Most importantly, this process can be recovered if pure air was introduced. However, when high concentrated H_2S reached the nanowire surface, a reaction began and a layer of CuS was formed, covering the surface of CuO nanowires and changing the effective contact area between the adjacent nanowires, as shown in Figure 2.12(c). This reaction was difficult to recover. The sensing responses to H_2, CO, and NH_3 were also studied at room temperature and elevated temperature (160 $^\circ$C). The sesnor showed no response to H_2 and CO, even with concentration as high as 2%. Small responses to highly concentrated ($>$1000 ppm) NH_3 were observed (Figure 2.13). The relative inert properties to these gases can be ascribed to the good selectivity of the CuO nanowires to H_2S.

2.2.4 Summary

In summary, a chemical sensor based on vertically aligned CuO nanowire array was constructed by in situ SEM micro- manipulation. The H_2S sensing properties have been investigated systematically. The sensor showed a detection limit as low as 500 ppb. Different sensing mechanisms were employed to explain the detection at low and high concentration. When the sensors were exposed to H_2S with a concentration higher than 5 ppm, the surface reaction began and thus a layer of CuS
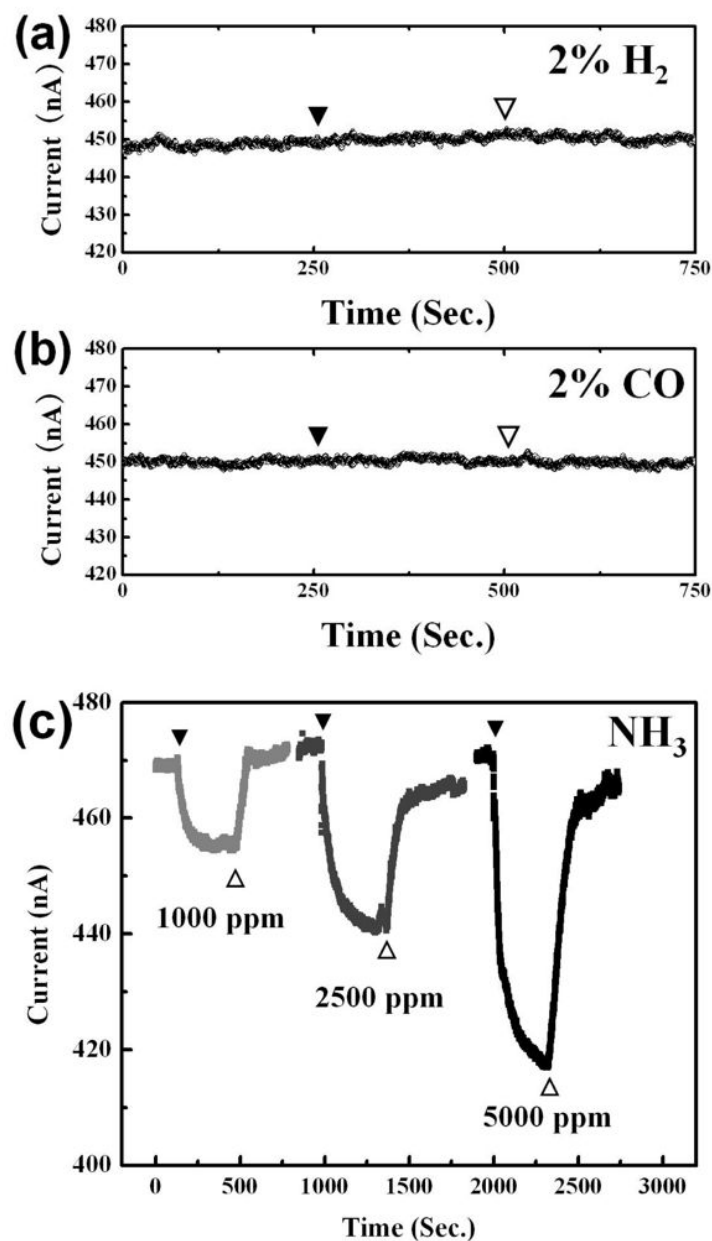
Figure 2.13: Sensing responses of CuO nanowire array device to air diluted H_2, CO, and NH_3. The time when gases were inlet is indicated by solid triangles and the time when the gases were pumped out is indicated by hollow triangles. [121]

formed, which increased the effective contact area between the adjacent nanowires, resulting in increased conductivity. In addition, the sensor showed a good selectivity to H_2S compared with the responses of H_2, CO, and NH_3.

Chapter 3

Electronic Noses Based on Multiple Nanowire Arrays

Conventional "lock-and-key" approach to selective detection of gas molecules applied strict requirements on the fabrication of metal oxide gas sensors. The standalone gas sensors must have high response to specific gas and be inert to other interferences. This requirement is actually very hard to realize. For examples, it is very difficult to design a gas sensor that can discriminate two active gases with similar properties. Mimicking biological olfactory systems that use broad chemical diversity of the array of olfactory receptors have superior power on gas discrimination [127]. In this section, the feasibility of using multiple nanowire array gas sensors to form electronic nose systems will be explored.

3.1 General Route to the Growth of Metal Oxide Nanowire Arrays

The limited availability of 3D metal oxide nanowire arrays is the major obstacle to realize the electronic nose systems. Not all the metal oxides can be grown as well patterned nanowire arrays. For examples, many high performance gas sensing metal oxides (i.e. SnO_2, WO_3, In_2O_3, MoO_3) are still difficult to be grown as nanowire arrays. The selective detection and construction of electronic noses require a material library that has versatile material selections.

Among all the metal oxide nanowires, ZnO nanowire is one of the most explored materials in last decade due to its multifunctional properties that can be applied for many areas [128]. The growth technique for ZnO nanowire array is relatively mature and low-cost wafer-scale growth
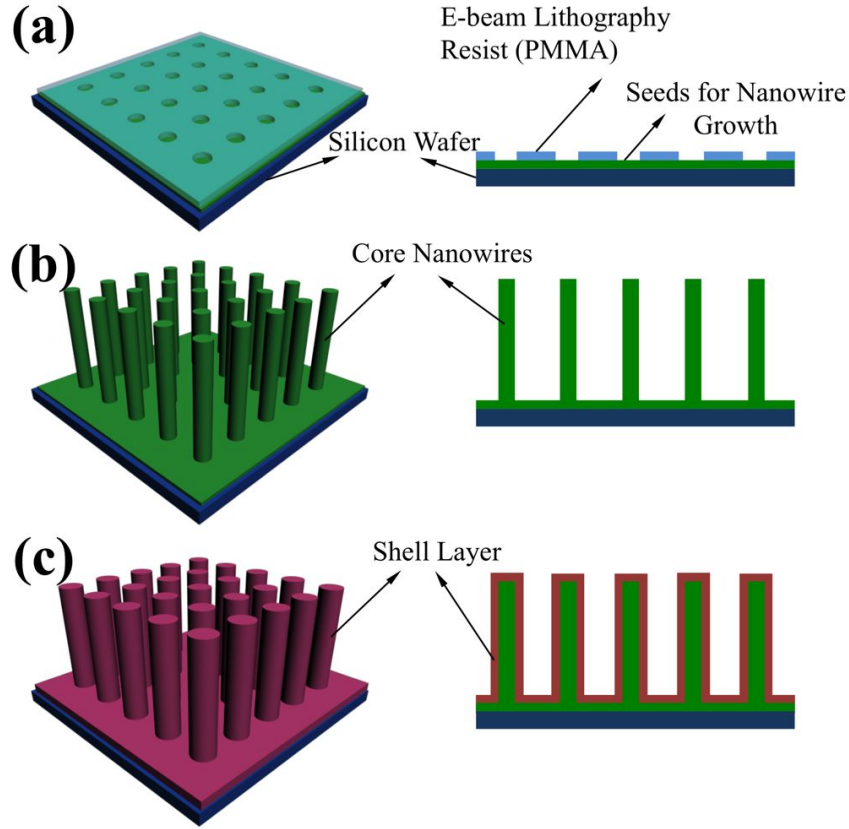
Figure 3.1: A general route to prepare various metal oxide nanowire arrays by using ZnO nanowires as templates.

of well-aligned ZnO nanowire has be reported [129–135]. To prepare the well-aligned nanowire array of gas sensing metal oxides, we propose a general route for polycrystalline nanowire fabrication using high-quality ZnO nanowire arrays as structural templates. Figure 3.1 shows the basic procedures in this process. The process starts with a substrate with textured seed-layer and PMMA patterns [Figure 3.1(a)]. The well-aligned ZnO nanowire array is grown by hydrothermal methods, shown in Figure 3.1(b). Finally, a layer of gas sensing metal oxide materials is coated on the surface of nanowire array, which can be realized by various thin film techniques. It is important to point out that the inter-nanowire space and alignment is critical for the homogeneous coating, which is controlled by the e-beam lithography and textured seeds in the first step. And sputtering is preferred for shell layer coatings because the argon gas used in the processing can promote the

diffusion of deposition species and increase the homogeneity of the surface coatings. Additionally, ZnO has large lattice mismatch to other metal oxide materials, which induces Volmer-Weber(VW) growth on ZnO surface forming polycrystalline coatings. The grain boundaries in the polycrystalline coatings may further increase the sensing performance of the nanowires.

The effectiveness of this template method will first be evaluated by lateral single nanowire gas sensors. Electronic noses that consist of different metal oxide coatings or noble metal decorations were then created and their sensitivity and capability of gas discrimination were also addressed.

3.2 Effectiveness of Template Growth of Metal Oxide Nanowire for Gas Sensing[1]

The sensing responses of 3D nanowire array are the synergic effect of the conductivity change in individual nanowires with parallel connections. The study of sensing performance in lateral patterned single-nanowire sensors is a very important method to evaluate the nanowires' sensing properties. In this section, ZnO nanowire arrays were first grown with chemical vapor deposition (CVD) and sequentially coated with gas sensing metal oxides and noble metal catalytic particles by conventional thin film techniques. The detailed structures of the coated nanowire were first investigated. The nanowires with and without coatings were patterned into two-terminal single-nanowire devices. The fundamental electrical and gas sensing properties of these devices were measured. The results of this research provide important indications of the effectiveness of the general route for the growth of metal oxide nanowire arrays.

3.2.1 Preparation of Pd/SnO_2-coated ZnO Nanowires

The ZnO nanowires were prepared by thermal evaporation via vapor-liquid-solid (VLS) mechanism originally developed by Wagner and Ellis [98]. An *a*-plane sapphire single crystalline sub-

---

[1]Adapted in part by permission from J. Chen *et al.* IEEE Tran. Nanotech. 9(2010)634. Please check Appendix D. © Copyright [2010] IEEE. http://dx.doi.org/10.1109/tnano.2010.2052629
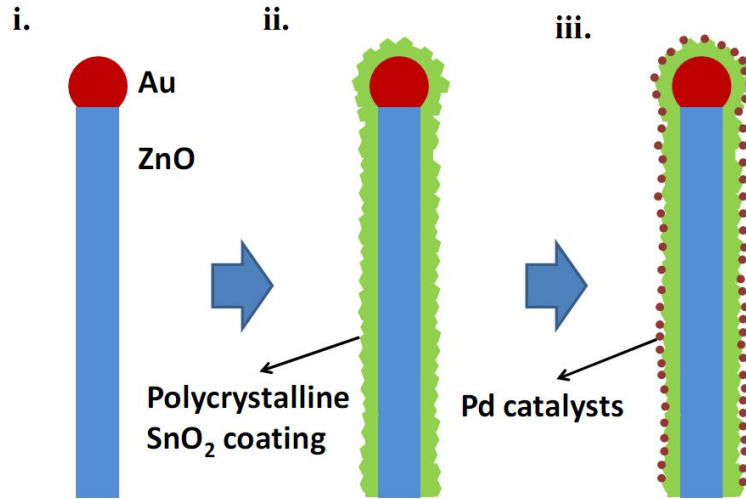
Figure 3.2: Schematic diagrams of nanowire cross-sections showing the growth processes of polycrystalline Pd/SnO_2 nanowire using a ZnO nanowire template: (i) VLS growth of pristine ZnO nanowire; (ii) PLD deposition of a polycrystalline layer of SnO_2; (iii) Sputtering coating of Pd catalysts. [136]

strate was first cleaned and coated by a 3-nm gold layer with sputtering. In the thermal evaporation process, 1 g ZnO (Alfa Aesar, CAS# 131413-2) and graphite powder (Alfa Ae- sar, CAS# 231955-3) mixture (mass ratio 1:1) worked as the source materials and was heated to 1000 °C through the whole growth process. The processing gas was a mixture of 100 sccm Argon and 10 sccm Oxygen, which carried the reduced Zn vapor from the source material to downstream low temperature area (800 °C) where the sapphire wafer was located. The sputtered gold layer melted and agglomerated into nanoparticles under the high growth temperature. The gold nanoparticles worked as the catalysts in the VLS growth and determined the diameter of the ZnO nanowires [98]. The as-grown ZnO nanowires were then loaded in a PLD system for SnO_2 nanocrystal coating. The background Argon pressure was maintained relatively high (10 torr) to promote the diffusion transport of deposition species, ensuring a homogeneous SnO_2 coating. A layer of 5 nm SnO_2 was coated at a temperature of 400 °C. Finally, the nanowires were loaded into a DC-sputtering system. A layer of Pd particles (0.2 nm normalized thickness) was sputtered onto the nanowire surfaces. The schematic diagrams of these processes are shown in Figure 3.2. All the as-synthesized nanowires were first

characterized by a Carl Zeiss 1530 VP field emission scanning electron microscope (FESEM) and a JEOL 2010 conventional transmission electron microscope (TEM). The initial composition analyses were conducted by the energy dispersive X-ray spectroscopy (EDS) equipped on the FESEM and TEM. Detailed structural characterization of Pd nanoparticle coatings was achieved by high-angle annual dark-field (HAADF) scanning TEM (STEM) by a JEM-2100 F-field emission TEM with CEOS C_S-corrector and the HAADF detection angle was $73 \sim 194$ mrad.
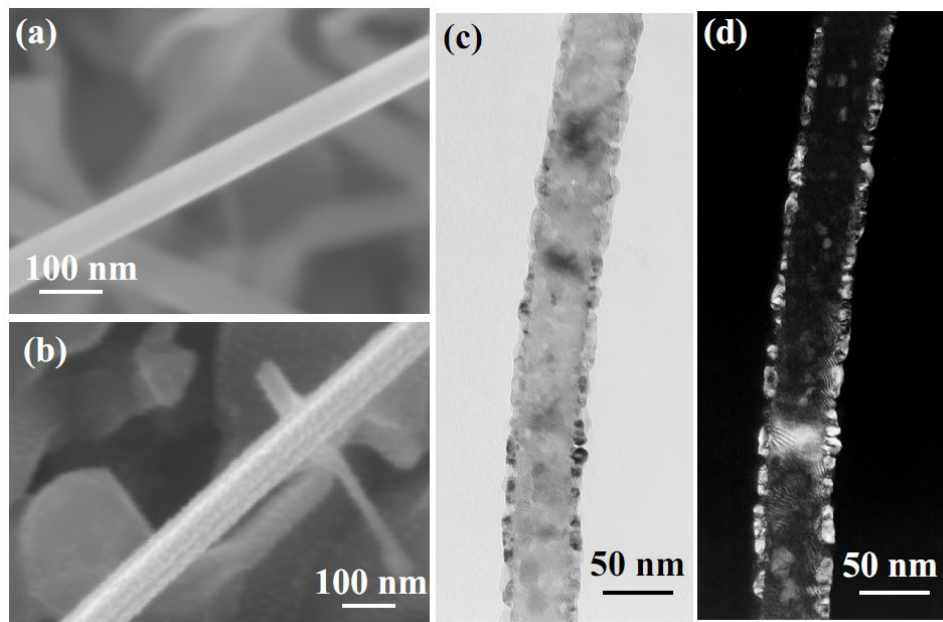
Figure 3.3: (a) and (b) FESEM images of a ZnO nanowire and a Pd/SnO$_2$ nanocrystal coated ZnO nanowire. (c) and (d) Conventional bright field and dark field images of a Pd/SnO$_2$ coated ZnO nanowire. [136]

VLS process is the most successful and controllable method for the growth of high-quality single crystalline ZnO nanowires. Figure 3.3(a) shows the FESEM image of a ZnO nanowire with a diameter of about 80 nm. The lengths of the nanowires are about 20 μm. The pristine ZnO nanowires show smooth surfaces without any undulations. The surface roughness increased after the SnO$_2$ and Pd nanocrystal coatings, shown in Figure 3.3(b). Figure 3.3(c) and (d) are low-magnification bright field and dark field images taken by a JEOL 2010 conventional TEM. The coated SnO$_2$ nanocrystals were highlighted in the dark-field image. The thickness of SnO$_2$

coating is about ~ 4 nm with polycrystalline structure. Though the SnO_2 nanocrystals formed a continuous film on the ZnO-nanowire surface, no specific epitaxial relation was found. Due to the different crystal structure and large lattice mismatch that induces high lattice stress, the SnO_2 was grown with Volmer-Weber mode on the ZnO surfaces [137]. Unlike many applications that require epitaxial growth to reduce density of grain boundaries (GB) to avoid carriers scattering [138,139], the large amount of GB in these nanowires is beneficial for gas-sensing properties since the energy barriers formed at the GB are very sensitive to the surface reaction and may result in significant change of device conductivity. Detailed structural and compositional characterizations are needed to evaluate the Pd coating.

Figure 3.4(a) is a high-resolution TEM (HRTEM) image enlarged from the edge of a Pd/SnO_2 nanocrystals-coated ZnO nanowire. The core ZnO nanowire was identified as single crystalline wurtzite structure with growth direction along [0001] by using electron diffraction, while SnO_2 was identified as a rutile structure. A HAADF Z-contrast image was obtained under a C_S-corrected TEM to characterize the distribution of Pd-nanocrystal coating, as shown in Figure 3.4(b). Because Pd has much larger atomic mass than other elements (Zn, Sn, and O) in the nanowires, the Pd nanocrystals can be highlighted by the contrast difference. The Pd nanocrystals have an average diameter of about 2 nm with an interparticle distance of 2 nm. The interspaces of Pd nanocrystals that allow targeting species to reach SnO_2 layer and avoid current paths through the Pd layer are extremely critical for the sensing performance and require well-controlled deposition process. The inset of Figure 3.4(b) gives a high-resolution HAADF image of a single Pd nanocrystal sitting on the nanowire surface. The Pd nanocrystal has irregular surface facets, which contribute to the high-catalytical activity [140]. A nanoprobe EDS linescan is depicted in Figure 3.4(c) to confirm the element distributions and the EDS spectra at three typical spots are also given in Figure 3.4(d). From the nanoprobe linescan, it can be confirmed that the SnO_2 nanocrystals are coated on the surface of ZnO nanowire and the Pd nanocrystals were deposited on the outermost layer of the nanowire.
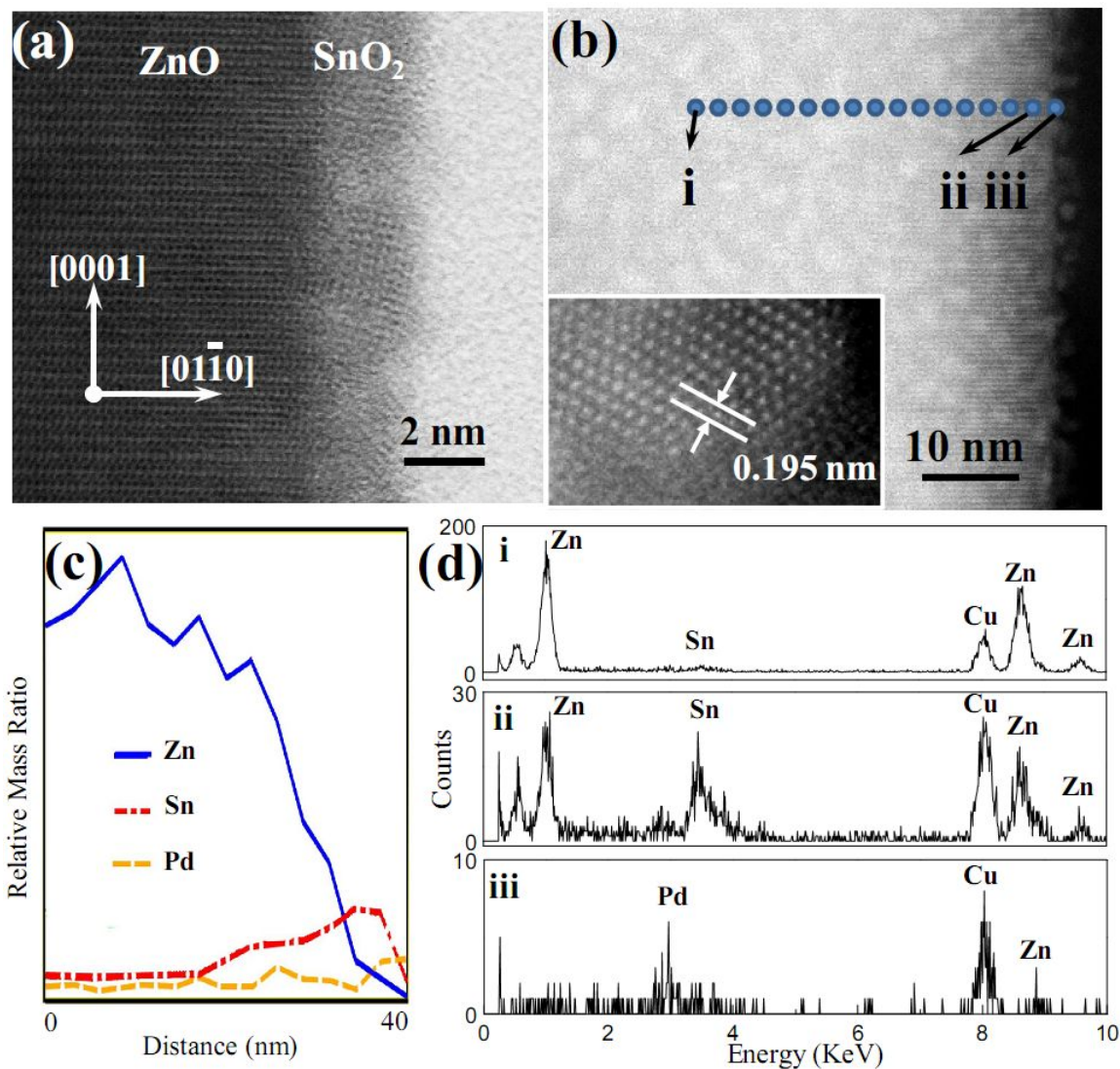
Figure 3.4: (a) A high resolution TEM image showing the ZnO nanowire with polycrystalline SnO$_2$ and Pd nanocrystal coating. (b) A HAADF Z-contrast image taken under a C_S-corrected field emission TEM highlighting the Pd nanocrystal distribution. The inset shows the lattice image of a Pd nanocrystal taken by HAADF STEM through [110] zone. (c) Composition distribution obtained by nanoprobe EDS linescan across the nanowire. The sampling points are indicated in Figure (b). (d) Three EDS spectra obtained at the ZnO core (i), SnO$_2$ layer (ii), and outmost Pd coating (iii). [136]

3.2.2 Sensing Performance of Single-Nanowire Devices
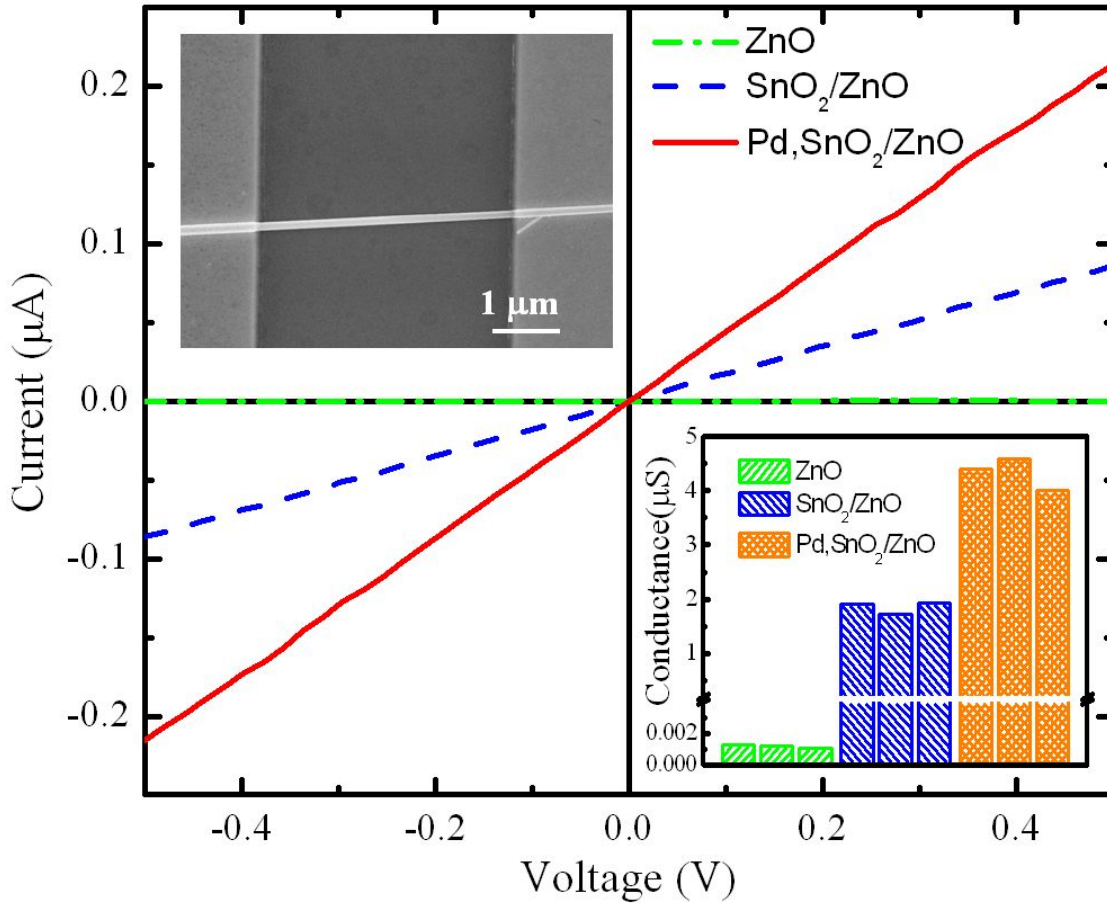
Figure 3.5: *I-V* characteristics of three types of nanowires. The inset FESEM image shows a typical device structure. The inset bar-graph depicts conductance of 9 devices with different surface coatings. [136]

The nanowires (pure ZnO, SnO_2-coated ZnO, and Pd/SnO_2-coated ZnO) were dispersed into ethanol by ultrasonication and then deposited onto Si/SiO_2 (600 nm) substrates with photolithographically defined electrodes. E-beam nanolithography process was used to make Au(100 nm)/Cr(10 nm) nanopads to connect the nanowires to the predefined electrodes. The basic *I-V* characteristics of these devices were measured by Keithley 2400 source meter. The devices were also loaded to a variable-temperature sensor testing cell for gas-sensing measure-

ment by successively introducing air-diluted H_2S gases with different concentrations. Before all the measurements, the devices were stabilized at 160 °C for 5 h.

Pristine ZnO, SnO_2-coated ZnO, and Pd/SnO_2-coated ZnO nanowires were then patterned into two-terminal resistors as shown in the inset FESEM of Figure 3.5. The nanowire spans of all the devices were kept to 5 μm. The *I-V* characteristics were measured by Keithley 2400 sourcemeter, plotted in Figure 3.5. All *I-V* measurements are linear implying good ohmic contacts between nanowires and metal patterns. It is important to point out that the Pd-nanocrystal coating did not have obvious effect on the contact nature even though Pd possesses large work-function value. This can be ascribed to the discrete distribution of Pd nanocrystals and similar work function with SnO_2. From the inset bar graph of Figure 3.5, it was found that the device resistance changed dramatically before and after the coating of the SnO_2 layers. The resistance of ZnO nanowires is almost three orders higher than the SnO_2-coated ZnO nanowire, implying that the ZnO nanowire works as a structural support for SnO_2 nanocrystals other than the current-transport channel and major part of current was transported through the SnO_2 layer. The high resistance of ZnO is caused by the oxygen-abundant growth process that induced low concentration of oxygen vacancies and, thus, low carrier density. The coating of Pd nanocrystals is nearly double the conductance of the nanowires. The increment of conductivity may be explained by the fact that Pd nanocrystals can bridge adjacent SnO_2 nanocrystals and reduce the contact resistances.

The three types of nanosensors were loaded to gas sensor testing cell for sensing response measurement separately. All the measurements were conducted at 160 °C. Figure 3.6(a) plots the normalized conductance changes $(G_S - G_0)/G_0$ of pristine ZnO device and SnO_2-coated ZnO when air-diluted H_2S with different concentrations were successively introduced. The pristine ZnO-nanowire device shows no response to even 5000 parts per million (ppm) H_2S. The inertness of ZnO device to highly concentrated H_2S may be attributed to the low concentration of carriers in nanowires. After applying the SnO_2 coating, the devices can detect 100 ppm H_2S. And the conductance of sensor can be gradually recovered when introducing pure synthetic air to the testing
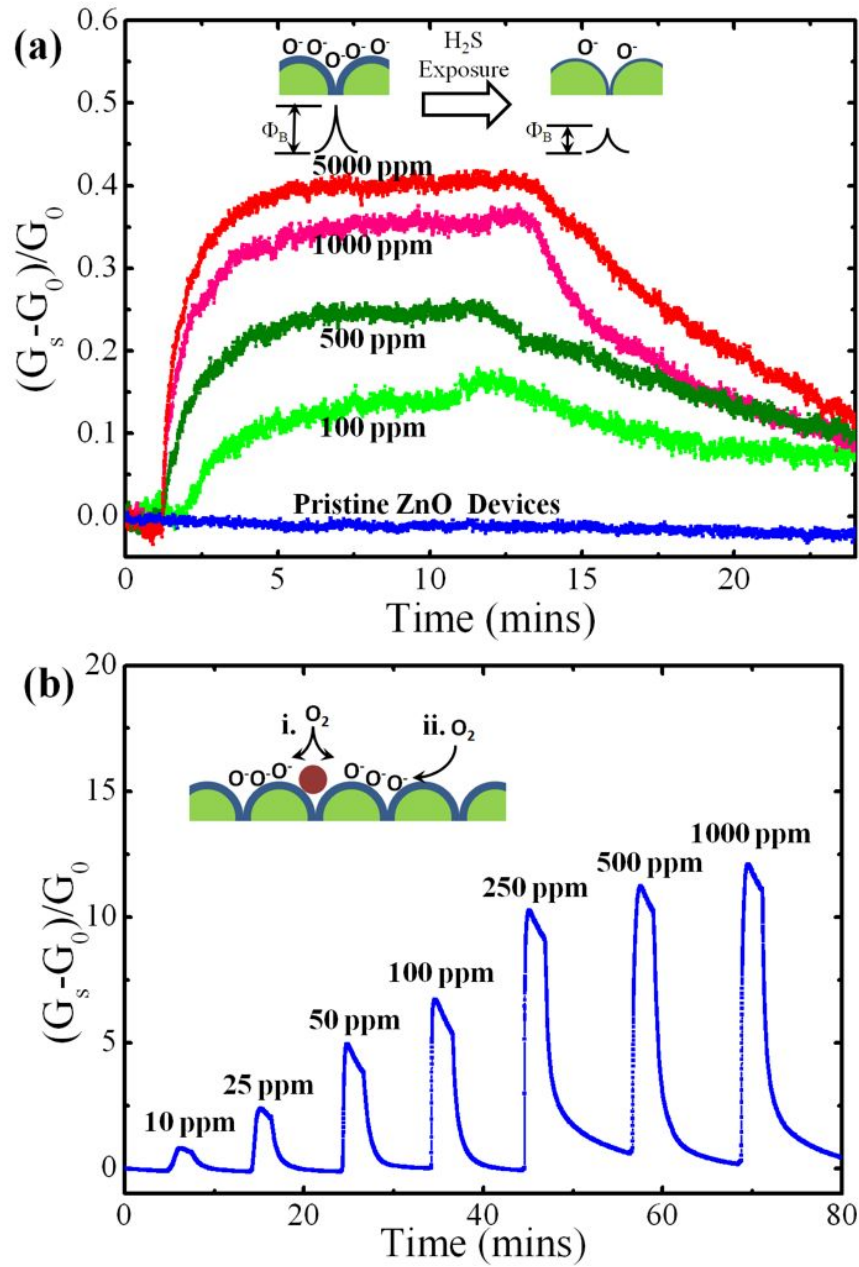
Figure 3.6: (a) Normalized conductance change for pristine ZnO nanowire device and SnO$_2$ coated ZnO nanowire device as air-diluted H$_2$S gases with different concentrations were introduced. The pristine ZnO nanowire device showed no response to H$_2$S gas. The inset schematic diagram shows the sensing mechanism of polycrystalline SnO$_2$ film. (b) Sensing response of Pd/SnO$_2$ coated ZnO nanowire devices. The inset diagram depicts the "spillover effect" and "back-spillover effect". [136]

cell. A schematic diagram of the sensing process is depicted in the inset of Figure 3.6(a). The introduced H_2S gas molecules reacted with the adsorbed oxygen species (i.e., O^-, O^{2-}, O_2^-, etc.) [9] and released electrons back to the n-type SnO_2 nanocrystals, as given by

$$H_2S + 3O^- (\text{ads.}) \rightarrow H_2S + SO_2 + 3e^-. \tag{3.1}$$
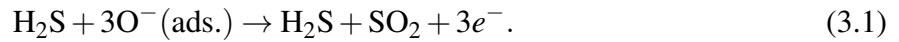
Releasing surface-trapped electrons back to the SnO_2 bulk can effectively reduce the width of depletion layers formed by the adsorbed oxygen and, thus, reduce the height of the energy barriers. The devices conductance increased as the height of energy barriers was reduced. With introducing higher concentration of H_2S, more pronounced conductance increase was observed. Based on the I-V measurements and the sensing responses, it was found that polycrystalline SnO_2 coating played a major role in H_2S detection and the core ZnO nanowire mainly worked as the support for the 1-D nanostructures. The response curves of Pd/SnO_2-coated ZnO-nanowire device is given in Figure 3.6(b), showing that the Pd-nanocrystal coating had promoted the sensitivity of the sensors enormously and the response speeds were also significantly increased. The effect of Pd-nanocrystal coating is generally understood by the "spillover effect" and "back-spillover effect" [52, 141]. For a spillover effect, the oxygen molecule dropped onto the Pd nanocrystals at which the oxygen molecules are catalytically dissociated into atomic species and diffuse to the SnO_2 surfaces. And on the other hand, the oxygen molecules are not necessarily to deposit directly onto the Pd catalysts in a "back-spillover effect". The oxygen molecules can reach to the SnO_2 surface first and diffuse to the Pd catalysts. Compare the interspaces ($\sim$2 nm) of Pd nanocrystals to reported experimental values of spillover zone ($\sim$10 nm) [142], all the exposed SnO_2 surfaces in our devices should be considered as spillover zone. The dissociated oxygen atomic species are highly active and is capable of populating the vacancies on SnO_2 surfaces to work as the electron trapping centers or reacting with H_2S molecules much more effectively. The plots of normalized sensing response (S) in terms of H_2S concentrations (C) are given in Figure 3.7 for the SnO_2-coated ZnO device and Pd/SnO_2-coated ZnO device. The data points can be well fitted by the equation based on
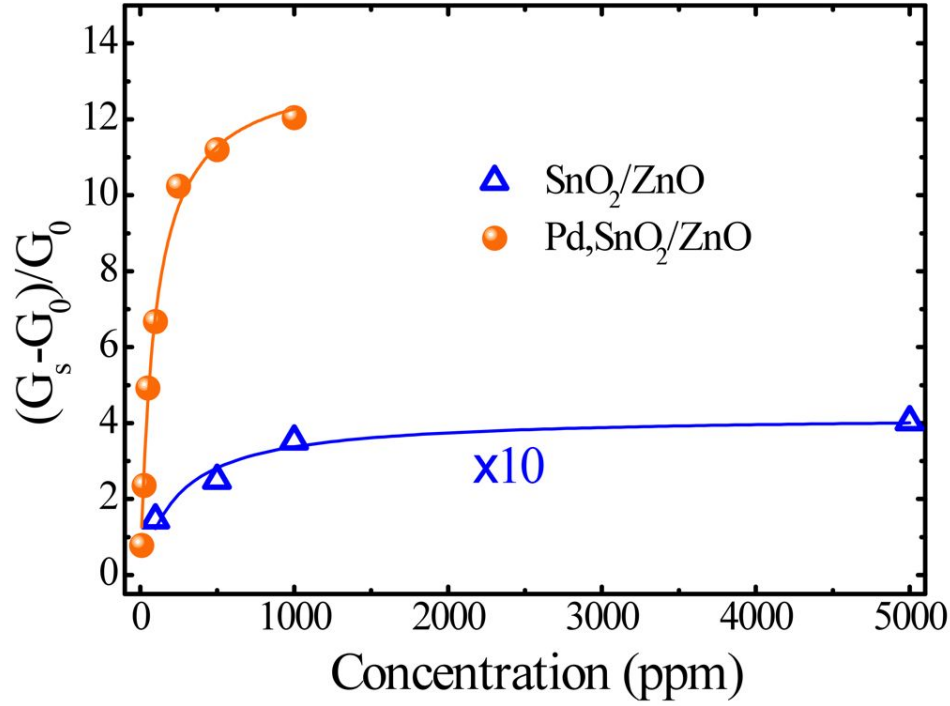
Figure 3.7: Normalized sensitivity ($\Delta G/G_0$) vs. concentration plots for nanocrystal coated nanowires. The solid-lines are the theoretical fitting based on Langmuir isotherm adsorption. The result for SnO_2 coated ZnO nanowire is multiplied by 10 for clear comparison. [136]

Langmuir isotherm adsorption [75, 143], written as

$$S = \frac{a}{1 + (b/C)}, \qquad (3.2)$$

where S is the sensitivity ($\Delta G/G_0$), C is the gas concentration, and a and b are fitting constants. The fitting constants are $a = 0.4199$, $b = 244.0$, and $a = 13.46$, $b = 96.50$ for the SnO_2-coated ZnO device and Pd/SnO_2-coated ZnO device, respectively. The curve shifts from high concentration to low concentration after the Pd coating, indicating much less H_2S molecules are needed to consume the adsorbed oxygen species on SnO_2 surfaces. This also proves the strong catalytic behavior of Pd nanocrystals. In addition, 1-nm-thick Pd layer was also sputtered on the SnO_2-coated ZnO nanowire, which formed a continuous Pd film on the nanowire surface and short the whole device with a resistance as low as 2 kΩ. The device showed no response to H_2S. Therefore, the

distribution of Pd-nanocrystal coating is crucial to the sensing responses. The device performance may be further improved in terms of the Pd nanocrystals size and interparticle distances, which requires further study.

To evaluate the specificity of the nanowire device, the responses to air-diluted CO and NH_3 have also been measured. The Pd/SnO_2-coated ZnO device showed no response 2 to 2000 ppm CO at 160 °C and the response to 2000 ppm NH_3 was only one fiftieth of the response for 1000 ppm H_2S indicating good specificity of the sensing device.

3.2.3   Summary

Polycrystalline Pd/SnO_2 nanowires have been successfully prepared using ZnO-nanowire templates by combination of thermal evaporation, PLD, and DC sputtering. The polycrystalline nanowires were patterned as two-terminal gas sensors. In this device structure, the ZnO nanowire worked as a structural backbone to support the Pd/SnO_2 -nanocrystal film. The SnO_2 polycrystalline film confined on ZnO nanowire played the major role of the sensing properties and the discrete Pd nanocrystals catalytically dissociate the gas molecules into active atomic species for enhanced sensitivity. Due to the natures of the synthesis methods (thermal evaporation, PLD, and dc sputtering), the fabrication strategy for 1-D nanosensors can be readily applied to other gas-sensing material systems (i.e., WO_3 , MoO_3 , etc.).

3.3 Gas Discrimination by Electronic Noses Based on Multiple Nanowire Arrays

In this section, two routes to electronic nose systems by 3D metal oxide nanowire arrays will be introduced, both of which use ZnO nanowire arrays as structural templates. Firstly, ZnO nanowire arrays coated with gas sensing metal oxides were used as the basic elements forming a two-device system that can discriminate H_2S and NO_2; secondly, different catalytic metals were applied to
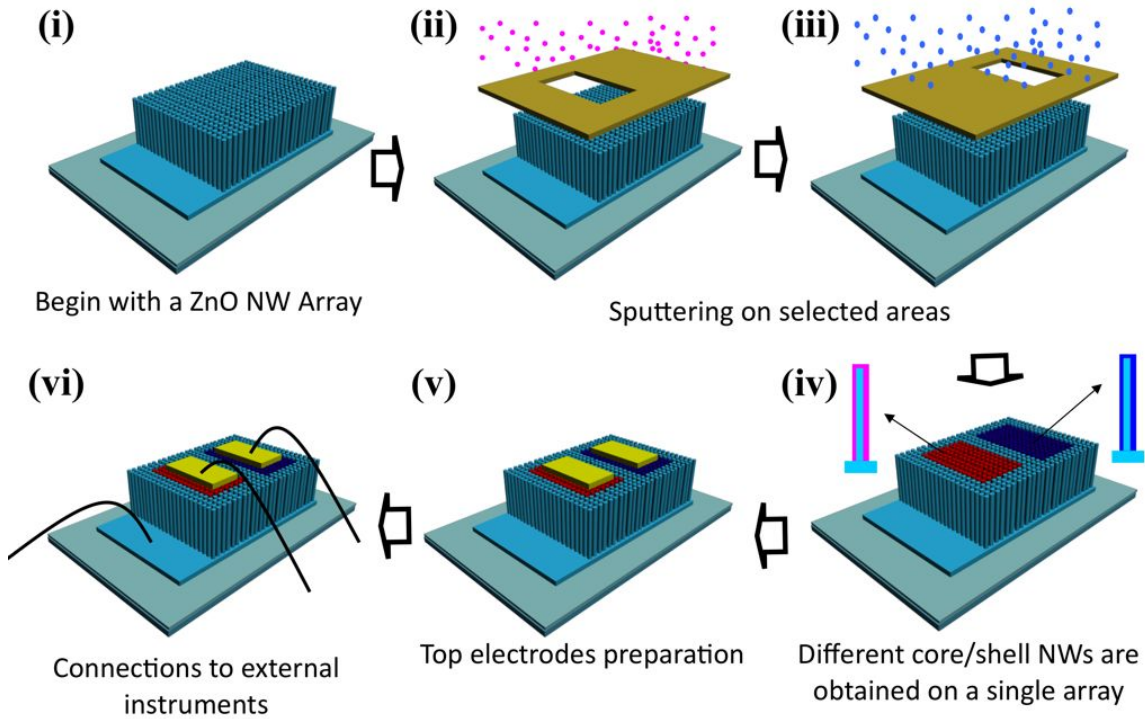
Figure 3.8: Schematic diagrams showing the procedures of metal oxide coatings on ZnO nanowire arrays for selective detection. (i) The procedures start with well-aligned ZnO nanowire arrays; (ii) $\sim$ (iv) selected-area metal oxide coatings; (v) and (vi) preparation of top electrodes on nanowire arrays.

modified the sensitivity of SnO_2 coated ZnO nanowire arrays forming a electronic noses for gas discrimination toward five different gases (NO_2, H_2S, NH_3, CO and H_2).

3.3.1 Electronic Nose Prepared by Nanowire Arrays with Different Metal Oxide Coatings

3.3.1.1 Fabrication of ZnO Nanowire Arrays with SnO_2 and CuO Coatings

The fabrication of ZnO nanowire arrays coated by gas sensing metal oxides is generally started with well-aligned ZnO nanowires grown by hydrothermal method. The orientation and growth position of nanowires can be finely controlled by highly-textured seeds and ebeam-patterned PMMA layer. In a typical hydrothermal growth process, the silicon wafer with 600 nm thermal oxidized
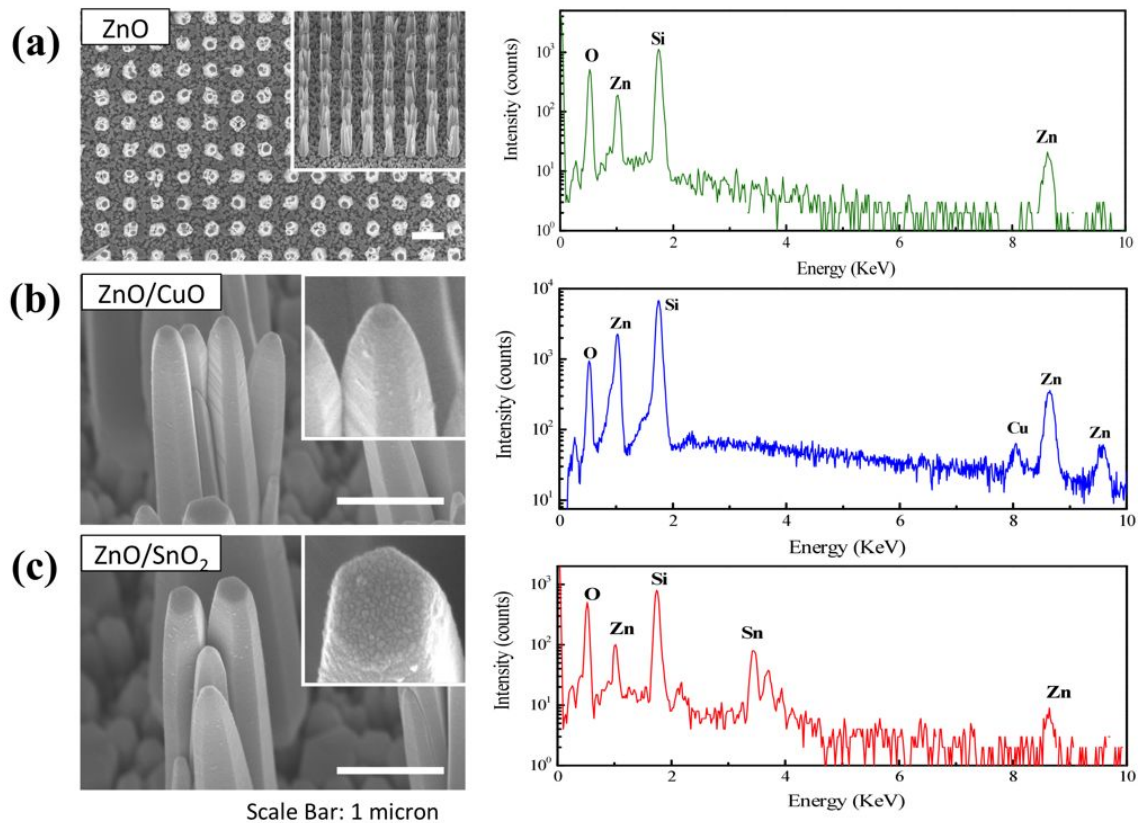
Figure 3.9: SEM images and EDS analyses on ZnO nanowire arrays with or without metal oxide coatings. (a) Pure ZnO nanowire arrays; (b) CuO coated ZnO nanowire arrays; (c) SnO_2 coated ZnO nanowire arrays.

layer was coated with 50 nm ZnO thin film by sputtering. The ZnO coated silicon wafer was then transferred to autoclave for hydrothermal growth of the highly textured seeds. The nutrition solution was the water solution of 25 mM mixture of $Zn(NO_3)_2$ and hexamethylenetetramine (HMTA) with 1:1 mass ratio. The seeds were grown at 90 °C for 120 mins. After the seed layer growth, the wafer was rinsed by de-ionized water and spin-coated by PMMA (950A4, Microchem Inc. 3000 rpm, 1 min). EBL process generated square or hexagonal patterns on the PMMA layer where the ZnO nanowire grew out. A slight oxygen plasma cleaning (30 W, 30 seconds) was used to improve the wetting of nutrition solution on the PMMA layer. Secondary hydrothermal growth was conducted after the EBL process with a 5 mM nutrition solution for 24 hours. The as-grown ZnO nanowire arrays were characterized under electron microscopes to ensure the quality before
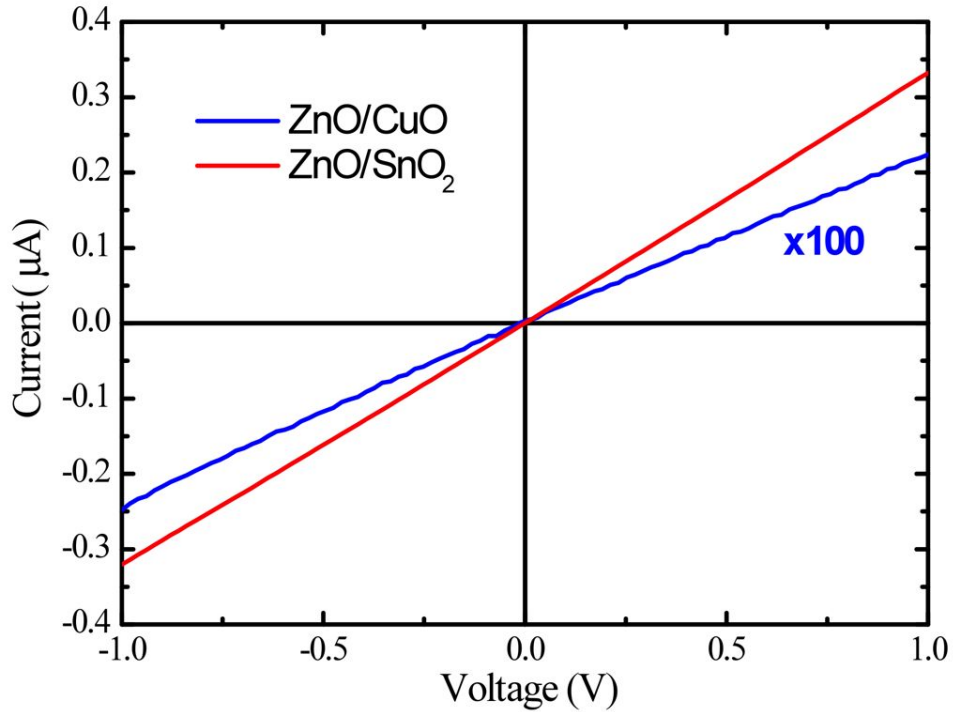
Figure 3.10: *I-V* Characteristics of CuO coated ZnO nanowire array and SnO$_2$ coated ZnO nanowire array. CuO coated ZnO nanowire array has much higher resistance than SnO$_2$ coated array. The linear characteristics indicated the contacts on the electrodes are Ohmic.

the coating processes. As shown in Figure 3.8, the hydrothermal grown ZnO nanowires were supported by a layer of highly-textured seeds. Common thin film techniques, such as sputtering, PLD, or CVD, can be used to deposit the surface coatings. In this experiment, sputtering of 50 nm SnO$_2$ or CuO was carried out in a Lekser PVD75 system. The deposition area was selected by metal masks as shown in processes (ii) $\sim$ (iv) in Figure 3.8. Finally the top electrodes to connect the nanowire arrays were prepared by the microfabrication processes similar to the method introduced for WO$_3$ devices, depicted in Figure 3.8(v) and (vi).

Figure 3.9 provides the SEM and EDS characterization on the nanowire array before and after the gas sensing metal oxide coatings. Figure 3.9(a) is the FESEM image of as-grown ZnO nanowire array prepared by hydrothermal method combined with EBL technique. It is clearly shown that the growth positions of nanowires are well-defined by the EBL and the nanowires are all vertically grown due to the highly-textured seeds. Figure 3.9(b) shows the nanowire surface after CuO

69
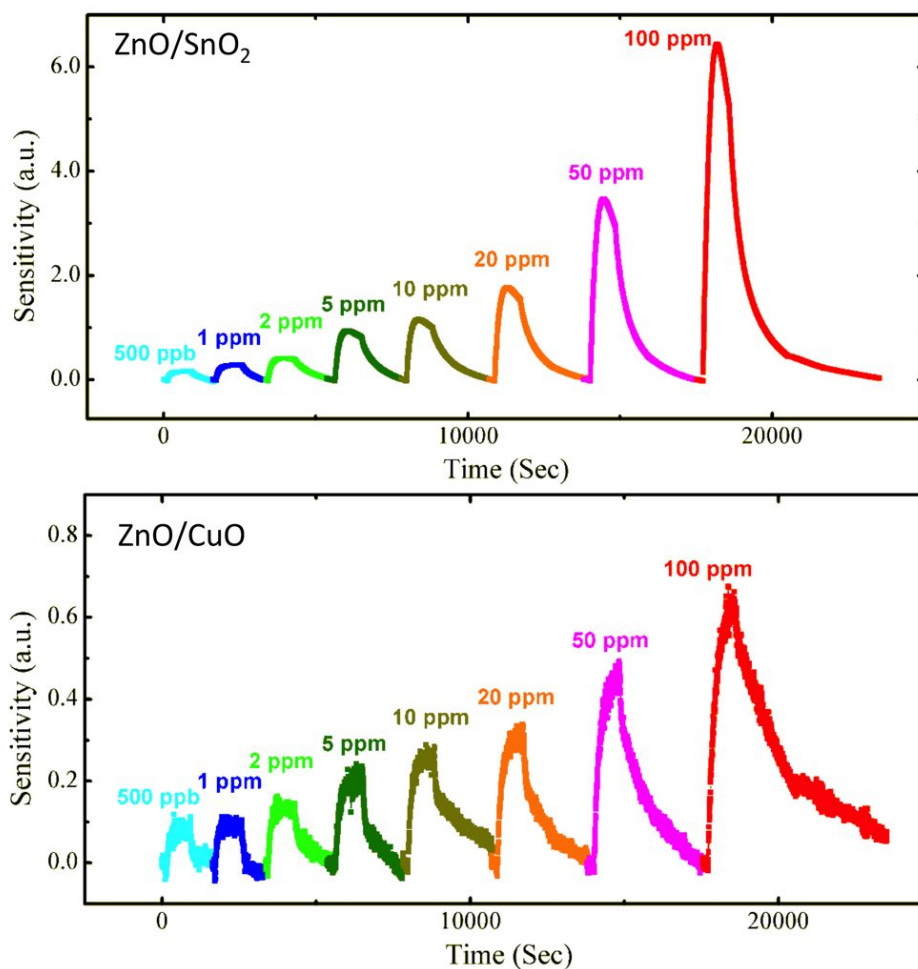
Figure 3.11: The sensing responses of metal oxide coated ZnO nanowire arrays to NO_2 at 160 °C.

coating. The inset FESEM image inidicates the particles formed on the nanowire surface and the EDS also showed the CuO signature on the nanowire. Similarly, the ZnO nanowire array after SnO_2 coating is also given in Figure 3.9(c). The nanowire showed obvious change in surface roughness and EDS further confirmed the successful coating of SnO_2 on the ZnO nanowire surface. Both of the SnO_2 and CuO were grown with the Volmer-Weber mechanism (island growth) due to their large lattice mismatch to ZnO nanowires. After the structural characterization and top electrode preparation the devices are ready for further electrical measurement and sensing tests.

3.3.1.2   Electrical Properties and Sensing Performance of Metal Oxide Coated ZnO Nanowire Arrays

After the microfabrication of top electrodes, the nanowire array sensors were loaded onto the gas sensor testing system (Appendix A). The devices were connected by 0.02 mm gold wire and silver paste. The Keithley 2400 source measurement unit cooperating with 7001 switch module can continuously monitor the conductivity of all the nanowire array devices.

Before the sensing tests, the *I-V* characteristics of both devices (CuO coated ZnO nanowire array and SnO_2 coated ZnO nanowire array) were obtained by source measurement. As shown in Figure 3.10, the *I-V* curves are both linear, indicating Ohmic contacts between the electrodes and the nanowires. However, the SnO_2 coated ZnO device had much higher conductance than that of CuO coated device (more than 2 orders' magnitude). The *I-V* characteristics implied that the SnO_2 shell carried the major part of the current of the whole devices since they formed high conductivity shell layers on the ZnO nanowires, while the ZnO nanowires in CuO coated ZnO devices still transport a significant part of the electrical current due to the high resistance of the CuO shell. This relation has important effects on the detection mechanism and the sensitivity of the 3D nanosensors.

After the basic *I-V* measurement, the resistances/conductances of the sensors were monitored simultaneously when the air-diluted testing gases with serial concentrations were introduced into the testing cells sequentially. For this experiment, the sensing responses were measured at 160 °C. The sensing responses to air-diluted NO_2 were shown in Figure 3.11. For clear comparison, the sensitivity in these plots was defined by the change of resistance ($\Delta R/R_0$). Since ZnO and SnO_2 are both *n*-type semiconductors, the resistances must increase when exposing to oxidizing gases like NO_2. The SnO_2 coated ZnO nanowires showed increase in resistance when exposed to NO_2, whose detection limit was as low as 500 ppb. The change in resistance can be 600 % for detection of 100 ppm NO_2. Surprisingly, the CuO coated ZnO also showed increase in resistance like normal *n*-type semiconductors when the response to oxidizing NO_2 was tested, shown in Figure 3.11. After

71
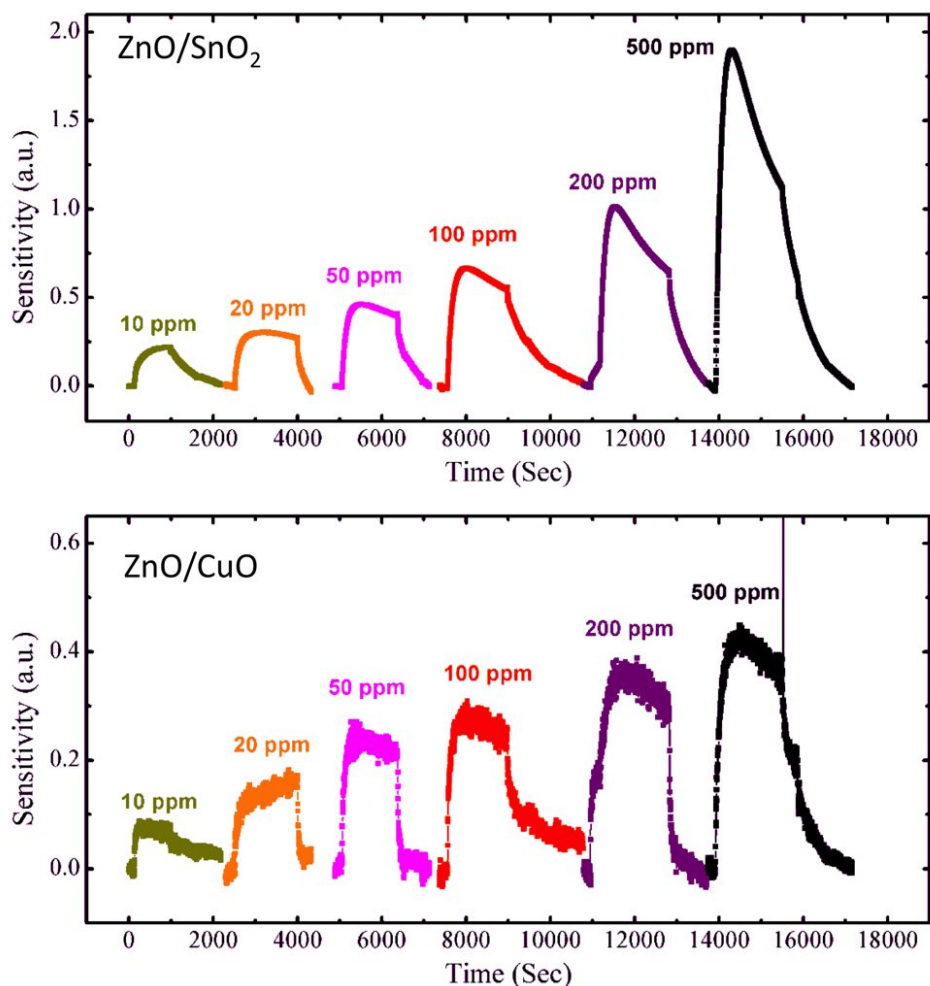
Figure 3.12: The sensing responses of metal oxide coated ZnO nanowire arrays to H_2S at 160 °C.

revisiting the *I-V* characteristics of CuO coated ZnO, it can be explained that the ZnO cores in the core/shell nanowires still contributed to the major part of the sensing response since they also carried the major part of the electrical currents. Though the shell coating was *p*-type CuO, the overall exhibition of the core/shell structures had *n*-type characteristics.

The sensing responses to reducing H_2S are plotted in Figure 3.12, in which the sensitivity is defined by the change in conductivity ($\Delta G/G_0$). The SnO_2 coated devices showed noticeable responses to H_2S with a concentration as low as 10 ppm. The response to 500 ppm air-diluted H_2S was about 200 %. Similar to the responses to the testing for air-diluted NO_2, the CuO coated ZnO nanowire array also showed *n*-type characteristics when exposed to reducing H_2S, in which

72
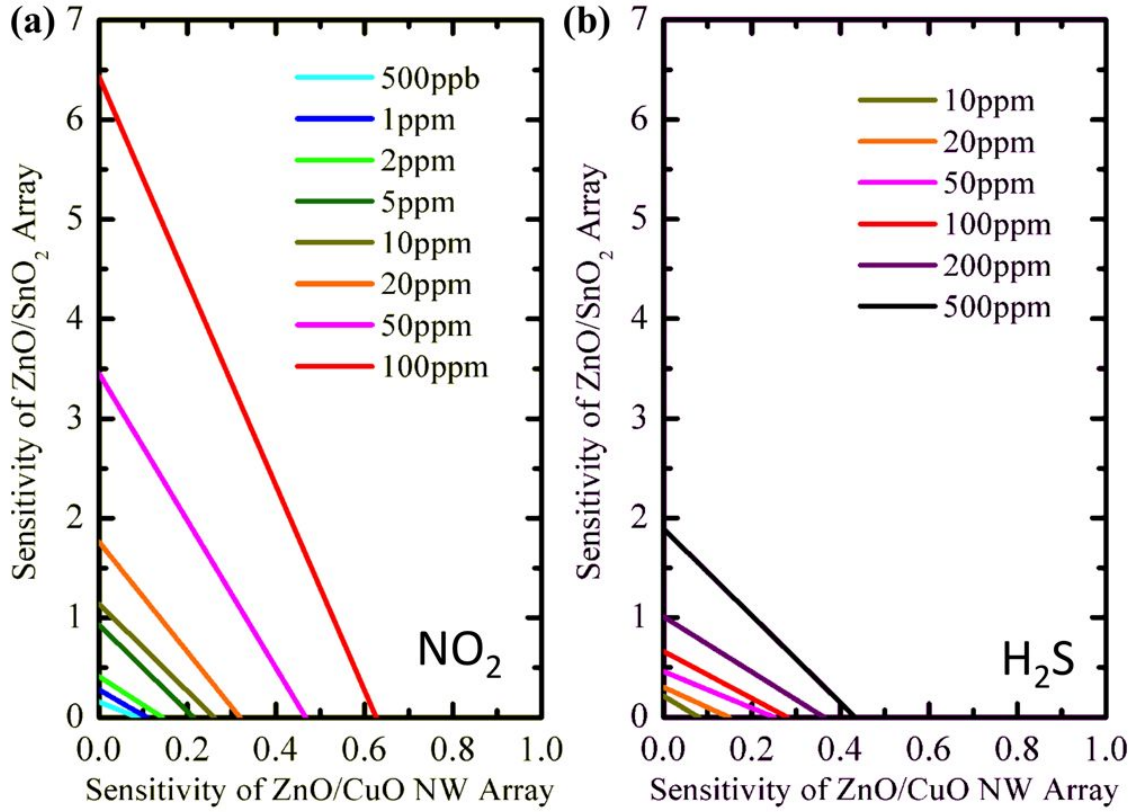
Figure 3.13: Radial plots of sensing reponses to NO_2 and H_2S. Different trianglar shapes indicates the arrays can discriminate these two gases.

increase in conductivity was observed. The CuO coated devices also have much lower sensitivity than that of SnO_2 coated devices. This can be ascribed to the major contribution of sensitivity of ZnO cores. But unlike the sensors introduced in Section 3.2, where the pristine ZnO nanowire device showed no response to H_2S gases, the CuO coated ZnO nanowire array devices had a sensing response of 40 % when exposed to 500 ppm H_2S. The increase in sensitivity toward air-diluted H_2S can be ascribed to two major factors: (1) the increment of depletion layer thickness caused by the *pn* junctions at the *n*-type ZnO and *p*-type CuO interface; (2) the large surface area of 3D nanostructures compared with the single-nanowire devices.

To evaluate the capability of the gas discrimination of these two devices, the radial plots described in the introduction section have been shown in Figure 3.13 based on the sensing responses to the NO_2 and H_2S. The right-angle triangles in radial plots represents the sensing properties

73

to different gases. The ratio between the right-angle sides should be similar when the devices were exposed to same kind of gas even at different concentrations. In the radial plot for NO_2, the SnO_2 coated ZnO device had much stronger responses, which made one right-angle side was much longer than the other. The difference of the right-angle sides for the radial plot of H_2S is much smaller than that for NO_2, which is one of the most important signatures for the discrimination of these two gases. Therefore, the ratio difference in radial plots can be employed to discriminate different gases.

3.3.1.3 Summary

An electronic nose system based on ZnO nanowire arrays with different gas sensing metal oxide coatings has been demonstrated for gas discrimination of NO_2 and H_2S at 160 °C. The SnO_2 coated ZnO sensors showed responses to NO_2 and H_2S with concentration as low as 500 ppb and 10 ppm, respectively. The CuO coated ZnO sensors presented *n*-type properties, which had same response trends as SnO_2 coated devices. The CuO coatings helped to deplete the ZnO nanowires and increased the sensitivity. However, the sensitivities of CuO coated devices were relatively low compared with SnO_2 coated devices. Radial plots for two-device systems were utilized to evaluate the capability of gas discrimination for the electronic nose constructed by these nanowire-array gas sensors.

3.3.2 Electronic Nose Prepared by Different Catalytic Noble Metal Decorations

Catalytic noble metal particles can help to dissociate the gas molecules in ambience into atomic species that have much stronger activities before they reach the surfaces of metal oxide semiconductor. The catalytic metal particles are frequently used as additives or surface modifications to increase the sensitivity of metal oxide gas sensors. In some cases, the improvement in sensitivity can be several orders' magnitudes [52]. Furthermore, different noble metals have distinct catalytic be-

haviors toward different gases, therefore, adding noble metal or modifying the metal oxide surface by noble metal particles can significantly change the selectivity of metal conductometric sensors. Accordingly, the chemical diversity of the nanowire arrays, which is very important for creation of high performance electronic noses, can be increase by using noble metal coatings. In this section, SnO_2 coated ZnO nanowire arrays were used as the platform for highly sensitive and selective gas detection and discrimination, in which the sensitivity of individual nanowire-array sensor was altered by different noble metal coatings (Pt, Pd, and Au).

3.3.2.1 Experimental Section

The growth of ZnO nanowire arrays for gas sensors typically starts with thermal oxidized Si substrates. A 5×5 mm^2 substrate was ultrasonically cleaned by acetone, isopropyl alcohol (IPA), and deionized water. After the cleaning process, the substrate was dried under a nitrogen flow. The cleaned substrate was later loaded into a Cressington 308R thin film coating system for bottom electrode coating. A 10-nm-thick Cr film was first coated by direct current (DC) sputtering at room temperature to ensure adhesion between the amorphous silicon oxide and the gold layer. Subsequently, a 20-nm-thick Au layer was also coated by DC sputtering at room temperature. The substrate with bottom electrode was then coated with 5-nm-thick amorphous ZnO layer at room temperature by radio-frequency (RF) sputtering in a Lesker PVD 75 system. The deposition rate was maintained in the range of $0.2 \sim 0.4$ Angstrom/s. The nutrition solution with 1:1 mass ratio of $Zn(NO_3)_2$ and hexamethylenetetramine (HMTA) was prepared and stirred for 24 hours. The concentrations for textured seed layer and nanowire growth are 25 mmol/L and 5 mmol/L, respectively. Following Xu's report [134], the substrate was flipped-down and floated on the nutrition solution to avoid precipitate deposition and overgrowth. The seed layer was grown at 90 °C for 2 hours. The substrate was then cleaned by IPA and de-ionized water, and finally blew dry by nitrogen flow. Before the e-beam lithography process (EBL), a layer of Poly(methyl methacrylate) (PMMA) (Microchem, 950A4) was spin-coated at 3000 rpm and post-heated at 150 °C for 90 sec-
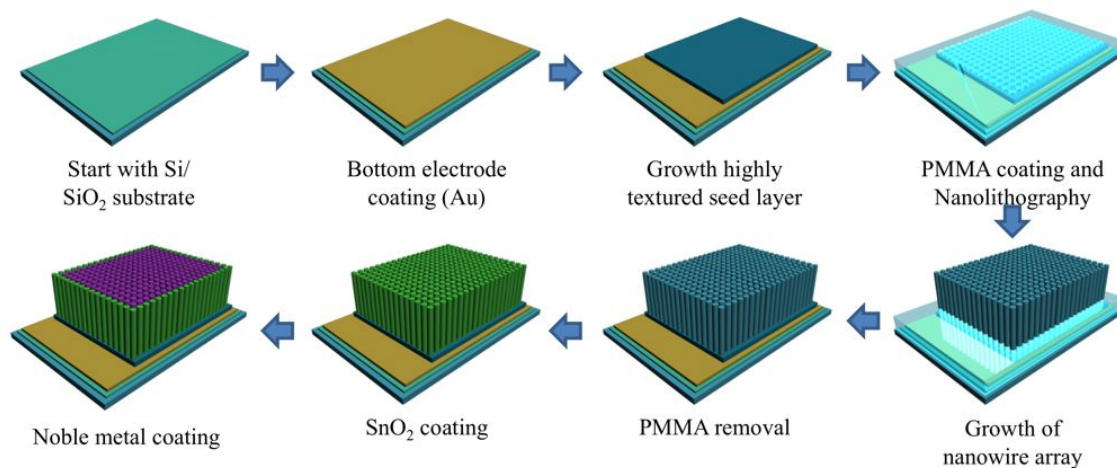
Figure 3.14: Schematics showing the process of preparation of noble metal modified SnO_2 coated ZnO nanowire arrays.

onds. The patterns were exposed by 10kV electron beam in a Carl Zeiss 1530 VP field emission electron microscope (FESEM), and the scanning was controlled by nanopattern generation system (NPGS) attached to the microscope. The exposed PMMA was then developed by developer solution (a mixture of IPA and Methyl isobutyl ketone (MIBK) with 3:1 volume ratio) for 75 s and subsequently washed in IPA and de-ionized water for 1 minute. The obtained substrate was then dried by nitrogen flow. The pattern used in this work is a square array of $\Phi300$ nm windows with 1 micron window-to-window distance. The pattened windows defined the growth position of ZnO nanowires. The ZnO nanowire array was grown at $90°C$ for 12 hours with 5 mmol/L nutrition solution by hydrothermal growth method. After the growth, the PMMA layer was removed by acetone. The as-grown nanowire array was dried at $80°C$ in a convection oven. A 50-nm-thick SnO_2 nanoparticle layer was coated on the whole nanowire array by RF sputtering with a deposition rate of 0.5 Angstrom/s at $200°C$. Noble metal particles were also sputtered onto the nanowire arrays with a normalized thickness of 0.2 nm. The structure and composition of the nanowires was checked by FESEM and JEOL 2010 transmission electron microscope (TEM) equipped with X-ray energy dispersive spectroscopy (EDS).

The fabrication of gas sensor started with a ZnO nanowire array coated with SnO_2/noble metal

(Pd, Pt, or Au) nanoparticles. The whole array was first covered with PMMA (Microchem, 950A4) by spin-coating at a rotation rate of 500 rpm. The nanowire tips were then exposed by etching the PMMA layer with oxygen plasma (100W, SPI Plasma Prep II) at a rate of 80 nm/min. A 100-nm-thick Au layer was sputtered as the top electrode, the size of which was controlled to $2 \times 2\,\text{mm}^2$ by a metal mask. Finally, the PMMA was removed by acetone and dried at $80\,°\text{C}$ in a convection oven.

To test the sensing performance, the sensors were loaded into a sensor testing chamber. The *I-V* characteristics of each device was first acquired before the sensor testing. The conductance of each device was recorded continuously by a Keithley 2400 sourcemeter incorporated with a 7001 switch module when the pre-diluted gases (dry air was used as balance gas) were sent to the sensor testing chamber. The recovery of gas sensors was realized by flushing with dry air. The nanowire-array sensors are measured at room temperature and dry air was used for all the sensor testing to exclude the effects of humidity.

3.3.2.2 Gas Sensing and Discrimination by SnO_2 coated ZnO Nanowire Arrays with Different Catalytic Metal Coatings

Figure 3.15(a) shows FESEM image of as-grown ZnO nanowire array. The diameter of the pristine ZnO nanowires is $150 \sim 450\,\text{nm}$ and the length is about $3 \sim 4\,\mu\text{m}$. It can be found that multiple nanowires may grow from a single window. Some nanowires have diameters larger than the pattern size (300 nm) indicating lateral growth that induce increase of diameters. Figure 3.15(b) is a FE-SEM image of the nanowire array after SnO_2 and noble metals nanoparticle coatings. The insets enlarged from the nanowire tips show surface roughness change after the nanoparticle coating indicating complete coverage of SnO_2 nanoparticles (the average size of the particles was estimated to 20 nm). The overall morphology observed by FESEM shows that hydrothermal growth method combined with EBL patterning can precisely control the growth position of the ZnO nanowires. Figure 3.15 (c-e) are the TEM structural and composition analyses of a ZnO nanowire coated with

77
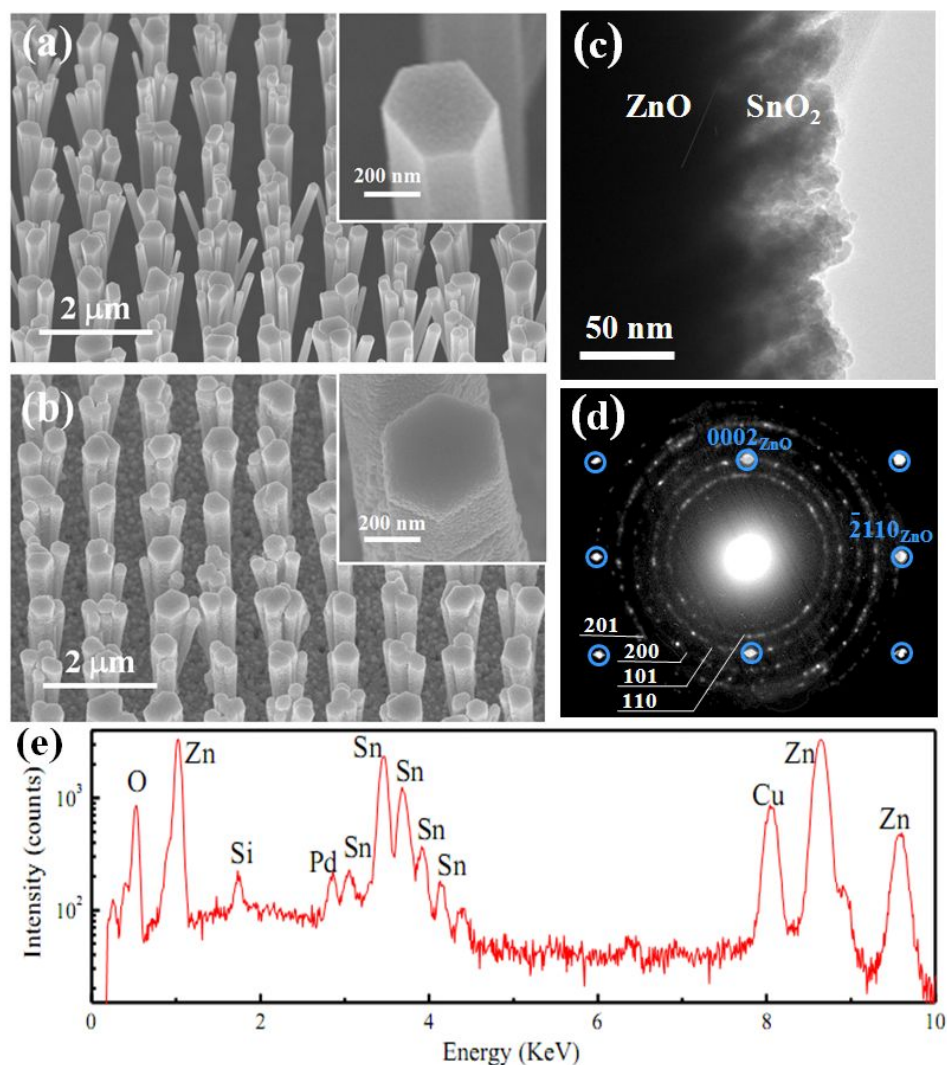
Figure 3.15: FESEM images of (a) as-grown ZnO nanowire array and (b) nanowire array after SnO$_2$ and Pd coatings. (c) TEM image on the edge of the nanowires showing the column structure of the SnO$_2$ coating. (d) Selected area electron diffraction (SAED) pattern from the nanowire along ZnO $[01\bar{1}0]$ zone. The ZnO nanowire is identified to grow along c-axis and the ring diffractions were indexed to SnO$_2$ rutile structure. (e) X-ray energy dispersive spectrum captured on the nanoparticles coated nanowire. The Cu peak originates from the copper grid for TEM observation. [144]
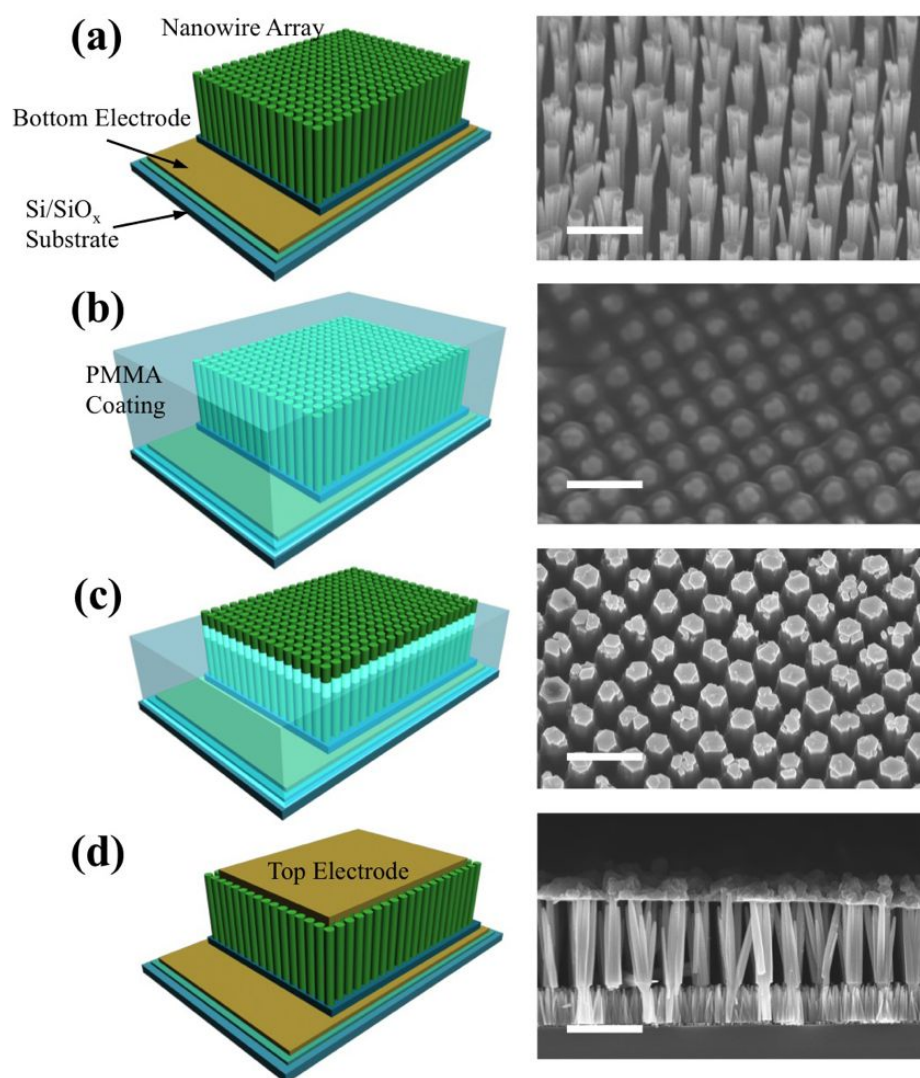
Figure 3.16: Schematic diagrams and FESEM images of overall procedures for top-electrode fabrication. Scale bars are 2 μm. [144]

SnO$_2$ and Pd nanoparticles. Figure 3.15(c) magnified from the nanowire surface reveals that the SnO$_2$ coating (The SnO$_2$ particles have an irregular shape with a diameter of about $15 \sim 20$ nm.) is formed by tilted column structures with lots of empty channels. This growth of column structures can be explained by the glazing angles between the incident deposition source and the perpendicular nanowire sidewalls [145, 146]. Figure 3.15(d) is a SAED pattern along the ZnO $[01\bar{1}0]$ zone on the nanowire, showing c-axis growth of the ZnO nanowire, which agrees with the hexagonal shape observed under FESEM. And the ring patterns were indexed to rutile SnO$_2$. The energy dispersive X-ray spectroscopy (EDS), shown in Figure 3.15(e), further confirms the coating of SnO$_2$ and Pd nanoparticles. Besides Pd nanoparticles, Pt and Au were also used as catalytic metals to improve sensor performances following exactly the same fabrication procedure in Section 3.2. The catalytic noble metal particles have an average diameter of about 2 nm with an inter-particle distance of 2 nm. The noble metal nanoparticles can effectively pre-dissociate the gas molecules into atomic species [52] and the catalytic behaviors of noble metals are different, therefore pre-dissociation process induced by noble metal decorations can not only increase the sensor sensitivity but also modify the cross-reactive behaviors of the sensors. Selective detection can be achieved by using an array of sensors with different noble metal decorations [147, 148].

Figure 3.16 shows schematics of the fabrication processes for top-electrode as well as the corresponding FESEM images. Figure 3.16(a) is a ZnO nanowire array coated with SnO$_2$/noble metal (Pd, Pt, or Au) nanoparticles. The whole array was first covered with PMMA (Figure 3.16(b)). As seen in Figure 3.16(c), the nanowire tips were then exposed by etching the PMMA layer with oxygen plasma. Figure 3.16(d) shows the final device after top electrode coating and PMMA removal. The cross-sectional FESEM image of as-prepared 3D nanowire devices shows the intervals between adjacent nanowires, which provide adequate space for gas transport.

The basic I-V characteristics (Figure 3.17) were obtained after the sensor array (ZnO/SnO$_2$/Pd, ZnO/SnO$_2$/Pt, and ZnO/SnO$_2$/Au) was loaded into the sensor testing system. For comparison, devices from pristine ZnO nanowire array were also prepared following the same fabrication pro-
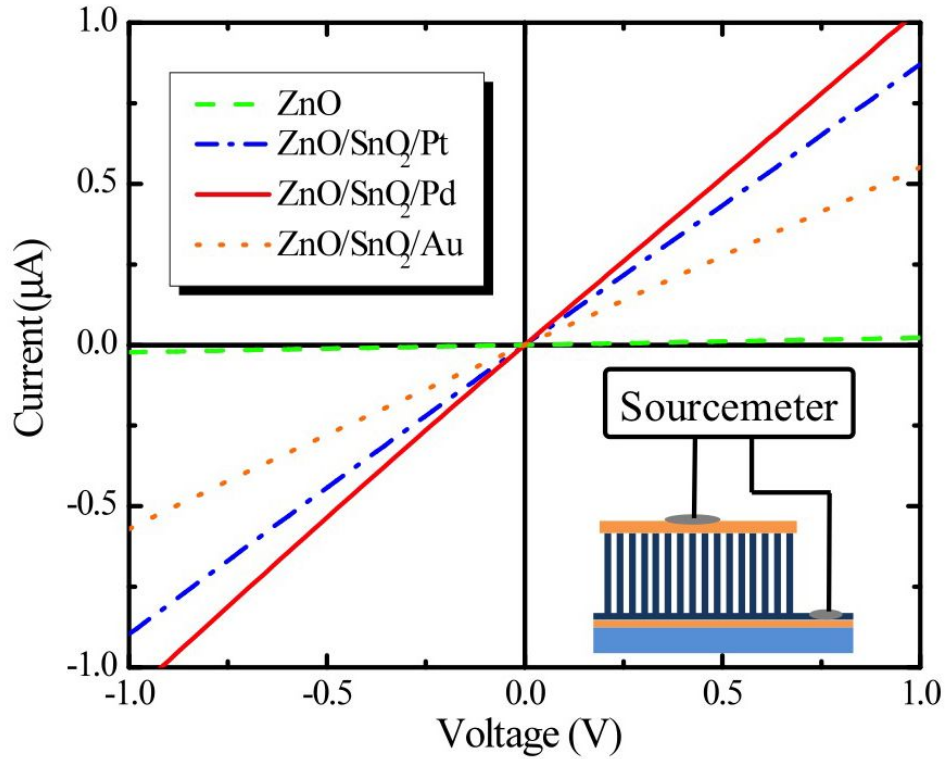
Figure 3.17: *I-V* characteristics before and after the SnO_2 and noble metal coating. The resistance of pure ZnO nanowire was more than 20 times larger than that of coated devices. The bottom-right inset is the schematic of measurement connection. [144]

cedure of the coated nanowire arrays. The linear *I-V* plots indicate that the contact between the electrodes and nanowires are all ohmic. The resistance of the pristine ZnO devices is almost 20 times larger than that of the coated nanowire array sensors, implying that the core ZnO nanowires majorly work as structural templates other than electrical channels and the major part of the current are flow through the shell nanoparticle layer. In addition, the pristine ZnO device only showed limited sensitivity compared with SnO_2/noble metal coated devices, confirming that ZnO nanowire and seed layers contribute little to the sensitivity.

The sensing responses of metal oxide conductometric gas sensors can be explained by the processes of oxygen adsorption and desorption on the metal oxide surfaces [41]. Schematic energy band diagrams near the surface of *n*-type metal oxide before and after exposure to reducing or oxidizing gases are depicted in Figure 3.18(a), showing the change of width of space charge layer,
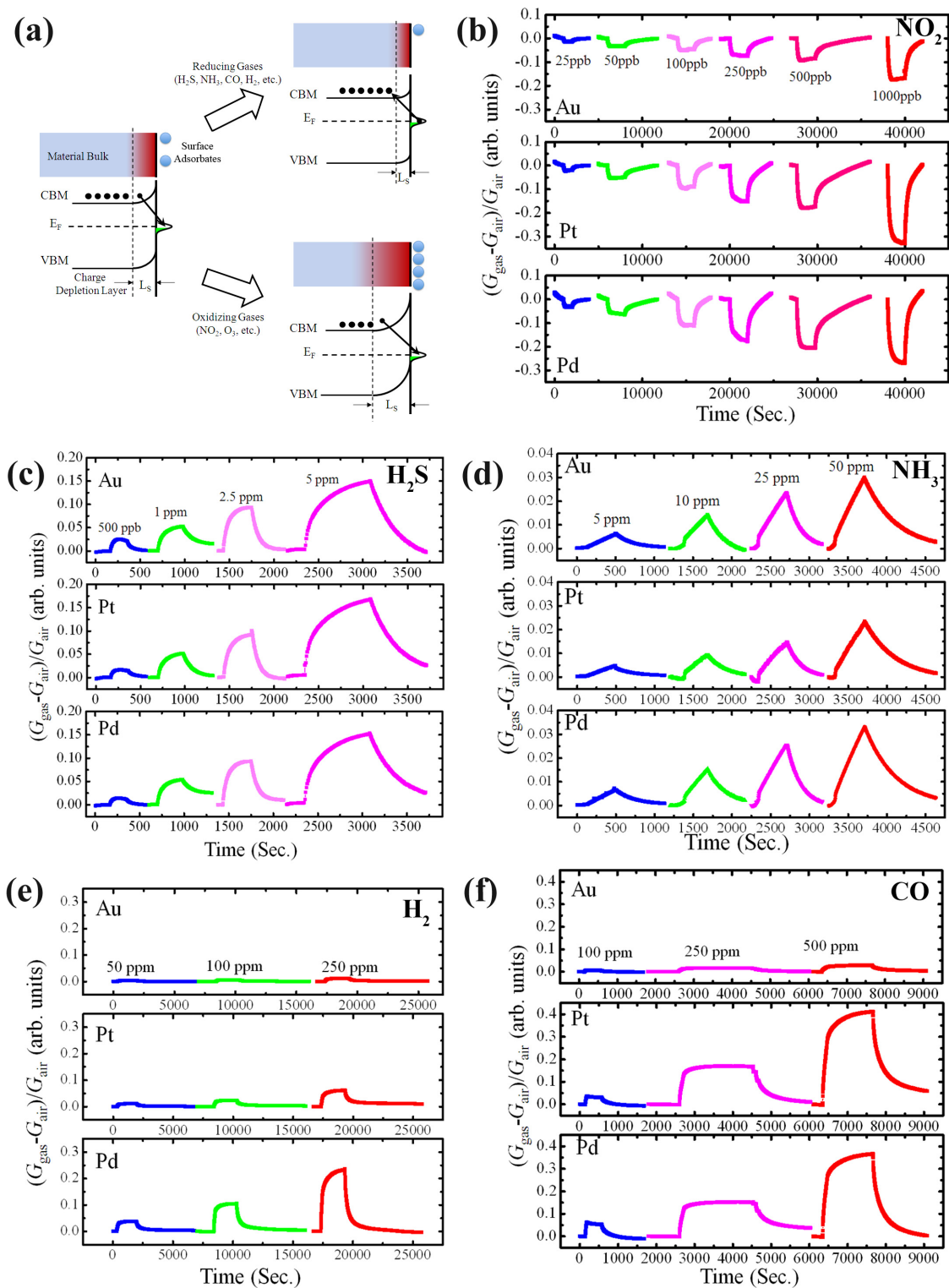
Figure 3.18: (a) Schematic and band diagrams showing the mechanism of the sensing responses. (b-f) Collection of all the normalized sensing responses to air-diluted gases: (b)NO_2, (c)H_2S, (d)NH_3, (e)H_2, and (f)CO. [144]
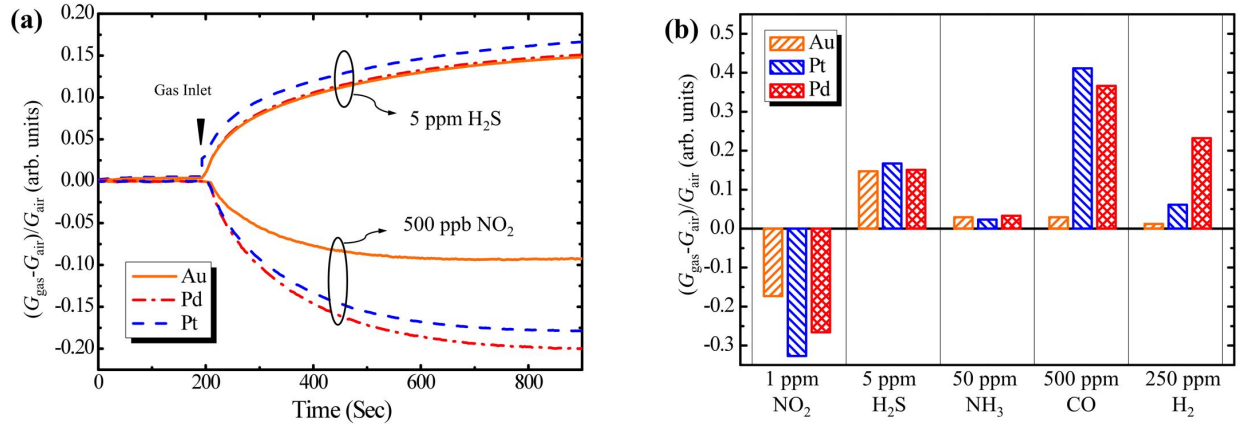
Figure 3.19: (a) Comparison of sensing responses of reducing (H_2S) and oxidizing (NO_2) gases for different noble metal modifications. (b) Bar plot summarizing the sensing responses of all the devices to five different gases.

L_S. Before exposure to the testing gases, oxygen molecules in atmosphere are adsorbed on the metal oxide surfaces and become adsorbates (O_2^-, O_2^{2-}, O^{2-}, etc.), which can be described by

$$O_2 + e \rightarrow nO^- (or\, O_2^-, O^{2-}...) \tag{3.3}$$

These adsorbates work as surface states and trap electrons from the *n*-type metal oxides, forming a carrier depletion layer. It is important to point out that the oxygen adsorbates are molecule-ion species (O_2^-, O_2^{2-}) at room temperature according to Barsan's report [41].The carrier depletion layer decreases the cross-section of effective conduction channel in the material bulk and increases the inter-particle energy barriers, which suppress the conductivity of *n*-type metal oxides. Reducing gases (H_2S, NH_3, CO, etc.) may react with the adsorbed oxygen adsorbates and release the electrons back to the metal oxides, thereby causing increase of electrical conductance, as described
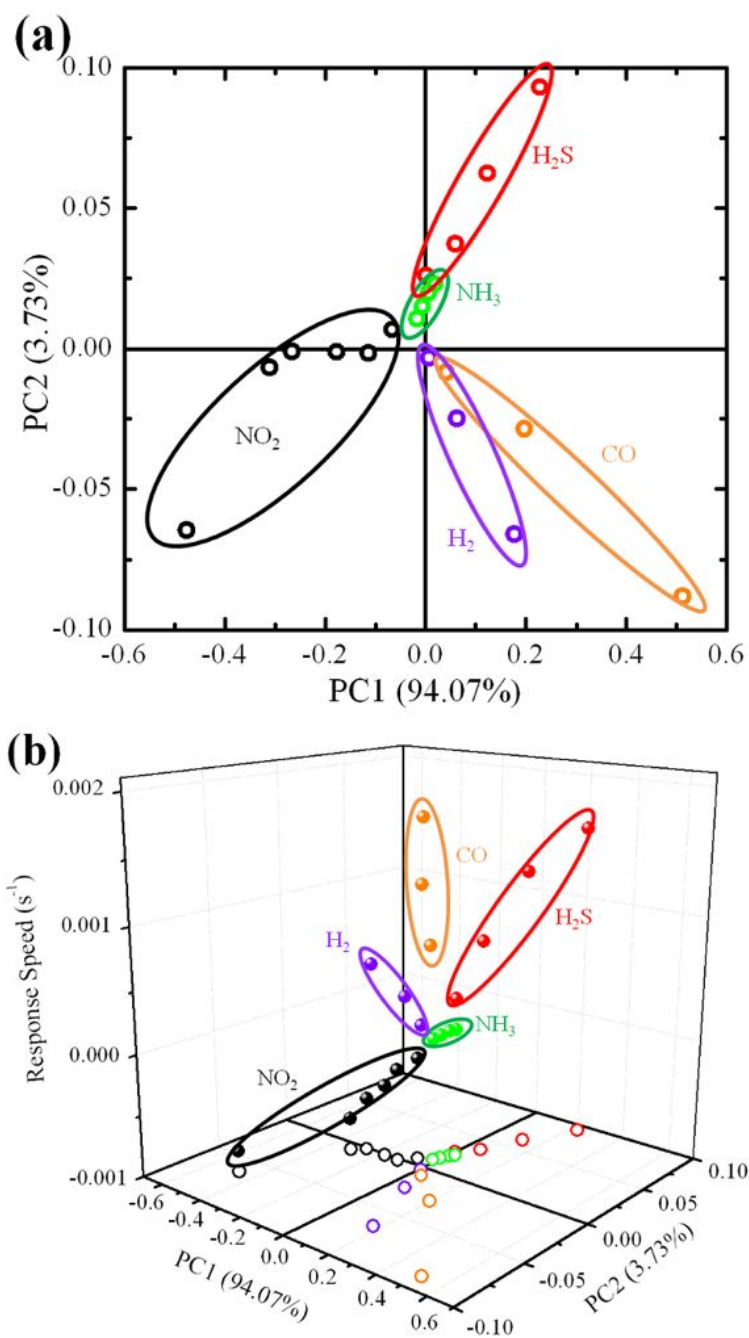
Figure 3.20: (a) PCA plot of sensing responses of the sensor array. The data points for same gas are grouped by clusters. (b) Plot of PCA data after incorporating response speeds as an extra discrimination factor. [144]

by

$$2H_2 + O_2^- \rightarrow 2H_2O + e,$$

$$2CO + O_2^- \rightarrow 2CO_2 + e,$$

$$4NH_3 + 3O_2^- \rightarrow 6H_2O + 2N_2 + 3e, \quad (3.4)$$

$$2H_2S + 3O_2^- \rightarrow 2H_2O + 2SO_2 + 3e.$$
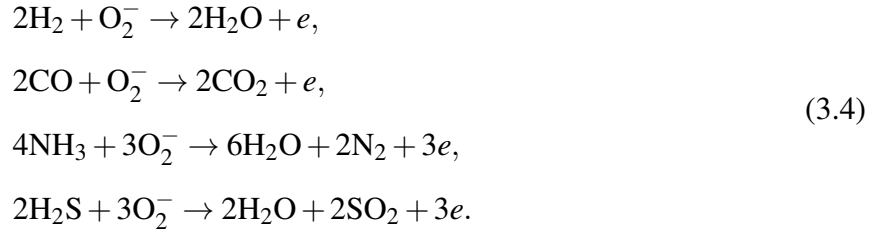
On contrary, oxidizing gases like NO_2 decrease the device conductance by trapping more electrons from the n-type metal oxides, as given by

$$NO_2 + e \rightarrow NO_2^-. \quad (3.5)$$

Therefore, it is relative easy to discriminate oxidizing gases from reducing gases by monitoring the conductance change.

To build a "smell-print" knowledge database for gas discrimination, the sensing responses were measured with air-diluted NO_2, H_2S, NH_3, CO, and H_2 of different concentrations at room-temperature. All normalized sensing response, $(G_{gas} - G_{air})/G_{air}$, are plotted in Figure 3.18 (b-f), where G_{gas} and G_{air} are the device conductances in the testing gases and dry air, respectively. The devices show high sensitivity to H_2S and NO_2 at room temperature, the lowest detection limits of which are as low as 500 ppb and 25 ppb, respectively. The response speed, measured by the duration from gas inlet to 90 % of sensing response was reached, were estimated to be about $10 \sim 15$ minutes. Some important response features for different noble metal coatings are shown in Figure 3.19. It was clearly shown that the devices give positive response to reducing gases while negative responses were observed for oxidizing gas, so NO_2 can be easily distinguished based on the conductance change. In addition to NO_2 and H_2S, NH_3 can be detected at room temperature with a detection limit of 5 ppm. Though the detection limits of H_2S and NH_3 are very different, but without knowing their concentrations, it is impossible to discriminate them only by the values of relative sensitivity. CO and H_2 are generally difficult to be detected at room temperature by metal

oxide conductometric sensors. Our devices can detect air-diluted CO and H_2 at room temperature, which can be ascribed to the large surface area of the nanowire arrays and the catalytic effect of noble-metal decorations. CO and H_2 show distinct response patterns for different noble-metal decorations indicating the noble metals not only help to increase the sensitivity but also enhance the selectivity for these two types of gases.

There are many statistical methods that can be used to analyze the response data of sensor array, such as principal component analysis (PCA), partial least squares (PLS), multiple linear regression (MLR), principal component regression (PCR), discrimination function analysis (DFA) [77, 149]. Among all of these methods, PCA is widely used to display the sensing responses of sensor array because it is a linear unsupervised method that require no or little prior knowledge, and in most case, only response variables (i.e. response strength, speed) are needed. Generally, it is difficult to plot the response vectors if more than 3 response variables are used. PCA can effectively reduce the dimensionality of the response data and maintain the major part of the information by using covariance analysis [77, 149]. All the data acquired by sensor array can be represented by response matrix $R_{m \times n}$. Each column of R corresponds to one type of the targeting gas with a specific concentration while rows are the responses for a sensor device at different measurements. We first consider the response strengths as the variables for PCA analysis. Since there are three independent sensors, each column in the response matrix corresponds to a vector in 3D space. Using a self-programmed PCA code that conducts singular value decomposition (SVD), the 3D data are projected to 2D principle component space. The plot in first two principle component space is illustrated in Figure 3.20(a). The cumulative variance of the principle components (PC1 and PC2) is 98.80 % indicating the 2D diagram abstract the major information from the raw data. Data points are grouped into clusters based on the types of tested gases. Most of the clusters are well separated, which reveals the sensor array has strong discrimination capability for these chemicals. One can easily identify that NO_2, H_2, and CO have distinct response trends as the concentration increases, while H_2S and NH_3 share similar change direction, which means it is difficult to distinguish H_2S

and NH$_3$. In addition, the clusters of CO and H$_2$ overlap at low concentration regions, which also bring ambiguity for gas discrimination towards CO and H$_2$.

As one can see, the gas sensors also show very different response speeds when exposed to different tested gases, therefore, the response speeds could help to increase the capability of gas discrimination. Figure 3.20(b) includes the response speeds (the slopes of response curves right after the gas exposure) into the PCA plot. By comparing to Figure 3.20(a), it can be found that the response speeds significantly enhance the capability of gas discrimination. No overlaps are found in all clusters and they tend to change along different directions. This enhancement of selectivity can be ascribed to the different adsorption and desorption dynamics for different gases. Another method to increase the selectivity of sensor array is to include more sensors built with new materials, which needs to be studied in future works.

3.3.2.3 Summary

In summary, vertically aligned ZnO nanowire array was grown on thermal oxidized Si substrate by hydrothermal method, which provided a 3D structural template for gas sensor fabrication. SnO$_2$/noble metal nanoparticles coated on nanowire arrays contributed the major part of the sensing responses. The gas sensors showed room-temperature responses to NO$_2$ and H$_2$S down to ppb level. The high sensitivity of these devices can be attributed to the large surface area of their 3D structure and catalytic behaviors of noble metals. A sensor array composed of 3D sensors with different noble metal decorations (Pd, Pt, and Au) was also used for selective detection. The sensor array has capability to discriminate five different gases (NO$_2$, H$_2$S, NH$_3$, CO and H$_2$). This work provides a rational strategy to prepare sensing devices with 3D structures and it can be readily expanded to other sensing materials that are difficult to be grown as nanowire arrays.

Chapter 4

Conclusions and Future Perspectives

Mammal's biological olfactory systems have extremely high performance for gas detection and identification. In the last few decades, many research groups are pursuing gas sesnsors that have performance comparable to or surpass biological olfactory systems. There are several important factors that define the high performance of biological olfactory system: the olfactory receptors have a wire shape with several micrometer in length and hundred nanometers in diameter, the array of which providing tremendous surface area for gas molecule captures; the chemical properties of the olfactory receptors are highly diversified, which makes them have strong capability of gas discrimination; the detected biological signals are transmitted and processed in a massively parallel way, which provides extremely fast response and gas identification.

Nanostrutures have some intrinsic properties that can significantly enhance the sensing performance of conventional metal oxide conductometric gas sensors, such as, large surface-to-volume ratio, feature size close to characteristic Debye length, etc. Accordingly, more and more efforts have been put into the applications of metal oxide nanostructures for gas detection. Metal oxide nanowire arrays share similar 3D structures as the array of mammal's olfactory receptors. The large surface area from the 3D nanostructures may further increase the performance of gas sensors. However, there are only several demonstration of gas sensors based on 3D metal oxide nanowire arrays due to the difficulty and stability of nanostructure fabrication and device integration. In this dissertation, two standalone gas sensors based on metal oxide nanowire arrays prepared by micro-fabrication and *in-situ* micromanipulation have been demonstrated. The sensors based on WO_3

nanowire arrays can detect 50 ppb NO_2 with a fast response speed; well-aligned CuO nanowire array present new detection mechanism, which can identify H_2S at a concentration of 500 ppb. To expand the material library of 3D metal oxide nanowire arrays for gas sensing, a general route for fabrication of polycrystalline metal oxide nanowire array by using ZnO nanowire arrays as structural templates has been introduced. The effectiveness of this method for high performance gas sensing was first investigated by single-nanowire devices. The polycrystalline metal oxide coatings showed high performance for gas detection and their sensitivity can be further enhanced by catalytic noble metal decorations. To form electronic nose systems, different metal oxide coatings and different catalytic decorations were employed to diversify the chemical reactivity of the sensors. The systems can work at room temperature and have a capability of gas discrimination towards five different gases.

Though 3D nanowire arrays present many advantages that can increase the performance over conventional thin film techniques, the applications of metal oxide nanowire arrays in gas detection are still limited. Lots of work may be done in the future for development of novel gas detection systems using metal oxide nanowire arrays:

1. The effects of structural parameters (i.e. nanowire diameters, inter-nanowire distances, thickness of shell-layer coatings, etc.) on the sensing performance should be studied in details for device optimization.

2. The materials library for 3D nanowire array gas sensors must be further expanded in order to create electronic noses with performance comparable to mammal's biological olfactory system.

3. Due to the large surface area, the recovery of 3D nanostructures is generally a slow process. Some new recovery mechanism may be developed, for instances, UV irradiation, high temperature flashes, etc.

4. The level of parallelism of signal transmission and processing is extremely high in biological

systems. To reach similar parallelism, new techniques for individual nanowire decorations and connections may be needed. Recently, a method that can connect individual standing nanowires has been demonstrated, which provides a feasible framework for devices parallelization [150].

The conventional van Neumann electronic computing structure that majorly relies on serial processes with a powerful computing units (CPU) may also been revolutionized so that the signal processing systems can meet the requirements of man-made olfactory systems. To simulate human's brain, some new computing frameworks have been developed to increase the parallelism of computing, such as neuromorphic computing [151], graphic processing units for general purpose computing [152], which may overcome the bottle-neck at the aspect of signal processing. The construction of man-made olfactory systems is a multi-disciplinary topic that relies on research on electronics, communications, computer sciences, and neuroscience, etc.

Appendix A

Gas Sensor Testing System Used in This Dissertation

The overall diagram of the gas sensing testing system is shown in Figure A.1. The gas sensor testing cell is a glass tube with a volume of 40 mL that host the gas sensor testing head (shown in Figure A.2). After the sensors are loading onto the test system, the conductances and resistances of all the devices are monitored simultaneously by the electrical measurement system. The electrical measurement system consists of a Keithley 7001 switch module, a 2400 source measurement unit, and a computer that synchronizes the measurements and retreat the data. The 7001 switch module has 40 channels that can specifically select which device to be measured. The 2400 source unit provides constant voltage or current source and detects the device current or voltage when the device is selected by the 7001 module. The simultaneous measurement is realized by continuous scanning of conductances of all the devices.

The detection head is composed of a high-power resistor with ceramic packages, which can heat the gas sensors from room temperature to 200 °C. The real temperature of the heater surface is measured by a thin film Pt sensor that is attached by silver paste. Eight electrical connections are provided for sensor connections. If one connection is used as common ground, the detection head can connect seven individual two-terminal devices.
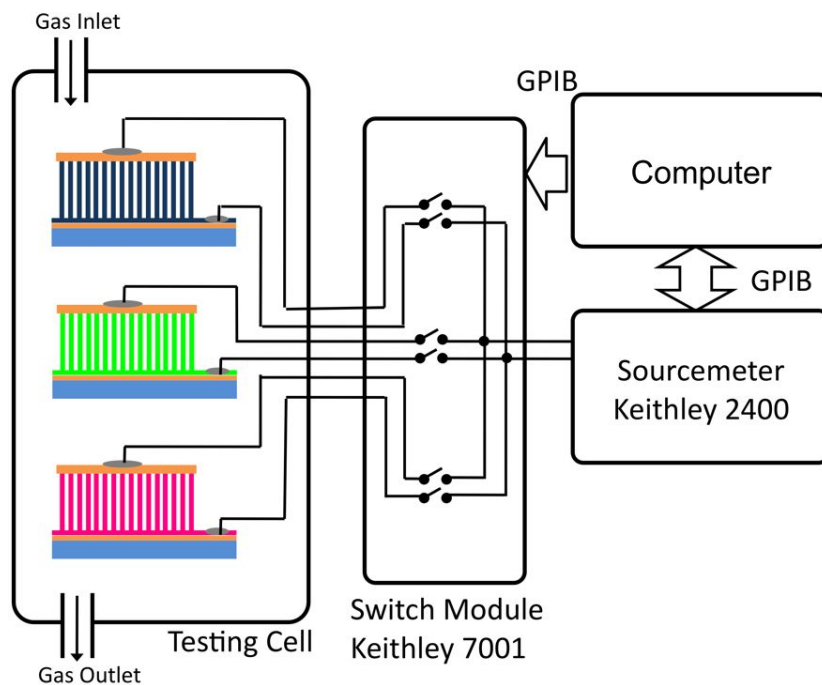
Figure A.1: Schematic of the multi-sensor testing system. Computer controlled switch module and source measurement unit are used to probe the conductivity of all the devices loaded in the system.
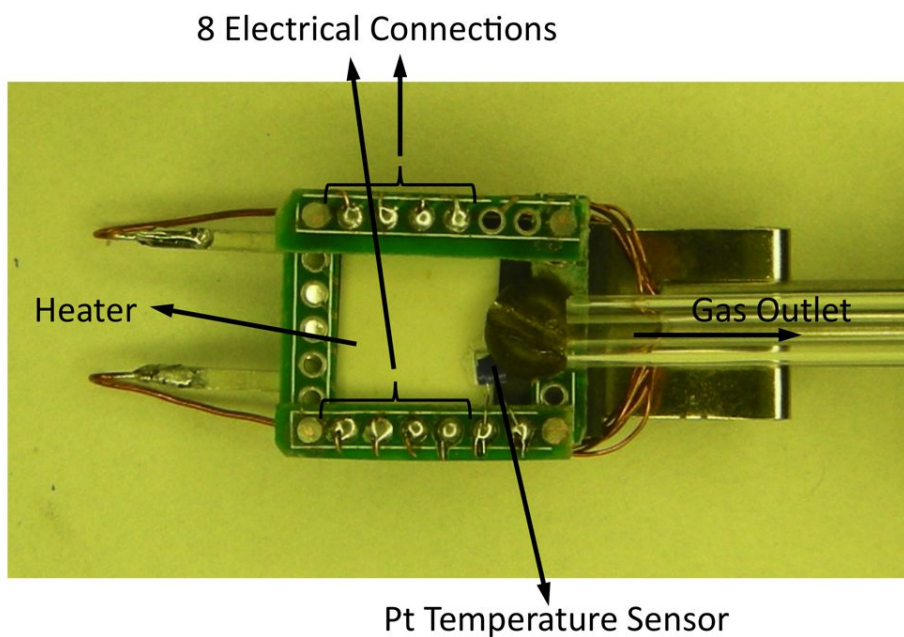
Figure A.2: Photograph of the detection head (including device heater, temperature sensor, and electrical connections) used in this dissertation.

Appendix B

Data Extracted from a Responsive Curve of Gas Sensor Testing
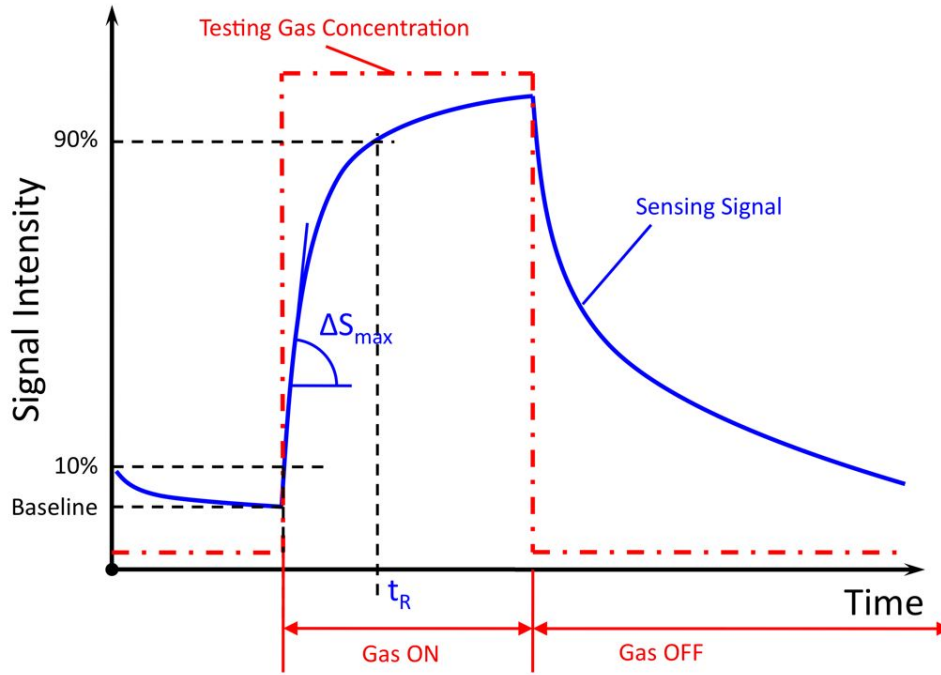
Figure B.1: A schematic response curve of gas sensor testing. The typical characteristic values extracted from the measurement are identified on the plots.

There are two major schemes that can monitor the conductance changes of the gas sensors: constant voltage or constant current. In this dissertation, constant voltage is applied onto the gas sensors and the currents flow through the two-terminal sensors are monitored. A typical response curve to a pulse of testing gas is depicted in Figure B.1. The red dashed curve indicates the concentration of the testing gas and the blue curve is the response signal collected by electronic

meters. The response time t_R is defined by the transition time from 10% to 90% of full scale response. The response speed can be calculated by the maximum slope ($\Delta S_{\max}$) of the response curve after the testing gas pulse is inlet. In this dissertation, the fractional conductance/resistance changes are employed to evaluate the sensing responses of gas sensors to the gas with specific concentration, which are generally calculated as:

$$S = (G_{\text{gas}} - G_0)/G_0, \tag{B.1}$$

or

$$S = (R_{\text{gas}} - R_0)/R_0, \tag{B.2}$$

where S is the sensing response, G_{gas} and R_{gas} are the conductance and resistance when devices are exposed to testing gas, G_0 and R_0 are the baseline values when the devices are stabilized in atmosphere. Using fractional values to represent the sensing responses can effectively compensate for the temperature cross-sensitivties and nonlinearities of concentration dependence [153], so it is widely used in metal oxide conductometric gas sensors.

In many research paper of gas sensors, the fractional conductance changes are also defined as the sensitivity of the gas sensors. Actually, this is different from the definition in analytical chemistry, where the "sensitivity" is explicitly defined as the slope of calibration curve. To avoid the confusion, the definition must be claimed when the sensitivity is represented by the fractional conductance/resistance changes.

Appendix C

Principle Component Analysis

In the gas testing experiment of a electronic nose, multiple gas sensors are exposed to serial gases with different concentrations. The response data can be collectively represented by a response matrix,

$$R_{m \times n}, \tag{C.1}$$

where the columns of R represent the responses to one specific gas with certain concentration, while the rows of R are the responses for one sensors at different measurements, m is the number of gas sensors, and n is the number of measurements. If the number of gas sensors, m, is more than 3, it is very difficult to depict the high-degree data in a plot for visualization and analysis. Principle component analysis (PCA) is a widely-used mathematical technique that can be used to reduce the dimensionality of data set and maintain the major part of the useful information. The working mechanism can be simply illustrated by the projection of a donut shape, as shown in Figure C.1. A three dimensional donut can be projected into 2-dimensional figures and there are many ways to do this projection. For examples, it can be projected to x-y plane or y-z plane (Figure C.1). Obviously, the projection in x-y plane maintains the major part of the structural information of the donut shape. PCA is a mathematical way to select the best project direction.

The PCA on the response matrix, $R_{m \times n}$, can be realized by singular value decomposition (SVD), as shown in the following procedures [154]:

1. Substrate the mean of measurement for each devices obtaining new response matrix, X.

2. Construct a new matrix for singular value decomposition (SVD),
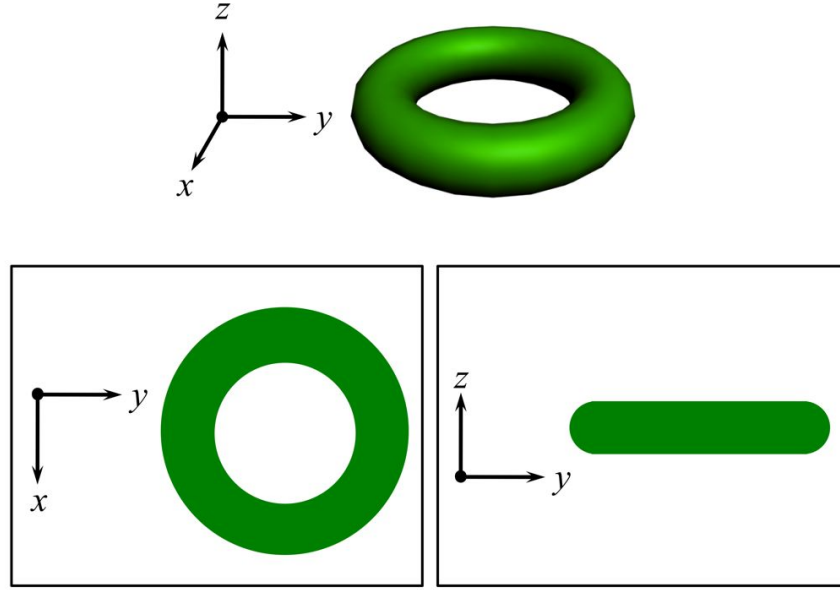
Figure C.1: Schematics showing how a donut structure in three dimensional space can be projected into two dimensional planes, which presents the importance of principle component analysis (PCA).

$$Y \equiv \frac{1}{\sqrt{n}}X^T \tag{C.2}$$

3. Apply SVD on the matrix Y:

$$Y = U\Sigma V^T, \tag{C.3}$$

where U and V are orthogonal matrices, Σ is a diagonal matrix. The column of V is the principle components of $\mathbb{R}$. The projected data on principle component basis are given as:

$$PCA = V^T X. \tag{C.4}$$

The first two or three rows of the data in *PCA* can be used to plot in 2D or 3D graph for data visualization. The variance values extracted from Σ represent the importance of the components.

Appendix D

Copyright Permissions

Dear Mr Chen

The Royal Society of Chemistry hereby grants permission for the use of the material specified below in the work described and in all subsequent editions of the work for distribution throughout the world, in all media including electronic and microfilm. You may use the material in conjunction with computer-based electronic and information retrieval systems, grant permissions for photocopying, reproductions and reprints, translate the material and to publish the translation, and authorize document delivery and abstracting and indexing services. The Royal Society of Chemistry is a signatory to the STM Guidelines on Permissions (available on request).

Please note that if the material specified below or any part of it appears with credit or acknowledgement to a third party then you must also secure permission from that third party before reproducing that material.

Please ensure that the published article carries a credit to The Royal Society of Chemistry in the following format:

[Original citation] – Reproduced by permission of The Royal Society of Chemistry

and that any electronic version of the work includes a hyperlink to the article on the Royal Society of Chemistry website. The recommended form for the hyperlink is http://dx.doi.org/10.1039/*DOI suffix*, for example in the link http://dx.doi.org/10.1039/b110420a the DOI suffix is 'b110420a'. To find the relevant DOI suffix for the RSC paper in question, go to the Journals section of the website and locate your paper in the list of papers for the volume and issue of your specific journal. You will find the DOI suffix quoted there.

Regards

Gill Cockhead
Contracts & Copyright Executive

Gill Cockhead (Mrs), Contracts & Copyright Executive
Royal Society of Chemistry, Thomas Graham House
Science Park, Milton Road, Cambridge CB4 0WF, UK
Tel +44 (0) 1223 432134, Fax +44 (0) 1223 423623
http://www.rsc.org

```
-----Original Message-----
From: jchen2@uno.edu [mailto:jchen2@uno.edu]
Sent: 12 October 2010 18:31
To: CONTRACTS-COPYRIGHT (shared)
Subject: Permission Request Form: Jiajun Chen


Name    : Jiajun Chen
Address :

2048 Science Bldg.
University of New Orleans
LA 70148, USA

Tel     : 504-638-4445
Fax     : 504-280-3185
Email   : jchen2@uno.edu

I am preparing the following work for publication:

Article/Chapter Title  : "Highly Sensitive and Selective Gas Sensors Based on Vertically Aligned Metal
Oxide Nanowire Arrays"
Journal/Book Title     : Ph. D Dissertation
Editor/Author(s)       : Jiajun Chen
Publisher              : ProQuest

I would very much appreciate your permission to use the following material:
```

Any Additional Comments   :

Dear Sir/Madam,

I am currently writing my Ph. D Dissertation. I would like to enclose some contents of my published paper (equally contributed first authors) into my dissertation. Would you please help me to issue a permission to reuse the contents?

Your help is appreciated very much!

Best Wishes,

Jiajun Chen

**AMERICAN CHEMICAL SOCIETY LICENSE
TERMS AND CONDITIONS**

Oct 19, 2010

This is a License Agreement between Jiajun Chen ("You") and American Chemical Society ("American Chemical Society") provided by Copyright Clearance Center ("CCC"). The license consists of your order details, the terms and conditions provided by American Chemical Society, and the payment terms and conditions.

All payments must be made in full to CCC. For payment instructions, please see information listed at the bottom of this form.

License Number	2532540660904
License Date	Oct 19, 2010
Licensed content publisher	American Chemical Society
Licensed content publication	The Journal of Physical Chemistry C
Licensed content title	H2S Detection by Vertically Aligned CuO Nanowire Array Sensors
Licensed content author	Jiajun Chen et al.
Licensed content date	Oct 1, 2008
Volume number	112
Issue number	41
Type of Use	Thesis/Dissertation
Requestor type11	Not specified
Format	Print and Electronic
Portion	50% or more of original article
Author of this ACS article	Yes
Order reference number	
Title of the thesis / dissertation	Highly Sensitive and Selective Gas Sensors Based on Vertically Aligned Metal Oxide Nanowire Arrays
Expected completion date	Dec 2010
Estimated size(pages)	150
Billing Type	Invoice
Billing Address	312 E St Jean Baptist St
	Chalmette, LA 70043
	United States
Customer reference info	

Thesis/Dissertation

ACS / RIGHTSLINK TERMS & CONDITIONS
THESIS/DISSERTATION

INTRODUCTION
The publisher for this copyrighted material is the American Chemical Society. By clicking
"accept" in connection with completing this licensing transaction, you agree that the
following terms and conditions apply to this transaction (along with the Billing and Payment
terms and conditions established by Copyright Clearance Center, Inc. ("CCC"), at the time
that you opened your Rightslink account and that are available at any time at
<http://myaccount.copyright.com>).

LIMITED LICENSE
Publisher hereby grants to you a non-exclusive license to use this material. Licenses are for
one-time use only with a maximum distribution equal to the number that you identified in
the licensing process; any form of republication must be completed within 60 days from the
date hereof (although copies prepared before then may be distributed thereafter).

GEOGRAPHIC RIGHTS: SCOPE
Licenses may be exercised anywhere in the world.

RESERVATION OF RIGHTS
Publisher reserves all rights not specifically granted in the combination of (i) the license
details provided by you and accepted in the course of this licensing transaction, (ii) these
terms and conditions and (iii) CCC's Billing and Payment terms and conditions.

PORTION RIGHTS STATEMENT: DISCLAIMER
If you seek to reuse a portion from an ACS publication, it is your responsibility to examine
each portion as published to determine whether a credit to, or copyright notice of, a third
party owner was published adjacent to the item. You may only obtain permission via
Rightslink to use material owned by ACS. Permission to use any material published in an
ACS publication, journal, or article which is reprinted with permission of a third party must
be obtained from the third party owner. ACS disclaims any responsibility for any use you
make of items owned by third parties without their permission.

REVOCATION
The American Chemical Society reserves the right to revoke a license for any reason,
including but not limited to advertising and promotional uses of ACS content, third party
usage, and incorrect figure source attribution.

LICENSE CONTINGENT ON PAYMENT

While you may exercise the rights licensed immediately upon issuance of the license at the end of the licensing process for the transaction, provided that you have disclosed complete and accurate details of your proposed use, no license is finally effective unless and until full payment is received from you (by CCC) as provided in CCC's Billing and Payment terms and conditions. If full payment is not received on a timely basis, then any license preliminarily granted shall be deemed automatically revoked and shall be void as if never granted. Further, in the event that you breach any of these terms and conditions or any of CCC's Billing and Payment terms and conditions, the license is automatically revoked and shall be void as if never granted. Use of materials as described in a revoked license, as well as any use of the materials beyond the scope of an unrevoked license, may constitute copyright infringement and publisher reserves the right to take any and all action to protect its copyright in the materials.

COPYRIGHT NOTICE: DISCLAIMER
You must include the following copyright and permission notice in connection with any reproduction of the licensed material: "Reprinted ("Adapted" or "in part") with permission from REFERENCE CITATION. Copyright YEAR American Chemical Society."

WARRANTIES: NONE
Publisher makes no representations or warranties with respect to the licensed material.

INDEMNITY
You hereby indemnify and agree to hold harmless publisher and CCC, and their respective officers, directors, employees and agents, from and against any and all claims arising out of your use of the licensed material other than as specifically authorized pursuant to this license.

NO TRANSFER OF LICENSE
This license is personal to you or your publisher and may not be sublicensed, assigned, or transferred by you to any other person without publisher's written permission.

NO AMENDMENT EXCEPT IN WRITING
This license may not be amended except in a writing signed by both parties (or, in the case of publisher, by CCC on publisher's behalf).

OBJECTION TO CONTRARY TERMS
Publisher hereby objects to any terms contained in any purchase order, acknowledgment, check endorsement or other writing prepared by you, which terms are inconsistent with these terms and conditions or CCC's Billing and Payment terms and conditions. These terms and conditions, together with CCC's Billing and Payment terms and conditions (which are incorporated herein), comprise the entire agreement between you and publisher (and CCC) concerning this licensing transaction. In the event of any conflict between your obligations established by these terms and conditions and those established by CCC's Billing and Payment terms and conditions, these terms and conditions shall control.

JURISDICTION

This license transaction shall be governed by and construed in accordance with the laws of the District of Columbia. You hereby agree to submit to the jurisdiction of the courts located in the District of Columbia   for purposes of resolving any disputes that may arise in connection with this licensing transaction.

THESES/DISSERTATION TERMS
Publishing implications of electronic publication of theses and dissertation material
Students and their mentors should be aware that posting of theses and dissertation material on the Web prior to submission of material from that thesis or dissertation to an ACS journal may affect publication in that journal. Whether Web posting is considered prior publication may be evaluated on a case-by-case basis by the journal's editor. If an ACS journal editor considers Web posting to be "prior publication", the paper will not be accepted for publication in that journal. If you intend to submit your unpublished paper to ACS for publication, check with the appropriate editor prior to posting your manuscript electronically.

If your paper has already been published by ACS and you want to include the text or portions of the text in your thesis/dissertation in **print or microfilm formats**, please print the ACS copyright credit line on the first page of your article: "Reproduced (or 'Reproduced in part') with permission from [FULL REFERENCE CITATION.] Copyright [YEAR] American Chemical Society." Include appropriate information.

Submission to a Dissertation Distributor: If you plan to submit your thesis to UMI or to another dissertation distributor, you should not include the unpublished ACS paper in your thesis if the thesis will be disseminated electronically, until ACS has published your paper. After publication of the paper by ACS, you may release the entire thesis (**not the individual ACS article by itself**) for electronic dissemination through the distributor; ACS's copyright credit line should be printed on the first page of the ACS paper.

Use on an Intranet: The inclusion of your ACS unpublished or published manuscript is permitted in your thesis in print and microfilm formats. If ACS has published your paper you may include the manuscript in your thesis on an intranet that is not publicly available. Your ACS article cannot be posted electronically on a publicly available medium (i.e. one that is not password protected), such as but not limited to, electronic archives, Internet, library server, etc. The only material from your paper that can be posted on a public electronic medium is the article abstract, figures, and tables, and you may link to the article's DOI or post the article's author-directed URL link provided by ACS. This paragraph does not pertain to the dissertation distributor paragraph above.

Other conditions:

v1.1

Gratis licenses (referencing $0 in the Total field) are free. Please retain this printable license for your reference. No payment is required.

If you would like to pay for this license now, please remit this license along with your payment made payable to "COPYRIGHT CLEARANCE CENTER" otherwise you will be invoiced within 48 hours of the license date. Payment should be in the form of a check or money order referencing your account number and this invoice number RLNK10868611.
Once you receive your invoice for this order, you may pay your invoice by credit card. Please follow instructions provided at that time.

Make Payment To:
Copyright Clearance Center
Dept 001
P.O. Box 843006
Boston, MA 02284-3006

If you find copyrighted material related to this license will not be used and wish to cancel, please contact us referencing this license number 2532540660904 and noting the reason for cancellation.

Questions? customercare@copyright.com or +1-877-622-5543 (toll free in the US) or +1-978-646-2777.

Comments/Response to Case ID: 006D7FD0

ReplyTo: Pubs-Permissions@ieee.org

    From: Jacqueline Hansson   Date: 10/18/2010

  Subject: Re: Reuse   Send To: Jiajun Chen <jchen2@uno.edu>
          previously-published
          materials in my
          dissertation

                             cc:

Dear Jiajun Chen   :

We are happy to grant you permission to reprint portions of the described
IEEE copyrighted paper.. We have two requirements that must be satisfied
before we can consider this permission final:

(1) In the case of textual material (i.e., using short quotes or referring
to the work within these papers), you must give full credit to the original
source (author, paper, publication) followed by the IEEE copyright line (©
[Year] IEEE. In the case of illustrations or tabular material, we require
that the copyright line appears prominently with each reprinted figure
and/or table.

2) If you expect to use a substantial portion of the original paper, and
if you are not the senior author. you must obtain the senior author's
approval and the following credit notice must appear on the first page of
the reprinted material, with the appropriate details filled in:

Portions reprinted, with permission, from (complete publication
information). © [Year] IEEE.

Sincerely,

Jacqueline Hansson

IEEE IPR Coordinator
© © © © © © © © © © © © © © © © © © ©
 IEEE Intellectual Property Rights Office
445 Hoes Lane
Piscataway, NJ 08855-1331 USA
+1 732 562 3966 (phone)
+1 732 562 1746 (fax)

IEEE-- Fostering technological innovation
and excellence for the benefit of humanity.
© © © © © © © © © © © © © © © © © © ©

To whom it may concern,

I am writing my Ph. D dissertation titled "Highly Sensitive and Selective Gas Sensors Based on Vertically Aligned Metal Oxide Nanowire Arrays" which will be finally published by ProQuest. I would like to reuse the "Results and discussion" part in my dissertation:

Title: "Facile Route to Polycrystalline Pd/ ${rm SnO}_{2}$ Nanowires Using ZnO-Nanowire Templates for Gas-Sensing Applications"
Authors: Jiajun Chen;   Kai Wang;   Rong Huang;   Saito, T.;   Ikuhara, Y.H.;   Hirayama, T.;   Weilie Zhou;
This paper appears in: Nanotechnology, IEEE Transactions on
Issue Date: Sept. 2010
Volume: 9 Issue:5
On page(s): 634 - 639
ISSN: 1536-125X
INSPEC Accession Number: 11513423
Digital Object Identifier: 10.1109/TNANO.2010.2052629
Date of Publication: 14 June 2010
Date of Current Version: 07 September 2010

Your help is appreciated very much!

Jiajun Chen
Research Assistant
****
Advanced Materials Research Institute
2048 Science Bldg.
University of New Orleans
Tel: 504-280-1087
Fax: 504-280-3185
email: jchen2@uno.edu
****

References

[1] Richard P. Feynman. There's plenty of room at the bottom. *Engineering and Science*, (February), 1960.

[2] William E. Buhro and Vicki L. Colvin. Semiconductor nanocrystals: Shape matters. *Nat Mater*, 2(3):138–139, 2003.

[3] H. W. Kroto, J. R. Heath, S. C. O'Brien, R. F. Curl, and R. E. Smalley. C_{60}: Buckminster-fullerene. *Nature*, 318(6042):162–163, 1985.

[4] Sumio Iijima and Toshinari Ichihashi. Single-shell carbon nanotubes of 1-nm diameter. *Nature*, 363(6430):603–605, 1993.

[5] Ganhua Lu, Leonidas E. Ocola, and Junhong Chen. Room-temperature gas sensing based on electron transfer between discrete tin oxide nanocrystals and multiwalled carbon nanotubes. *Adv. Mater.*, 21(24):2487–2491, 2009.

[6] K. S. Novoselov, A. K. Geim, S. V. Morozov, D. Jiang, Y. Zhang, S. V. Dubonos, I. V. Grigorieva, and A. A. Firsov. Electric field effect in atomically thin carbon films. *Science*, 306(5696):666–669, 2004.

[7] Katherine A. Dunphy Guzman, Margaret R. Taylor, and Jillian F. Banfield. Environmental risks of nanotechnology: National nanotechnology initiative funding, $2000 \sim 2004$. *Environmental Science & Technology*, 40(5):1401–1407, 2006.

[8] Adam Peng and Wei Liu. Semiconductor nanocrystal complexes comprising a metal coating and methods. *U. S. Patent*, 7,482,059, 2009.

[9] Kourosh Kalantar-zadeh and Benjamin Fry. *Nanotechnology enabled sensors*. Springer, New York, 2007.

[10] Jr. Bruchez, Marcel, Mario Moronne, Peter Gin, Shimon Weiss, and A. Paul Alivisatos. Semiconductor nanocrystals as fluorescent biological labels. *Science*, 281(5385):2013–2016, 1998.

[11] Adam de la Zerda and Sanjiv S. Gambhir. Drug delivery: Keeping tabs on nanocarriers. *Nat Nano*, 2(12):745–746, 2007.

[12] William A. Tisdale, Kenrick J. Williams, Brooke A. Timp, David J. Norris, Eray S. Aydil, and X.-Y. Zhu. Hot-electron transfer from semiconductor nanocrystals. *Science*, 328(5985):1543–1547, 2010.

[13] D. G. Rickerby and M. Morrison. Nanotechnology and the environment: A european perspective. *Science and Technology of Advanced Materials*, 8(1-2):19, 2007.

[14] Nicholas A. Melosh, Akram Boukai, Frederic Diana, Brian Gerardot, Antonio Badolato, Pierre M. Petroff, and James R. Heath. Ultrahigh-density nanowire lattices and circuits. *Science*, 300(5616):112–115, 2003.

[15] Peter Grundler. *Chemical Sensors - An Introduction for Scientists and Engineers*. Springer, Leipzig, 2006.

[16] J. Hesse, J. W. Gardner, and W. Gopel. *Sensors Applications*. Wiley-VCH, Weinheim, 2003.

[17] Jack Chou. *Hazardous Gas Monitors: A Practical Guide to Selection, Operation, and Applications*. McGraw-Hill Professional, New York, 1999.

[18] Ruth N. Hull, Constantin-Horia Barbu, Nadezhda Goncharova, Waldemar Nawrocki, and Tadeusz Nawalaniec. Sensors and communications in environment monitoring systems. In *Strategies to Enhance Environmental Security in Transition Countries*, NATO Science for Peace and Security Series C: Environmental Security, pages 153–165. Springer Netherlands, —2007—.

[19] Mauri Kuorilehto, Mikko Kohvakka, Jukka Suhonen, Panu Hamalainen, Mark Hannikainen, and Timo D. Hamalainen. *Ultra-low energy wireless sensor networks in practice*. John Wiley & Sons Ltd., Chichester, England, 2007.

[20] John H. Holtz and Sanford A. Asher. Polymerized colloidal crystal hydrogel films as intelligent chemical sensing materials. *Nature*, 389(6653):829–832, 1997.

[21] G. Sberveglieri. *Gas Sensors - Principles, Operation and Developments*. Kluwer Academic Publishers, Boston, 1992.

[22] M. G. Jones and T. G. Nevell. The detection of hydrogen using catalytic flammable gas sensors. *Sensors and Actuators*, 16(3):215–224, 1989.

[23] A. D'Amico and E. Verona. SAW sensors. *Sens. Actuators*, 17(1-2):55–66, 1989.

[24] Cheryl M. Harris. Product review: Seeing SAW potential. *Anal. Chem.*, 75(15):355 A–358 A, 2003.

[25] D. Lange, O. Brand, and H. Baltes. *Cantilever-based CMOS Sensor Systems*. Springer, 2002.

[26] A. K. Naik, M. S. Hanay, W. K. Hiebert, X. L. Feng, and M. L. Roukes. Towards single-molecule nanomechanical mass spectrometry. *Nat Nano*, 4(7):445–450, 2009.

[27] Mo Li, H. X. Tang, and M. L. Roukes. Ultra-sensitive NEMS-based cantilevers for sensing, scanned probe and very high-frequency applications. *Nat Nano*, 2(2):114–120, 2007.

[28] Chengxiang Wang, Longwei Yin, Luyuan Zhang, Dong Xiang, and Rui Gao. Metal oxide gas sensors: Sensitivity and influencing factors. *Sensors*, 10(3):2088–2106, 2010.

[29] Josephine B. Chang, Vincent Liu, Vivek Subramanian, Kevin Sivula, Christine Luscombe, Amanda Murphy, Jinsong Liu, and Jean M. J. Frechet. Printable polythiophene gas sensor array for low-cost electronic noses. *Journal of Applied Physics*, 100(1):014506–7, 2006.

[30] Jiri Janata and Mira Josowicz. Conducting polymers in electronic chemical sensors. *Nat. Mater.*, 2(1):19–24, 2003.

[31] Hua Bai and Gaoquan Shi. Gas sensors based on conducting polymers. *Sensors*, 7(3):267–307, 2007.

[32] F. Schedin, A. K. Geim, S. V. Morozov, E. W. Hill, P. Blake, M. I. Katsnelson, and K. S. Novoselov. Detection of individual gas molecules adsorbed on graphene. *Nat Mater*, 6(9):652–655, 2007.

[33] Alexander Star, Vikram Joshi, Sergei Skarupo, David Thomas, and Jean-Christophe P. Gabriel. Gas sensor array based on metal-decorated carbon nanotubes. *J. Phys. Chem. B*, 110(42):21014, 2006.

[34] Changshi Lao, Yi Li, C. P. Wong, and Z. L. Wang. Enhancing the electrical and optoelectronic performance of nanobelt devices by molecular surface functionalization. *Nano Lett.*, 7(5):1323–1328, 2007.

[35] Chang Shi Lao, Qin Kuang, Zhong L. Wang, Myung-Chul Park, and Yulin Deng. Polymer functionalized piezoelectric-fet as humidity/chemical nanosensors. *Appl. Phys. Lett.*, 90(26):262107–3, 2007.

[36] Te-Yu Wei, Ping-Hung Yeh, Shih-Yuan Lu, and Zhong Lin Wang. Gigantic enhancement in sensitivity using schottky contacted nanowire nanosensor. *Journal of the American Chemical Society*, 131(48):17690–17695, 2009.

[37] Youfan Hu, Jun Zhou, Ping-Hung Yeh, Zhou Li, Te-Yu Wei, and Zhong Lin Wang. Supersensitive, fast-response nanowire sensors by using schottky contacts. *Advanced Materials*, 22(30):3327, 2010.

[38] Evgheni Strelcov, Yigal Lilach, and Andrei Kolmakov. Gas sensor based on metal insulator transition in VO$_2$ nanowire thermistor. *Nano Letters*, 9(6):2322–2326, 2009.

[39] Jeong Min Baik, Myung Hwa Kim, Christopher Larson, Cafer T. Yavuz, Galen D. Stucky, Alec M. Wodtke, and Martin Moskovits. Pd-sensitized single vanadium oxide nanowires: Highly responsive hydrogen sensing based on the metal-insulator transition. *Nano Letters*, 9(12):3980–3984, 2009.

[40] W. Gopel, J. Hesse, and J. N. Zemel. *Sensors, A Comprehensive Survey*, volume 1-9. Wiley-VCH, Weinheim, 1989-1995.

[41] Nicolae Barsan and Udo Weimar. Conduction model of metal oxide gas sensors. *J. Electroceram.*, 7(3):143–167, 2001.

[42] S. M. Sze. *Physics of Semiconductor Devices*. John Wiley & Sons, New York, 1981.

[43] Yasuhiro Shimizu and Makoto Egashira. Basic aspects and challenges of semiconductor gas sensors. *MRS Bulletin*, 24(6):18, 1999.

[44] Hisahito Ogawa, Masahiro Nishikawa, and Atsushi Abe. Hall measurement studies and an electrical conduction model of tin oxide ultrafine particle films. *Journal of Applied Physics*, 53(6):4448–4455, 1982.

[45] Chaonan Xu, Jun Tamaki, Norio Miura, and Noboru Yamazoe. Grain size effects on gas sensitivity of porous SnO_2-based elements. *Sensors and Actuators B: Chemical*, 3(2):147–155, 1991.

[46] N. Yamazoe, Y. Kurokawa, and T. Seiyama. Effects of additives on semiconductor gas sensors. *Sensors and Actuators*, 4:283–289, 1983.

[47] Yuji Takao, Yutaka Iwanaga, Yasuhiro Shimizu, and Makoto Egashira. Trimethylamine-sensing mechanism of TiO_2-based sensors 1. effects of metal additives on trimethylamine-sensing properties of TiO_2 sensors. *Sensors and Actuators B: Chemical*, 10(3):229–234, 1993.

[48] Yuji Takao, Masahiko Nakanishi, Tomohiro Kawaguchi, Yasuhiro Shimizu, and Makoto Egashira. Semiconductor dimethylamine gas sensors with high sensitivity and selectivity. *Sensors and Actuators B: Chemical*, 25(1-3):375–379, 1995.

[49] G. G. Mandayo, E. Castano, F. J. Gracia, A. Cirera, A. Cornet, and J. R. Morante. Strategies to enhance the carbon monoxide sensitivity of tin oxide thin films. *Sens. Actuators B Chem.*, 95(1-3):90–96, 2005.

[50] Niranjan S. Ramgir, Imtiaz S. Mulla, and Kunjukrishna P. Vijayamohanan. A room temperature nitric oxide sensor actualized from Ru-doped SnO_2 nanowires. *Sens. Actuators B Chem.*, 107(2):708–715, 2005.

[51] Makoto Egashira and Yasuhiro Shimizu. Odor sensing by semiconductor metal oxides. *Sensors and Actuators B: Chemical*, 13(1-3):443–446, 1993.

[52] A. Kolmakov, D. O. Klenov, Y. Lilach, S. Stemmer, and M. Moskovits. Enhanced gas sensing by individual SnO_2 nanowires and nanobelts functionalized with Pd catalyst particles. *Nano Lett.*, 5(4):667, 2005.

[53] Carrie G. Read, Ellen M. P. Steinmiller, and Kyoung-Shin Choi. Atomic plane-selective deposition of gold nanoparticles on metal oxide crystals exploiting preferential adsorption of additives. *J. Am. Chem. Soc.*, 131(34):12040–12041, 2009.

[54] Diefeng Gu, Sandwip K. Dey, and Prashant Majhi. Effective work function of Pt, Pd, and Re on atomic layer deposited HfO_2. *Appl. Phys. Lett.*, 89(8):082907–3, 2006.

[55] V. Brinzari, G. Korotcenkov, V. Golovanov, J. Schwank, V. Lantto, and S. Saukko. Morphological rank of nano-scale tin dioxide films deposited by spray pyrolysis from $SnCl_4 5H_2O$ water solution. *Thin Solid Films*, 408(1-2):51–58, 2002.

[56] G. Korotcenkov, A. Cornet, E. Rossinyol, J. Arbiol, V. Brinzari, and Y. Blinov. Faceting characterization of tin dioxide nanocrystals deposited by spray pyrolysis from stannic chloride water solution. *Thin Solid Films*, 471(1-2):310–319, 2005.

[57] R. W. J. Scott, S. M. Yang, G. Chabanis, N. Coombs, D. E. Williams, and G. A. Ozin. Tin dioxide opals and inverted opals: Near-ideal microstructures for gas sensors. *Advanced Materials*, 13(19):1468–1472, 2001.

[58] Panchapakesan Balaji and et al. Sensitivity, selectivity and stability of tin oxide nanostructures on large area arrays of microhotplates. *Nanotechnology*, 17(2):415, 2006.

[59] Brian T. Holland, Christopher F. Blanford, Thang Do, and Andreas Stein. Synthesis of highly ordered, three-dimensional, macroporous structures of amorphous or crystalline inorganic oxides, phosphates, and hybrid composites. *Chemistry of Materials*, 11(3):795–805, 1999.

[60] N. L. V. Carreno, A. P. Maciel, E. R. Leite, P. N. Lisboa-Filho, E. Longo, A. Valentini, L. F. D. Probst, C. O. Paiva-Santos, and W. H. Schreiner. The influence of cation segregation on the methanol decomposition on nanostructured SnO_2. *Sensors and Actuators B: Chemical*, 86(2-3):185–192, 2002.

[61] Yasuhiro Shimizu, Toru Maekawa, Yuichiro Nakamura, and Makoto Egashira. Effects of gas diffusivity and reactivity on sensing properties of thick film SnO_2-based sensors. *Sensors and Actuators B: Chemical*, 46(3):163–168, 1998.

[62] Guozhen Shen, Po-Chiang Chen, Koungmin Ryu, and Chongwu Zhou. Devices and chemical sensing applications of metal oxide nanowires. *J Mater. Chem.*, 19:828 – 839, 2009.

[63] Yaping Dan, Stephane Evoy, and A. T. Charlie Johnson. Chemical gas sensors based on nanowires. In *Nanowire Research Progress*. Nova Science Publisher, —2008—.

[64] Xing-Jiu Huang and Yang-Kyu Choi. Chemical sensors based on nanostructured materials. *Sens. Actuators B Chem.*, 122(2):659–671, 2007.

[65] Andrei Kolmakov and Martin Moskovits. Chemical sensing and catalysis by one-dimensional metal-oxide nanostructures. *Annual Review of Materials Research*, 34(1):151–180, 2004.

[66] Jia Grace Lu, Paichun Chang, and Zhiyong Fan. Quasi-one-dimensional metal oxide materials–synthesis, properties and applications. *Mater. Sci. Eng. R Rep.*, 52(1-3):49–91, 2006.

[67] Zheng Wei Pan, Zu Rong Dai, and Zhong Lin Wang. Nanobelts of semiconducting oxides. *Science*, 291(5510):1947–1949, 2001.

[68] Soumitra Kar, Bhola Nath Pal, Subhadra Chaudhuri, and Dipankar Chakravorty. One-dimensional ZnO nanostructure arrays: Synthesis and characterization. *The Journal of Physical Chemistry B*, 110(10):4605–4611, 2006.

[69] T. Krishnakumar, R. Jayaprakash, N. Pinna, N. Donato, A. Bonavita, G. Micali, and G. Neri. CO gas sensing of ZnO nanostructures synthesized by an assisted microwave wet chemical route. *Sensors and Actuators B: Chemical*, 143(1):198–204, 2009.

[70] Chao Li, Daihua Zhang, Xiaolei Liu, Song Han, Tao Tang, Jie Han, and Chongwu Zhou. In_2O_3 nanowires as chemical sensors. *Applied Physics Letters*, 82(10):1613–1615, 2003.

[71] E. Comini, G. Faglia, G. Sberveglieri, Zhengwei Pan, and Zhong L. Wang. Stable and highly sensitive gas sensors based on semiconducting oxide nanobelts. *Appl. Phys. Lett.*, 81(10):1869–1871, 2002.

[72] Andrea Ponzoni, Elisabetta Comini, Giorgio Sberveglieri, Jun Zhou, Shao Zhi Deng, Ning Sheng Xu, Yong Ding, and Zhong Lin Wang. Ultrasensitive and highly selective gas sensors using three-dimensional tungsten oxide nanowire networks. *Appl. Phys. Lett.*, 88(20):203101–3, 2006.

[73] Zhifu Liu, Toshinari Yamazaki, Yanbai Shen, Toshio Kikuta, Noriyuki Nakatani, and Yongxiang Li. O_2 and CO sensing of Ga_2O_3 multiple nanowire gas sensors. *Sensors and Actuators B: Chemical*, 129(2):666–670, 2008.

[74] Jiguang Deng, Lei Zhang, Hongxing Dai, Hong He, and Chak Au. Single-crystalline $La_{0.6}Sr_{0.4}CoO_{3-\delta}$ nanowires/nanorods derived hydrothermally without the use of a template: Catalysts highly active for toluene complete oxidation. *Catalysis Letters*, 123(3):294–300, 2008.

[75] Daihua Zhang, Zuqin Liu, Chao Li, Tao Tang, Xiaolei Liu, Song Han, Bo Lei, and Chongwu Zhou. Detection of NO_2 down to ppb levels using individual and multiple In_2O_3 nanowire devices. *Nano Lett.*, 4(10):1919–1924, 2004.

[76] G. Korotcenkov. The role of morphology and crystallographic structure of metal oxides in response of conductometric-type gas sensors. *Mater. Sci. Eng. R Rep.*, 61(1-6):1–39, 2008.

[77] T. C. Pearce, S. S. Schiffman, H. T. Nagle, and J. W. Gardner. *Handbook of Machine Olfaction*. Wiley-VCH, 2003.

[78] Y. Engel, R. Elnathan, A. Pevzner, G. Davidi, E. Flaxer, and F. Patolsky. Supersensitive detection of explosives by silicon nanowire arrays. *Angewandte Chemie International Edition*, 49(38):6830–6835, 2010.

[79] Maxwell M. Mozell and Morris Jagodowicz. Chromatographic separation of odorants by the nose: Retention times measured across in vivo olfactory mucosa. *Science*, 181(4106):1247–1249, 1973.

[80] Krishna Persaud and George Dodd. Analysis of discrimination mechanisms in the mammalian olfactory system using a model nose. *Nature*, 299(5881):352–355, 1982.

[81] Po-Chiang Chen, Fumiaki N Ishikawa, Hsiao-Kang Chang, Koungmin Ryu, and Chongwu Zhou. A nanoelectronic nose: a hybrid nanowire/carbon nanotube sensor array with integrated micromachined hotplates for sensitive gas discrimination. *Nanotechnology*, 20(12):125503, 2009.

[82] Po-Chiang Chen, Guozhen Shen, and Chongwu Zhou. Chemical sensors and electronic noses based on 1-d metal oxide nanostructures. *IEEE Trans. Nanotechnol.*, 7(6):668–682, 2008.

[83] J. R. Stetter and W. R. Penrose. Understanding chemical sensors and chemical sensor arrays (electronic noses): Past, present, and future. *Sensors Update*, 10(1):189–229, 2002.

[84] Victor V. Sysoev, Bradly K. Button, Kelly Wepsiec, Serghei Dmitriev, and Andrei Kolmakov. Toward the nanoscopic "electronic nose": Hydrogen vs carbon monoxide discrimination with an array of individual metal oxide nano- and mesowire sensors. *Nano Lett.*, 6(8):1584–1588, 2006.

[85] Victor V. Sysoev, Joachim Goschnick, Thomas Schneider, Evghenii Strelcov, and Andrei Kolmakov. A gradient microarray electronic nose based on percolating SnO_2 nanowire sensing elements. *Nano Letters*, 7(10):3182–3188, 2007.

[86] Victor V. Sysoev, Evghenii Strelcov, Martin Sommer, Michael Bruns, Ilia Kiselev, Wilhelm Habicht, Swastik Kar, Luca Gregoratti, Maya Kiskinova, and Andrei Kolmakov. Single-nanobelt electronic nose: Engineering and tests of the simplest analytical element. *ACS Nano*, pages null–null, 2010.

[87] Qingwei Chen, Dongsheng Xu, Zhongyun Wu, and Zhongfan Liu. Free-standing TiO_2 nanotube arrays made by anodic oxidation and ultrasonic splitting. *Nanotechnology*, 19(36):365708, 2008.

[88] Chuanwei Cheng, Bo Liu, Huiying Yang, Weiwei Zhou, Li Sun, Rui Chen, Siu Fung Yu, Jixuan Zhang, Hao Gong, Handong Sun, and Hong Jin Fan. Hierarchical assembly of ZnO nanostructures on SnO_2 backbone nanowires: Low-temperature hydrothermal preparation and optical properties. *ACS Nano*, 3(10):3069–3076, 2009.

[89] Seung-Hoon Choi, Guy Ankonina, Doo-Young Youn, Seong-Geun Oh, Jae-Min Hong, Avner Rothschild, and Il-Doo Kim. Hollow ZnO nanofibers fabricated using electrospun polymer templates and their electronic transport properties. *ACS Nano*, 2009.

[90] Teppei Iwanaga, Takeo Hyodo, Yasuhiro Shimizu, and Makoto Egashira. H_2 sensing properties and mechanism of anodically oxidized TiO_2 film contacted with Pd electrode. *Sens. Actuators B Chem.*, 93(1-3):519–525, 2003.

[91] Maggie Paulose, Oomman K Varghese, Gopal K Mor, Craig A Grimes, and Keat G Ong. Unprecedented ultra-high hydrogen gas sensitivity in undoped titania nanotubes. *Nanotechnology*, 17(2):398, 2006.

[92] Min-Chang Jeong, Byeong-Yun Oh, Ok-Hyun Nam, Taek Kim, and Jae-Min Myoung. Three-dimensional ZnO hybrid nanostructures for oxygen sensing application. *Nanotechnology*, 17(2):526, 2006.

[93] C. Baratto, G. Faglia, G. Sberveglieri, A. Sutti, G. Calestani, and C. Dionigi. Inverse opal structure of SnO_2 and SnO_2 : Zn for gas sensing. In *Sensors, 2005 IEEE*, pages 1196–1200, 2005.

[94] C. F. Blanford, R. C. Schroden, M. Al-Daous, and A. Stein. Tuning solvent-dependent color changes of three-dimensionally ordered macroporous (3DOM) materials through compositional and geometric modifications. *Advanced Materials*, 13(1):26–29, 2001.

[95] Cheng-Yu Kuo, Shih-Yuan Lu, Shengfu Chen, Matt Bernards, and Shaoyi Jiang. Stop band shift based chemical sensing with three-dimensional opal and inverse opal structures. *Sensors and Actuators B: Chemical*, 124(2):452–458, 2007.

[96] V. N. Bogomolov, S. V. Gaponenko, I. N. Germanenko, A. M. Kapitonov, E. P. Petrov, N. V. Gaponenko, A. V. Prokofiev, A. N. Ponyavina, N. I. Silvanovich, and S. M. Samoilovich. Photonic band gap phenomenon and optical properties of artificial opals. *Physical Review E*, 55(6):7619, 1997.

[97] Jongseung Yoon, Sungjin Jo, Ik Su Chun, Inhwa Jung, Hoon-Sik Kim, Matthew Meitl, Etienne Menard, Xiuling Li, James J. Coleman, Ungyu Paik, and John A. Rogers. Gaas photovoltaics and optoelectronics using releasable multilayer epitaxial assemblies. *Nature*, 465(7296):329–333, 2010.

[98] R. S. Wagner and W. C. Ellis. Vapor-liquid-solid mechanism of single crystal growth. *Appl. Phys. Lett.*, 4(5):89–90, 1964.

[99] Magnus T. Borgstrom, George Immink, Bas Ketelaars, Rienk Algra, and P. A. M. BakkersErik. Synergetic nanowire growth. *Nat. Nano.*, 2(9):541–544, 2007.

[100] Zhuo Chen and Chuanbao Cao. Effect of size in nanowires grown by the vapor-liquid-solid mechanism. *Appl. Phys. Lett.*, 88(14):143118–3, 2006.

[101] V. G. Dubrovskii, G. E. Cirlin, I. P. Soshnikov, A. A. Tonkikh, N. V. Sibirev, Yu B. Samsonenko, and V. M. Ustinov. Diffusion-induced growth of GaAs nanowhiskers during molecular beam epitaxy: Theory and experiment. *Phys. Rev. B*, 71(20):205325, 2005.

[102] Jonas Johansson, C. Patrik T. Svensson, Thomas Martensson, Lars Samuelson, and Werner Seifert. Mass transport model for semiconductor nanowire growth. *J. Phys. Chem. B*, 109(28):13567–13571, 2005.

[103] Douglas B. Chrisey and Graham K. Hubler. *Pulsed Laser Deposition of Thin Films*. Wiley-Interscience, New York, 1994.

[104] Haiyong Gao, Wenjie Cai, Paresh Shimpi, Hui-Jan Lin, and Pu-Xian Gao. $(La, Sr)CoO_3$/ZnO nanofilm-nanorod diode arrays for photo-responsive moisture and humidity detection. *Journal of Physics D: Applied Physics*, 43(27):272002, 2010.

[105] S. Gubbala, J. Thangala, and M. K. Sunkara. Nanowire-based electrochromic devices. *Solar Energy Materials and Solar Cells*, 91(9):813–820, 2007.

[106] I. Turyan, U. O. Krasovec, B. Orel, T. Saraidorov, R. Reisfeld, and D. Mandler. "writing–reading–erasing" on tungsten oxide films using the scanning electrochemical microscope. *Advanced Materials*, 12(5):330–333, 2000.

[107] J. L. Solis, S. Saukko, L. Kish, C. G. Granqvist, and V. Lantto. Semiconductor gas sensors based on nanostructured tungsten oxide. *Thin Solid Films*, 391(2):255–260, 2001.

[108] Chia-Ching Liao, Fu-Rong Chen, and Ji-Jung Kai. WO_{3-x} nanowires based electrochromic devices. *Solar Energy Materials and Solar Cells*, 90(7-8):1147–1155, 2006.

[109] Chandra Sekhar Rout, A. Govindaraj, and C. N. R. Rao. High-sensitivity hydrocarbon sensors based on tungsten oxide nanowires. *Journal of Materials Chemistry*, 16(40):3936–3941, 2006.

[110] Shih-Han Wang, Tse-Chuan Chou, and Chung-Chiun Liu. Nano-crystalline tungsten oxide NO_2 sensor. *Sensors and Actuators B: Chemical*, 94(3):343–351, 2003.

[111] C. Cantalini, M. Pelino, H. T. Sun, M. Faccio, S. Santucci, L. Lozzi, and M. Passacantando. Cross sensitivity and stability of NO_2 sensors from WO_3 thin film. *Sensors and Actuators B: Chemical*, 35(1-3):112–118, 1996.

[112] Lisheng Wang, Judit Pfeifer, Csaba Balazsi, and P. I. Gouma. Synthesis and sensing properties to NH_3 of hexagonal WO_3 metastable nanopowders. *Materials and Manufacturing Processes*, 22(6):773 – 776, 2007.

[113] Reit Artzi-Gerlitz, Kurt D. Benkstein, David L. Lahr, Joshua L. Hertz, Christopher B. Montgomery, John E. Bonevich, Steve Semancik, and Michael J. Tarlov. Fabrication and gas sensing performance of parallel assemblies of metal oxide nanotubes supported by porous aluminum oxide membranes. *Sensors and Actuators B: Chemical*, 136(1):257–264, 2009.

[114] Shibin Sun, Yimin Zhao, Yongde Xia, Zengda Zou, Guanghui Min, and Yanqiu Zhu. Bundled tungsten oxide nanowires under thermal processing. *Nanotechnology*, 19(30):305709, 2008.

[115] Baobao Cao, Jiajun Chen, Xiaojun Tang, and Weilie Zhou. Growth of monoclinic WO_3 nanowire array for highly sensitive NO_2 detection. *J. Mater. Chem.*, 19:2323–2327, 2009.

[116] Jae Young Park, Dong Eon Song, and Sang Sub Kim. An approach to fabricating chemical sensors based on ZnO nanorod arrays. *Nanotechnology*, 19(10):105503, 2008.

[117] B. Deb, S. Desai, G. U. Sumanasekera, and M. K. Sunkara. Gas sensing behaviour of mat-like networked tungsten oxide nanowire thin films. *Nanotechnology*, 18(28):285501, 2007.

[118] A. E. Rakhshani. Preparation, characteristics and photovoltaic properties of cuprous oxide–a review. *Solid-State Electronics*, 29(1):7–17, 1986.

[119] Rajesh Kumar, Atul Khanna, Pragya Tripathi, R. V. Nandedkar, S. R. Potdar, S. M. Chaudhari, and S. S. Bhatti. $CuO - SnO_2$ element as hydrogen sulfide gas sensor prepared by a sequential electron beam evaporation technique. *Journal of Physics D: Applied Physics*, 36(19):2377, 2003.

[120] Xuchuan Jiang, Thurston Herricks, and Younan Xia. CuO nanowires can be synthesized by heating copper substrates in air. *Nano Letters*, 2(12):1333–1338, 2002.

[121] Jiajun Chen, Kai Wang, Lisa Hartman, and Weilie Zhou. H_2S detection by vertically aligned CuO nanowire array sensors. *J. Phys. Chem. C*, 112(41):16017–16021, 2008.

[122] Yuanda Wu, Maosong Tong, Xiuli He, Yushu Zhang, and Guorui Dai. Thin film sensors of $SnO_2 - CuO - SnO_2$ sandwich structure to H_2S. *Sensors and Actuators B: Chemical*, 79(2-3):187–191, 2001.

[123] G. Sarala Devi, S. Manorama, and V. J. Rao. High sensitivity and selectivity of an SnO_2 sensor to H_2S at around 100 °C. *Sensors and Actuators B: Chemical*, 28(1):31–37, 1995.

[124] M. T. Bjork, B. J. Ohlsson, T. Sass, A. I. Persson, C. Thelander, M. H. Magnusson, K. Deppert, L. R. Wallenberg, and L. Samuelson. One-dimensional heterostructures in semiconductor nanowhiskers. *Applied Physics Letters*, 80(6):1058–1060, 2002.

[125] T. W. Hickmott, P. M. Solomon, R. Fischer, and H. Morkoc. Negative charge, barrier heights, and the conduction-band discontinuity in al[sub x]ga[sub 1 - x]as capacitors. *Journal of Applied Physics*, 57(8):2844–2853, 1985.

[126] X. Y. Xue, P. Feng, C. Wang, Y. J. Chen, Y. G. Wang, and T. H. Wang. Electrical transport through individual nanowires with transverse grain boundaries. *Applied Physics Letters*, 89(2):022115–3, 2006.

[127] Keith J. Albert, Nathan S. Lewis, Caroline L. Schauer, Gregory A. Sotzing, Shannon E. Stitzel, Thomas P. Vaid, and David R. Walt. Cross-reactive chemical sensor arrays. *Chem. Rev.*, 100(7):2595–2626, 2000.

[128] Zhong Lin Wang. Zinc oxide nanostructures: growth, properties and applications. *Journal of Physics: Condensed Matter*, 16(25):R829, 2004.

[129] Yaguang Wei, Wenzhuo Wu, Rui Guo, Dajun Yuan, Suman Das, and Zhong Lin Wang. Wafer-scale high-throughput ordered growth of vertically aligned ZnO nanowire arrays. *Nano Letters*, 10(9):3414–3419, 2010.

[130] Lori E. Greene, Matt Law, Dawud H. Tan, Max Montano, Josh Goldberger, Gabor Somorjai, and Peidong Yang. General route to vertical ZnO nanowire arrays using textured ZnO seeds. *Nano Lett.*, 5(7):1231–1236, 2005.

[131] Daisuke Ito, Michael L. Jespersen, and James E. Hutchison. Selective growth of vertical ZnO nanowire arrays using chemically anchored gold nanoparticles. *ACS Nano*, 2(10):2001–2006, 2008.

[132] L. Vayssieres. Growth of arrayed nanorods and nanowires of ZnO from aqueous solutions. *Adv. Mater.*, 15(5):464–466, 2003.

[133] Lionel Vayssieres, Karin Keis, Anders Hagfeldt, and Sten-Eric Lindquist. Three-dimensional array of highly oriented crystalline ZnO microtubes. *Chem. Mater.*, 13(12):4395–4398, 2001.

[134] Sheng Xu, Yaguang Wei, Melanie Kirkham, Jin Liu, Wenjie Mai, Dragomir Davidovic, Robert L. Snyder, and Zhong Lin Wang. Patterned growth of vertically aligned ZnO nanowire arrays on inorganic substrates at low temperature without catalyst. *J. Am. Chem. Soc.*, 130(45):14958–14959, 2008.

[135] Sheng Xu, Nagesh Adiga, Shan Ba, Tirthankar Dasgupta, C. F. Jeff Wu, and Zhong Lin Wang. Optimizing and improving the growth quality of ZnO nanowire arrays guided by statistical design of experiments. *ACS Nano*, 3(7):1803–1812, 2009.

[136] Jiajun Chen, Kai Wang, Rong Huang, T. Saito, Y.H. Ikuhara, T. Hirayama, and Weilie Zhou. Facile route to polycrystalline Pd/SnO_2 nanowires using ZnO-nanowire templates for gas-sensing applications. *IEEE Trans. Nanotechnol.*, 9(5):634, 2010.

[137] Ivan V. Markov. *Crystal Growth for Beginners: Fundamentals of Nucleation, Crystal Growth, and Epitaxy*. World Scientific Publishing Co. Pte. Ltd., London, 2003.

[138] Hailong Wang, Moneesh Upmanyu, and Cristian V. Ciobanu. Morphology of epitaxial core-shell nanowires. *Nano Lett.*, 8(12):4305–4311, 2008.

[139] Kai Wang, Jiajun Chen, Weilie Zhou, Yong Zhang, Yanfa Yan, John Pern, and Angelo Mascarenhas. Direct growth of highly mismatched type II ZnO/ZnSe core/shell nanowire arrays on transparent conducting oxide substrates for solar cell applications. *Adv. Mater.*, 20(17):3248–3253, 2008.

[140] Vladimir Komanicky, Hakim Iddir, Kee-Chul Chang, Andreas Menzel, Goran Karapetrov, Daniel Hennessy, Peter Zapol, and Hoydoo You. Shape-dependent activity of platinum array catalyst. *J. Am. Chem. Soc.*, 131(16):5732–5733, 2009.

[141] G. Korotcenkov. Gas response control through structural and chemical modification of metal oxide films: state of the art and approaches. *Sens. Actuators B Chem.*, 107(1):209–232, 2005.

[142] R. A. Bennett, P. Stone, and M. Browker. Scanning tunnelling microscopy studies of the re-activity of the TiO$_2$(110) surface: Re-oxidation and the thermal treatment of metal nanoparticles. *Faraday Discuss.*, 114:267–277, 1999.

[143] Pengfei Qi, Ophir Vermesh, Mihai Grecu, Ali Javey, Qian Wang, Hongjie Dai, Shu Peng, and K. J. Cho. Toward large arrays of multiplex functionalized carbon nanotube sensors for highly sensitive and selective molecular detection. *Nano Lett.*, 3(3):347–351, 2003.

[144] Unpublished data.

[145] K. D. Harris, A. Huizinga, and M. J. Brett. High-speed porous thin film humidity sensors. *Electrochem. Solid-State Lett.*, 5(11):H27–H29, 2002.

[146] T. Smy, D. Vick, M. J. Brett, S. K. Dew, A. T. Wu, J. C. Sit, and K. D. Harris. Three-dimensional simulation of film microstructure produced by glancing angle deposition. *J. Vac. Sci. Technol. A*, 18(5):2507–2512, 2000.

[147] H. T. Wang, B. S. Kang, F. Ren, L. C. Tien, P. W. Sadik, D. P. Norton, S. J. Pearton, and J. Lin. Detection of hydrogen at room temperature with catalyst-coated multiple ZnO nanorods. *Appl. Phys. A*, 81(6):1117–1119, 2005.

[148] Jeong Min Baik, Mark Zielke, Myung Hwa Kim, Kimberly L. Turner, Alec M. Wodtke, and Martin Moskovits. Tin-oxide-nanowire-based electronic nose using heterogeneous catalysis as a functionalization strategy. *ACS Nano*, 4(6):3117–3122, 2010.

[149] P. C. Jurs, G. A. Bakken, and H. E. McClelland. Computational methods for the analysis of chemical sensor array data from volatile analytes. *Chem. Rev.*, 100(7):2649–2678, 2000.

[150] Peter Offermans, Mercedes Crego-Calama, and Sywert H. Brongersma. Gas detection with vertical InAs nanowire arrays. *Nano Letters*, 10(7):2412–2415, 2010.

[151] Y. Tang, J. R. Nyengaard, D. M. De Groot, and H. J. G. Gundersen. Total regional and global number of synapses in the human brain neocortex. *Synapse*, 41(3):258–273, 2001.

[152] David B. Kirk and Wen-mei W. Hwu. *Programming Massively Parallel Processors: A Hands-on Approach*. Morgan Kaufmann, Burlington, 2010.

[153] Julian W. Gardner and Philip N. Bartlett. A brief history of electronic noses. *Sensors and Actuators B: Chemical*, 18(1-3):210–211, 1994.

[154] Joseph F. Hair, William C. Black, Barry J. Babin, and Rolph E. Anderson. *Multivariate Data Analysis*. Prentice Hall, New Jersey, 7 edition, 2009.

Vita

Mr. J. Chen was born in Meizhou, Guangdong province, China. He moved to Shenzhen, a young metropolis in southern China, with his family, where he received his primary and high school education. He attended undergraduate and master programs in majors of electronic materials and materials physics and chemistry, in University of Electronic Science and Technology of China (UESTC), Chengdu, Sichuan Province. During the master program, he and his colleagues fabricated the first 3-inch double-sided high temperature superconductor thin films in China. He joined the Ph. D program of Engineering and Applied Sciences Program in Advanced Materials Research Institute, University of New Orleans, where he enjoyed making really tiny stuffs. During his Ph. D program, he worked on applications of nanostructured materials for spintronics, photovoltaics, and most importantly, gas sensors.